MBE Growth and Characterisation of Metastable Transition Metal Sulphides

by

Lorraine David M.Phys. (Hons.)

Submitted for the degree of Doctor of Philosophy

Heriot-Watt University

School of Engineering and Physical Sciences

March 2006

Abstract

This thesis describes the growth by Molecular Beam Epitaxy (MBE) and characterisation of two metastable transition metal sulphides. Details of the growth method used to produce zinc blende (ZB) manganese sulphide and ZB chromium sulphide will be presented as well as structural characterisation of the layers produced.

Layers of ZB MnS have been produced up to 132 nm thick, which exceeds the previous limit of only 50 nm. The structural quality was analysed using X-Ray Diffraction (XRD). The lattice constant was found to be 0.5559 ± 0.0002 nm and Poisson's ratio was determined to be 0.475. X-ray Interference (XRI) was used to determine the growth rate of ZB MnS as 0.15 μhr^{-1}. Surface studies using Atomic Force Microscopy (AFM) showed the formation of 1D ridges on layers greater than 20 nm. A series of MnS layers were grown for X-ray Photoelectron Spectroscopy (XPS) measurements, which were used to determine a type II valence band offset of 48 ± 90 meV between ZnSe and MnS. Photoluminescence (PL) results from a fully metastable structure of a MnS quantum well with MgS barriers were also discussed.

Growth of ZB CrS, initially thought to be lattice matched to InP substrates, was carried out before a re-determination of the CrS lattice parameter using both the XRI of MnCrS layers and calculations using published atomic radii. This confirmed that GaP would be the preferred substrate. Subsequently, XRI on thin layers grown on GaP substrates has determined the lattice parameter of CrS to be 5.3525 ± 0.0025 Å and Poisson's ratio as 0.48 ± 0.02.

Acknowledgements

I would like to thank my supervisor, Kevin Prior, for his guidance and assistance over the last few years. Thanks also go to Brian Cavenett and Richard Warburton for the helpful discussions during our group meetings.

Members of the MBE group, both past and present, deserve thanks and recognition for the many, many hours we all spent together in the lab with spanners in our hands. I'd like to acknowledge Xiaodong Tang for the X-ray characterisation of the MnS layers presented in this thesis. I would also like to thank members of the Nano-optics group at Heriot-Watt for carrying out the Photoluminescence experiments.

The lunchtime crowd deserve a mention for always managing to find the funny side of everything and ensuring that everyday was interesting so, in no particular order: Paul, Heather, Jess, Clare, Martin, Euan, Stuart, Karl, Matthias, Arran and Tim. I'd also like to thank the technical and secretarial staff in the Brewster Building, without them a lot of people would be stuck in the mud around here.

Special thanks go to my parents, Bob and Lorna David, for supporting and encouraging me throughout my education.

Finally, I'd like to thank my boyfriend, Gordon Russell, for keeping me sane and putting up with me, especially during the writing process.

ACADEMIC REGISTRY
Research Thesis Submission

Name:	Lorraine David		
School/PGI:	School of Engineering and Physical Sciences		
Version: *(i.e. First, Resubmission, Final)*	Final	Degree Sought:	PhD

Declaration

In accordance with the appropriate regulations I hereby submit my thesis and I declare that:

1) the thesis embodies the results of my own work and has been composed by myself
2) where appropriate, I have made acknowledgement of the work of others and have made reference to work carried out in collaboration with other persons
3) the thesis is the correct version of the thesis for submission*.
4) my thesis for the award referred to, deposited in the Heriot-Watt University Library, should be made available for loan or photocopying, subject to such conditions as the Librarian may require
5) I understand that as a student of the University I am required to abide by the Regulations of the University and to conform to its discipline.

* *Please note that it is the responsibility of the candidate to ensure that the correct version of the thesis is submitted.*

Signature of Candidate:		Date:	24/03/06

Submission

Submitted By *(name in capitals)*:	JOHN I B WILSON
Signature of Individual Submitting:	
Date Submitted:	31/3/06

For Completion in Academic Registry

Received in the Academic Registry by *(name in capitals)*:	VAL MURDOCH		
Method of Submission *(Handed in to Academic Registry; posted through internal/external mail)*:	Handed in to AR		
Signature:		Date:	31/3/06

Table of Contents

Publications

1. K.A. Prior, X. Tang, C. O'Donnell, C. Bradford, L. David, B.C. Cavenett, Characterisation of MBE grown II-VI semiconductor thin layers by X-Ray Interference, J. Crystal Growth, 251 (2003) 565-570

2. L. David, C. Bradford, X. Tang, T.C.M. Graham, K.A. Prior and B.C. Cavenett, Growth of zinc blende MnS and MnS heterostructures by MBE using ZnS as a sulphur source, J. Crystal Growth, 251 (2003) 591-595

3. K.A. Prior, C. Bradford, L. David, X. Tang, B.C. Cavenett, Growth by MBE and characterization of Metastable group II sulphides, Phys. Stat. Sol. (b) 241 (2004) 463-470.

4. L. David, C. Bradford, X. Tang, T.C.M. Graham, G. Beamson, D. Wolverson, K.A. Prior and B.C. Cavenett, Characterization of heterostructures containing MnS grown by MBE, Phys. Stat. Sol. (b) 241 (2004) 471-474

5. K.A. Prior, C. Bradford, L. David, X. Tang, B.C. Cavenett, Metastable group II sulphides grown by MBE: surface morphology and crystal structure, J. Cryst Growth, 275 (2005) 141-149

6. L. David and K.A. Prior, Determination of the Lattice Constant of CrS from $Mn_{1-x}Cr_xS$ MBE Epitaxial Layers, Phys Stat. Sol. (b), 243 (2006) 778-781

Presentations at meetings

1. Characterisation of MBE grown II-VI semiconductor thin layers by X-Ray Interference, K.A. Prior, X. Tang, C. O'Donnell, C. Bradford, L. David, B.C. Cavenett, presented at MBE-XII, San Francisco, September 2002.

2. Growth of zinc blende MnS and MnS heterostructures by MBE using ZnS as a sulphur source, L. David, C. Bradford, X. Tang, T.C.M. Graham, K.A. Prior and B.C. Cavenett, presented at MBE-XII, San Francisco, September 2002.

3. Characterisation of heterostructures containing MnS grown by MBE, L. David, C. Bradford, X. Tang, T.C.M. Graham, G. Beamson, D. Wolverson, K.A. Prior and B.C. Cavenett, presented at the 11th International Conference on II-VI compounds, Niagra, September 2003

4. Growth by MBE and characterisation of metastable group II sulphides, K.A. Prior, C. Bradford, L. David, X. Tang, B.C. Cavenett, invited presentation, at the 11th International Conference on II-VI compounds Niagra, September 2003

5. Growth of zinc blende MnS by MBE using ZnS as a source of sulphur, L. David, X. Tang, G. Beamson, T.C.M. Graham, K.A. Prior, and B.C. Cavenett. Set for Britain, Materials Research Evening Reception, House of Commons, London, March 2004

6. Growth and characterisation of zincblende MnS by MBE using ZnS as a sulphur source, L. David, X. Tang, K.A. Prior and B.C. Cavenett. Prep 2004, University of Hertfordshire, April 2004

7. Growth by MBE and characterisation of metastable group II sulphides, K.A. Prior, C. Bradford, L. David, X. Tang, B.C. Cavenett, invited presentation at 14th International Conference on Crystal Growth (ICCG-14) Grenoble August 2004

8. Determination of the Lattice Constant of CrS from $Mn_{1-x}Cr_xS$ MBE Epitaxial Layers, L. David and K.A. Prior, presented at the 12th International Conference on II-VI materials, Warsaw, September 2005

Chapter 1: Introduction

1.1 Molecular Beam Epitaxy

Molecular Beam Epitaxy (MBE) was developed in the late 1960s [1], in reply to the demand for a crystal growth technology to produce single crystal films less than 100 nm thick. Under ultra high vacuum conditions, the epilayers crystallise as a result of reactions between thermal-energy molecular beams of the constituent elements and a substrate surface, which is maintained at an elevated temperature. The composition of the layer produced is dependant on the relative arrival rates of the constituent elements, which are dependant on the evaporation rates of the sources.

Initial work on the MBE technique was focused on understanding the processes involved in the growth of both homoepitaxial and heteroepitaxial layers, and developing the technique for the production of device quality material. In the late 1980s, MBE became a high volume production technology, with developments enabling the use of larger substrates, higher uniformity, faster turnaround and real time monitoring to be designed into the system. At present, commercially available MBE systems can accommodate up to 7x6" substrates per platen, which allows cost effective, high yield growth.

In addition to the application of MBE to mass market production, it is also ideal for developing new material systems on a smaller scale. The main reasons for this are

that MBE is known as a "clean" technique, which means that the source materials are of a high purity (5N or higher) and the UHV environment minimises contamination in the system. The UHV environment also allows the use of *in situ* monitoring techniques, such as Reflection High Energy Electron Diffraction (RHEED) and Mass Spectrometry. RHEED (see section 2.5) is used to monitor the surface of the sample during oxide removal from the substrate and during growth of the epilayer. The quality of the UHV is monitored by Mass Spectrometry (see section 2.4), which also assists in maintaining the "clean" environment.

1.2 Spintronics

Spintronics (spin transport electronics) utilises the spin state of the electron to manipulate information instead of, or in conjunction with, the charge of the electron, as in conventional electronics. It is believed that by exploiting the spin degree of freedom, the capability and performance of electronic products will be substantially improved. These non-volatile spintronic devices would have increased data processing speed and decreased electric power consumption compared with conventional semiconductor devices. Before such devices can be manufactured, there are many challenges that must be addressed, including the optimisation of electron spin lifetimes, the detection of spin coherence in nanoscale structures, transport of spin-polarised carriers across relevant length scales and heterointerfaces and the manipulation of both electron and nuclear spins on sufficiently fast time scales [2].

Giant magnetoresistance (GMR) devices have been in commercial use since 1997, which consist of alternating ferromagnetic and non-magnetic thin layers. The application of a magnetic field to the structure dramatically changes the resistance of the material, which is lowest when the magnetic moments in the ferromagnetic layers are aligned and highest when they are misaligned. GMR read heads on computer hard drives have improved the storage capacity on hard disks from 1 to 20 gigabits [3].

Recently, work in the field of spintronics has focused on the development of room temperature ferromagnetic materials. In II-VI semiconductors, p-type ZnO containing 5% Mn has been predicted to have a Curie temperature above room temperature [4]. However, the most successful II-VI room temperature ferromagnetic material is $Zn_{1-x}Cr_xTe$, which has a Curie temperature of 300 ± 10 K when x = 0.2 [5,6].

1.3 Heriot-Watt II-VI Research

The II-VI MBE group at Heriot-Watt was established in 1988, with the donation of an MBE machine by British Telecom. Early work in the group focused on light emitting devices, culminating in the development of Europe first blue laser in 1992 [7]. Research continued with the growth and characterisation p-type doping of ZnSe based semiconductors [8].

Following the worldwide shift away from II-VI laser growth in the mid 1990's, research at Heriot-Watt has focused on the structural properties and fundamental spectroscopy of II-VI semiconductors. The development of (Zn,Mg)S alloys and subsequently magnesium sulphide layers, through a variation on the conventional MBE growth technique [9], has allowed research into structures with large exciton binding energies to be explored.

The growth technique used to produce MgS in the zinc blende (ZB) crystal structure is an achievement as the stable crystal structure is rocksalt. It has opened up development of further metastable materials, including those presented in this thesis.

1.4 Outline of this Thesis

In this thesis work on the growth and characterisation of ZB manganese sulphide is reported as well as the initial work to produce layers of chromium (II) sulphide.

Chapter 2 contains a detailed description of the Heriot-Watt MBE system, which was used to produce all the layers discussed in this thesis. The *in situ* monitoring techniques used to monitor the UHV conditions and semiconductor growth are discussed. Various characterisation techniques are covered in Chapter 3, where the theoretical background and experimental set up of each technique is described and discussed.

The growth of MnS is outlined in Chapter 4. Structural characterisation of layers obtained from X-ray Interference (XRI) and X-ray diffraction (XRD) measurements are discussed, resulting in determinations of growth rate, lattice parameter and Poisson's ratio. Atomic Force Microscopy (AFM) has also been used to study surface features of ZB MnS.

Chapter 5 covers the characterisation of heterostructures containing MnS. X-ray Photoelectron Spectroscopy (XPS) measurements of ZnSe and thin MnS layers are detailed and used to determine the Valence Band offset between the two compounds. Photoluminescence (PL) results from ZnSe / MnS and fully metastable MnS / MgS quantum wells are discussed.

Initial work on the growth of CrS is detailed in Chapter 6, including the determination of a suitable substrate on which to grow the material. Initial X-ray characterisation of thin layers is also discussed.

Chapter 7 includes a summary of the work presented in this thesis and future prospects involving these materials are discussed.

References

[1] A.Y. Cho, M.B. Panish, I. Hayashi, 3rd. Int Symp. On Gallium Arsenide and Related Compounds, The Institute of Physics, Conference Series 9 (1970) 18

[2] S.A. Wolf, D.D. Awschalom, R.A. Buhrman, J.M. Daughton, S. von Molnár, M.L. Roukes, A.Y. Chtchelkanova and D.M. Treger, Science **294** (2001) 1488

[3] Visions 5 - Spintronics, http://policy.iop.org/v_production/v5.html, IOP publishing, October 2005

[4] T. Dietl and H. Ohno, Physica E **9** (2001) 185

[5] H. Saito, V. Zayets, S. Yamagata and K. Ando, Phys. Rev. Lett. **90** (2003) 207202

[6] K. Ando and H. Saito, presented at 12th International Conference on II-VI Compounds, Warsaw, Poland, September 2005

[7] S.Y. Wang, I. Hauksson, J. Simpson, H. Stewart, S.I.A. Adams, J.M. Wallace, Y. Kawakami, K.A. Prior and B.C. Cavenett, Appl. Phys. Lett. **61** (1992) 506

[8] I. Hauksson, J. Simpson, S.Y. Wang, K.A. Prior and B.C. Cavenett, Appl. Phys. Lett. **61** (1992) 2208

[9] C. Bradford, C.B. O'Donnell, B. Urbaszek, K.A. Prior and B.C. Cavenett, Phys. Rev. B **64** (2001) 195309

Chapter 2: Heriot-Watt MBE System

2.1 Introduction

There are many different crystal growth techniques used to produce high quality semiconductors. The technique described in this thesis is molecular beam epitaxy (MBE), which was developed in the late 1960s [1]. MBE is a crystal growth technique that allows high quality compound semiconductor layers to be grown with monolayer precision.

This chapter outlines the operation of the Heriot-Watt MBE system, discusses the available *in situ* monitoring techniques and details how these techniques were used to overcome a system contamination problem which occurred during the work presented in this thesis.

2.2 Overall System

All the samples analysed in this thesis were grown in a Vacuum Generators V80H MBE system (Figure 2.1). The V80H consists of four chambers isolated by gate valves. There are two similar growth chambers; HWA and HWB, both accessible through a preparation chamber and a fast entry lock, which allows samples to be quickly introduced into the vacuum environment. The entry lock has its own turbomolecular pump, which allows it to be brought up to atmosphere and back down to a pressure of 10^{-6} mbar. Initial flash heating of the sample, to remove

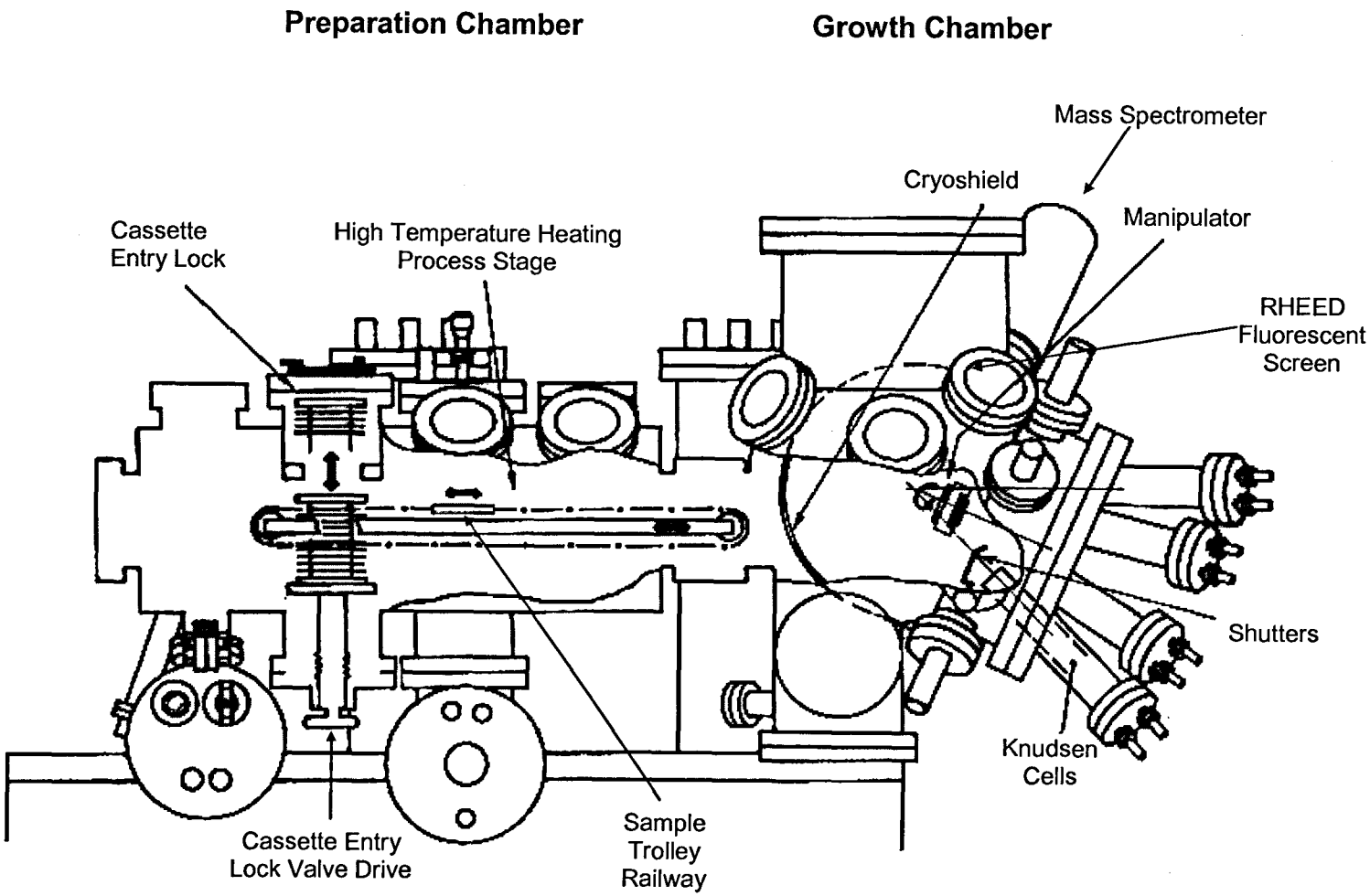

Figure 2.1: Schematic of V80H MBE system.

contaminants such as water, is done in the preparation chamber to prevent contamination of the growth chamber. The base pressure of the preparation chamber is 10^{-8} to 10^{-9} mbar. Easy transportation of samples is carried out through the use of a railway system, which can extend from the preparation chamber into either growth chamber.

In the growth chamber, working pressures of around 10^{-9} to 10^{-10} mbar are required to minimise contaminants. Such low pressure also means that the mean free path of the molecules effusing from the cells is larger than the dimensions of the chamber. Therefore only collisions between molecules and solid surfaces occur, rather than inter-molecular collisions which would cause scattering from the beam.

2.2.1 Vacuum Environment

The vacuum is maintained through the use of several pumps. Oil sealed rotary vane pumps are used to reduce the pressure from atmosphere to 10^{-3} mbar. These pumps work by drawing gas into the pump, compressing it before expulsion through the pump exhaust. Since the rotary pump is oil sealed it is necessary to place foreline traps between the vacuum system and the pump. This prevents the oil backstreaming [2].

Once the pumping limit of the rotary pump has been reached, turbomolecular pumps reduce the pressure still further. In a turbomolecular pump, the gas molecules collide with high speed rotating blades, causing the molecules to gain

momentum. These blades are also angled so that the gas can only leave the chamber [3].

Below a pressure of 10^{-6} mbar, ionisation pumps (Figure 2.2) are used to achieve pressures in the low 10^{-9} mbar region. There are three different processes in the operation of an ion pump which contribute to the pumping speed. First, electrons are emitted from the cathode into a magnetic field. Here they encounter and ionise the gas load from the vacuum chamber. Such ionised molecules are attracted to the cathode plates, become buried and sputter titanium on collision. Other gas molecules can adhere to the surface of the plates, and are subsequently buried by the sputtered titanium. Chemically active gases, such as oxygen and nitrogen, are also permanently removed from the vacuum system by titanium gettering. The main disadvantage of an ion pump is that it is not a displacement pump: the gas load is buried, not exhausted and can therefore be re-evolved [4].

Several additional methods are used to obtain a system pressure in the UHV regime. Bakeout of a stainless steel system reduces the pressure of the system by stimulating the desorption of water through thermal heating. Typical temperatures for bakeout of UHV systems are 180-200°C [5], however in the II-VI growth system at Heriot-Watt, bakeouts are carried out at 105°C for ~24 hours. This low temperature is used because we are limited by the vapour pressure of sulphur, selenium and silver iodide.

Outgassing of the source cells decreases the operating system pressure further, as heating the cells above their normal operating temperature removes other

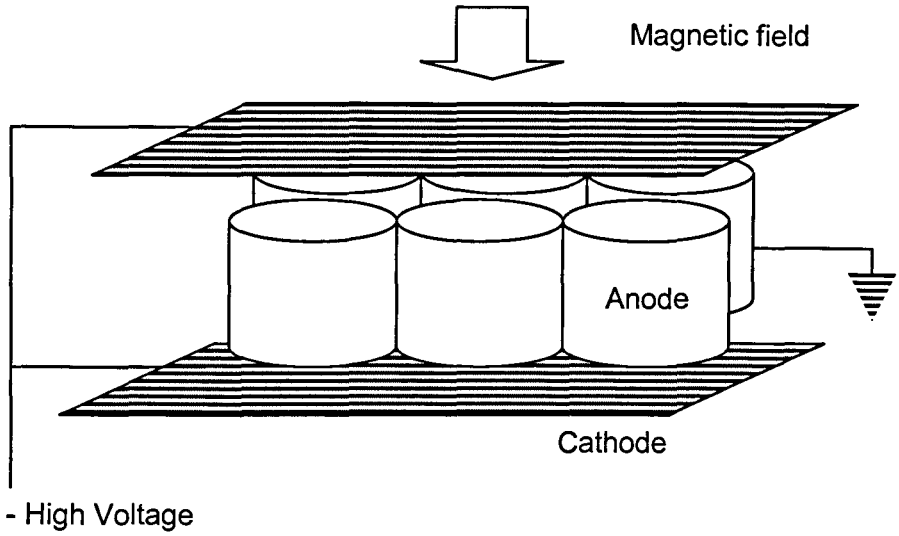

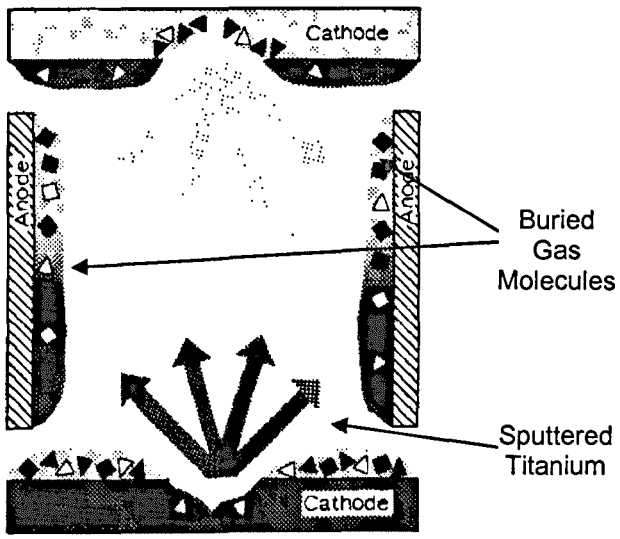

Figure 2.2: Diagram of the inside of an ionisation pump (top), and a schematic of the pumping mechanism of an ionisation pump. Electrons are emitted from the cathode and they ionise the gas load from the vacuum chamber. The ionised molecules are attracted to the cathode plates, become buried and sputter titanium on collision. Other gas molecules adhere to the surface of the plates, and are subsequently buried by the sputtered titanium.

contaminants (such as water). Further discussion of the outgassing procedure can be found in the section describing the use of the mass spectrometer in section 2.4.

When cells and the substrate heater are at growth temperature, a liquid nitrogen cooled cryoshield is used to improve the operating pressure in the growth chamber.

2.2.2 Pressure Measurement

Accurate pressure measurement is a fundamental requirement for vacuum systems. At Heriot-Watt, two types of pressure measurement gauges are used. Pirani gauges are used for monitoring the pressure in the main chambers as well as in the backing line between the Turbo and rotary pumps. The operational range of this type of gauge is from atmospheric pressure to 10^{-3} mbar. The UHV in the preparation and growth chambers is measured using Bayard-Alpert ionisation (ion) gauges [6]. The upper and lower limits of the ion gauge are 10^{-3} and 10^{-11} mbar respectively.

2.3 Growth Chamber

All the samples detailed in this thesis were grown in the HWA chamber of the V80H system. The source flange of the growth chamber (shown schematically in Figure 2.3) has eight ports for interchangeable thermal effusion Knudsen cells (K-

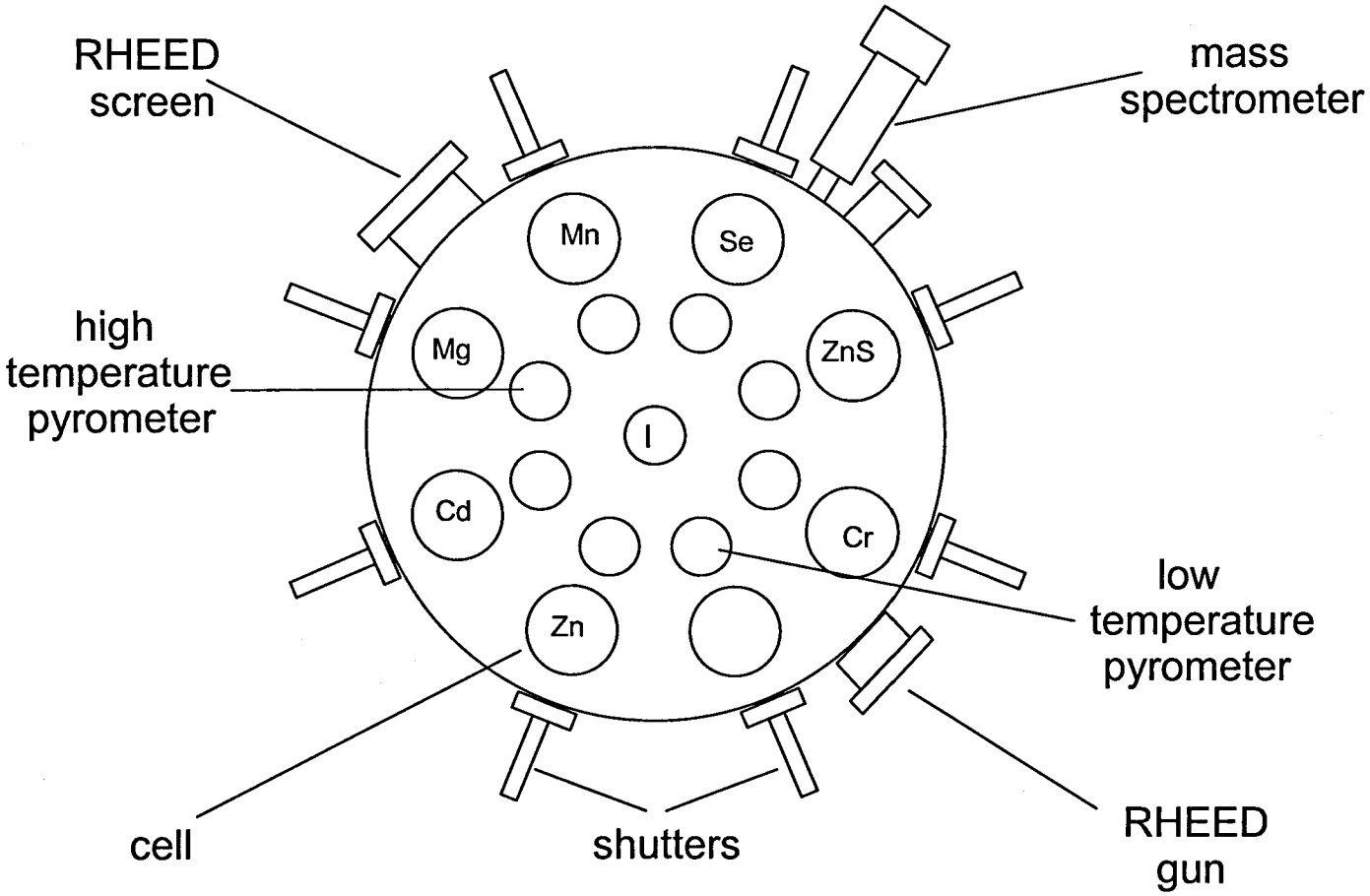

Figure 2.3: Diagram of the source flange of the MBE chamber, showing the position of the source cells during this thesis.

cell), as well as an Addon minicell containing silver iodide for iodine doping. Other ports on the chamber house pyrometers for measuring the temperature of the substrate during growth, a RHEED gun and a quadrupole mass spectrometer.

The source materials for II-VI semiconductor growth include elemental zinc, cadmium, selenium, and magnesium with purities of 6N; elemental 5N8 manganese and 5N chromium, and a compound source of 6N zinc sulphide.

2.3.1 Knudsen Cells

Individual temperature control of each K-cell is essential to allow growth of different materials, since the source flange contains nine different source materials and not all are required for the growth of each sample. The source material is contained in pyrolytic boron nitride (PBN) crucibles within the K-cells (Figure 2.4).

Each K-cell is heated independently by radiation from a resistively heated filament, coiled around the crucible. Heat shielding surrounds the filament to improve both the temperature stability and the thermal efficiency of the K-cell. Thermocouples, in contact with the crucible, monitor the temperature of the K-cell.

Proportional Integral Derivative (PID) temperature controllers measure the emf generated by each thermocouple and power the heating filaments accordingly. This feedback system can accurately control and maintain temperatures to ± 1K. The PID parameters of each cell can be individually tuned to minimise any

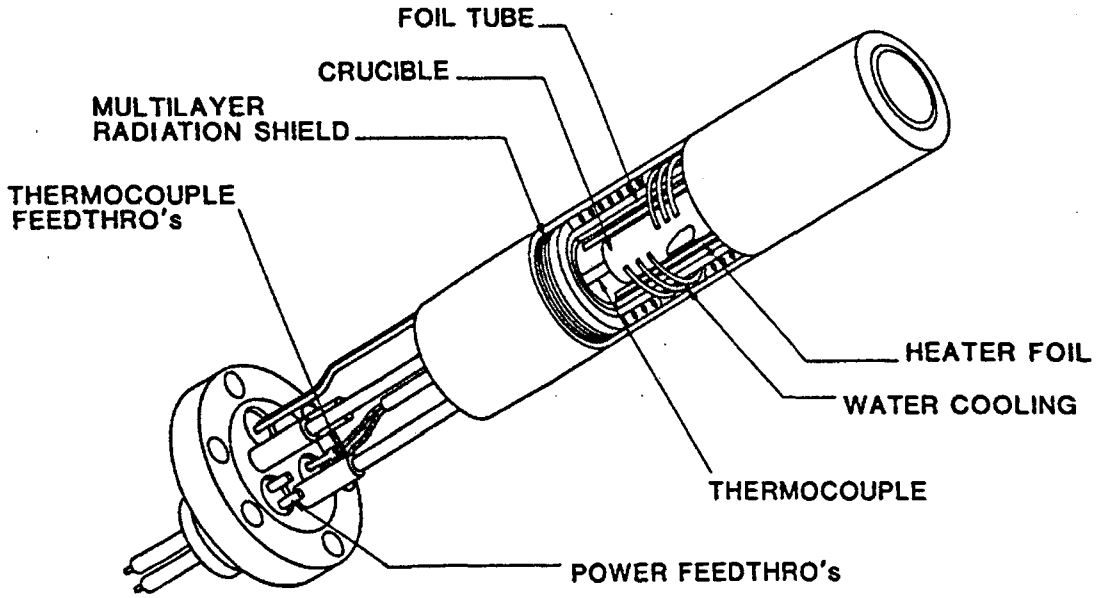

Figure 2.4: Diagram of a Knudsen cell. The internal water cooling pipes can be seen in the cut-away section. This type of cell is used for the ZnS, Mg and Cr sources.

oscillations and overshoots of the heater temperature. A water cooling system around the source flange ports assists in keeping the thermal crosstalk between the K-cells to a minimum. For the high temperature K-cells, ZnS, Mn and Cr, the water is also directed through an internal water cooling system as shown in Figure 2.4.

2.3.2 Shutters

In front of each K-cell, solenoid operated shutters control the molecular beams, these can be operated either manually or by a computer program for the growth of more complicated structures. The shutters are controlled by two solenoids; an AC current drives the magnetic core of the shutter to the open or closed position and a DC current holds the shutter in place. The time for the shutters to move is a fraction of a second, therefore the thickness of the layer can be controlled to within an atomic layer.

In order to prevent sulphur leaking round the shutter of the ZnS K-cell, the standard shutter was replaced by a liquid nitrogen cooled shutter. This also reduces the size of the cell aperture, and also aids in reducing the sulphur leakage.

Leakage around the shutters is a concern and is discussed in Chapter 4 with respect to MnS growth and Mn contamination. During this thesis, two further liquid nitrogen cooled shutters were installed in front of the Mn and Cr K-cells, to

eliminate potential Mn contamination and as a pre-emptive measure against Cr contamination.

2.3.3 Manipulator

The manipulator (Epicentre 282, UHV design) in the growth chamber can be rotated to three different positions (Figure 2.5). To allow easy loading / unloading of the sample position (1) is used, material flux measurements are taken when the manipulator is in position (2) and the growth position is illustrated in position (3).

The Epicentre 282 was installed in the HWA chamber in 1999. The advantages over the previous Vacuum Generators manipulator include the absence of a door to secure the molybdenum substrate holder in place. The new design has a horseshoe shape which the molybdenum block drops into, with a peg at the back of the horseshoe to secure it into place. Another advantage is that the new manipulator is approximately half to weight of the old design, making removal and re-installation during maintenance easier.

The manipulator allows the sample to be heated to high temperatures (600-700°C) for oxide desorption from the sample surface as well as heating to the growth temperature. In position (3), the manipulator rotates about the normal to the sample ensuring even growth over the sample surface.

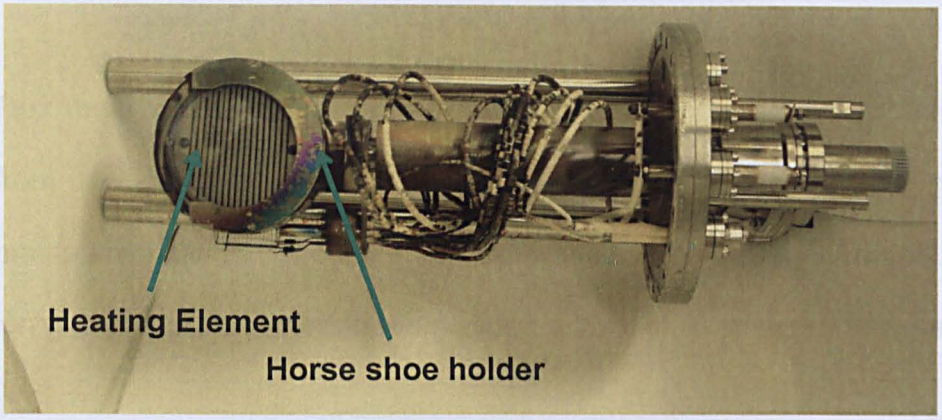

(1)

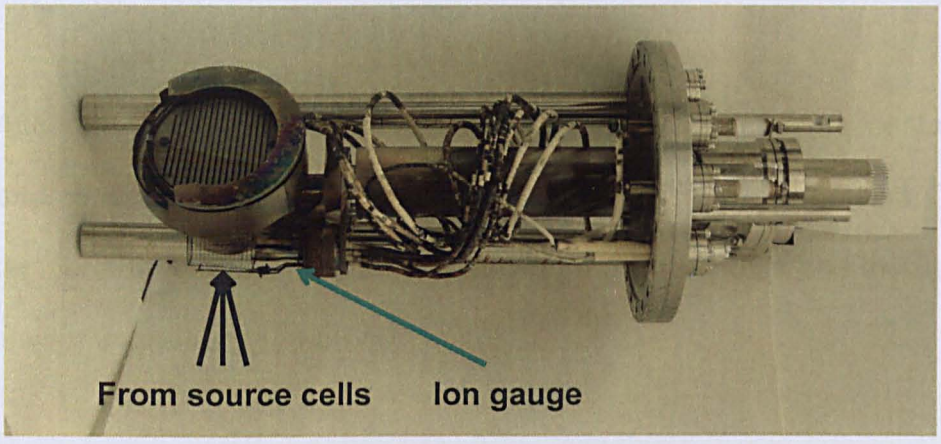

(2)

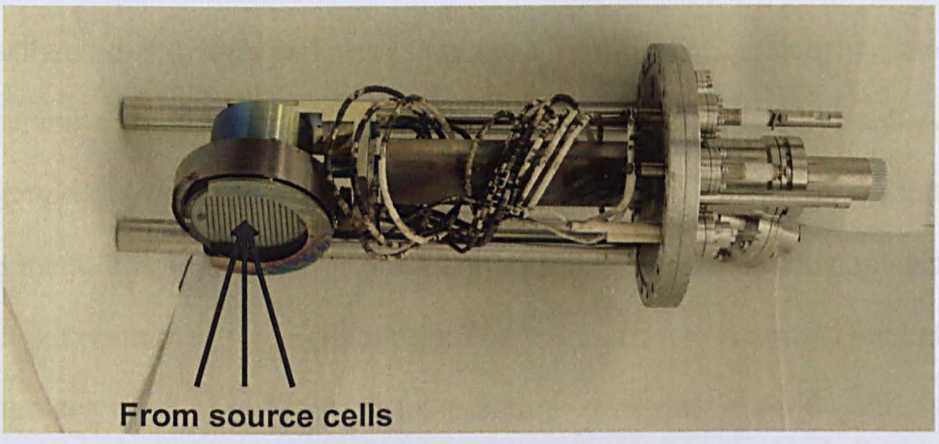

(3)

Figure 2.5: Photographs of an Epicentre 282 manipulator removed from B-end chamber, taken from the bottom of the chamber looking up. The source flange would be at the bottom of the photograph. Manipulator set up is a mirror image of the A-end set up. The heating element and horse shoe shape to hold the molybdenum block are indicated.

Substrate manipulator positions; (1) sample loading / unloading position, (2) flux measuring position with the ion gauge facing towards the source flange, (3) growth position with the sample surface facing cells.

Flux measurements are taken in order to monitor the amount of material effusing from the cells. In the flux measurement position (2), the ion gauge on the manipulator faces the cells. Each cell in use is then opened in sequence and the ion gauge current recorded. This allows a level of consistency between growths.

2.3.4 Substrate Temperature Measurement

Accurate temperature control of the substrate is required for a constant growth rate and to ensure the high crystal quality of the sample produced. The substrate temperature is measured by two means, a thermocouple and the use of high and low temperature pyrometers.

The particular thermocouple is made of tungsten/rhenium alloys, which can withstand the high temperatures used in the MBE system. A feedback system similar to that used in the operation of the K-cells is used to achieve the desired temperature of the substrate. Since the substrate needs to be rotated during the growth, it not possible for the thermocouple to be in the ideal position (which is in direct contact with the substrate). The thermocouple is placed behind the substrate heater, which produces a temperature offset of ~ 50°C with respect to the substrate surface. This offset can be affected by various factors, including the thickness and finish of the molybdenum substrate holder and the emissivity of the surface of the sample.

The use of infrared pyrometry as the second means of temperature measurement counteracts the problem of the temperature offset. The pyrometers operate on the principle that all objects emit radiant energy, and the intensity of such radiation is a function of temperature.

The HWA chamber is fitted with two ports for the Ircon Mirage pyrometers. The high temperature pyrometer, used to measure the temperature during the oxide desorption of the substrates, covers the range of 250°C - 700°C [7]. The low temperature pyrometer is used to measure the growth temperature of the samples, over a range 120°C - 310°C. Both the sensors detect the incident radiation from the indium, used to solder the substrate to the molybdenum block, convert it into an electrical signal, which is then linearised and scaled to the temperature range of the system by the detector.

The temperature indicated by the pyrometer may not be the true temperature due to several sources of error, which include transmission errors, due to the build-up of material on the pyrometer port window, and the errors incurred by incorrect emissivity settings. The build-up of material on the port window is minimised by regular cleaning when the MBE system is at atmospheric pressure for maintenance.

The most commonly used substrate at Heriot-Watt is GaAs, which has an emissivity of 0.4 when undoped and 0.6 when doped [8]. Since at any one time there are at least three different growth projects being carried out in the same

chamber, most of which used doped GaAs substrates, the emissivity setting of the pyrometer is kept constant at 0.6. The error associated with using the incorrect emissivity setting can be determined as follows, the incident photon flux Φ can be expressed as:

$$\Phi = A\varepsilon_T T_T^4 \qquad \text{Equation 2.1}$$

where A is the area of the sample being studied, ϵ_T is the true emissivity of the sample and T_T is the true temperature of the sample. The same photon flux can also be expressed as:

$$\Phi = A\varepsilon_F T_F^4 \qquad \text{Equation 2.2}$$

where ϵ_F is the incorrect emissivity setting and T_F is the false temperature reading. Equations 2.1 and 2.2 can be equated to give:

$$\varepsilon_T T_T^4 = \varepsilon_F T_F^4 \qquad \text{Equation 2.3}$$

Re-arranging gives:

$$T_T = T_F \sqrt[4]{\frac{\varepsilon_F}{\varepsilon_T}} \qquad \text{Equation 2.4}$$

Therefore the typical systematic error which would be incurred from using an emissivity of 0.6 instead of 0.4 would result in an underestimate of ~11%. In depth analysis of the pyrometers in the Heriot-Watt system is covered elsewhere [9].

2.4 Mass Spectrometer

In order to maintain a high quality vacuum environment, periodic checks of the residual gas present in the system are required. This is carried out using a quadruple mass spectrometer with Residual Gas Analysis (RGA) software, RGA for Windows. The software has several modes of use; leak check, bar chart and multi-trend, which are described here.

The system is periodically leak checked, in order to detect leaks to atmosphere. The *leak check mode* of the RGA software is tuned to detect the probe gas, in this case helium. The partial pressure of the probe gas is displayed on the screen as both a histogram and a continuous trace. The gas is then applied to the entire vacuum system, starting from the uppermost part of the machine, paying particular attention to flanges, feedthroughs and welds, until an increase in peak height is observed. Leak detection is aided by an audio tone with a frequency proportional to the peak height. This allows the tester to be out of sight of the screen during testing.

The RGA software also displays a general overview of the growth chamber pressure in the *bar chart mode*. This mode scans over a range of consecutive masses and displays the partial pressures as a histogram. The scan is performed on a single range and the partial pressures are plotted on a linear y-axis. The range is adjusted so that the largest peak will appear on the screen. The bar chart

is useful because it allows an overview of the residual gas in the system to be obtained and any anomalous elements present are easily detected. A library of mass spectra is available for use in this mode; it contains common mass spectra and can be extended to include custom spectra for the particular vacuum system.

Multi-trend mode in the RGA software is used to monitor the partial pressures of particular molecular masses over time. Up to twelve channels (masses) are scanned in sequence and plotted. Each channel can be plotted with a different scale.

This mode has been used extensively in the outgassing procedures of the Mn and Cr source materials, which are different to the other cells. As well as heating the cell to ~20°C above its operating temperature for typically one hour, the Mn and Cr cells are then cycled between a lower temperature (500°C) and their outgas temperature, as shown in Figure 2.6. This cycling procedure further purifies the source material. While the cell is at the lower temperature, contaminants and impurities diffuse to the surface of the material and segregate there. At higher temperatures these will alloy with the source material, however the sudden rise in temperature does not allow them to dissolve before they are evaporated from the surface of the source. The mass spectrometer is monitored during the high temperature phases of the cycling procedure. The hydrogen peak (mass 2) is rapidly increases when the metal sources are heated and the cycling process is continued until H_2 no longer dominates when the cell is at the higher temperature.

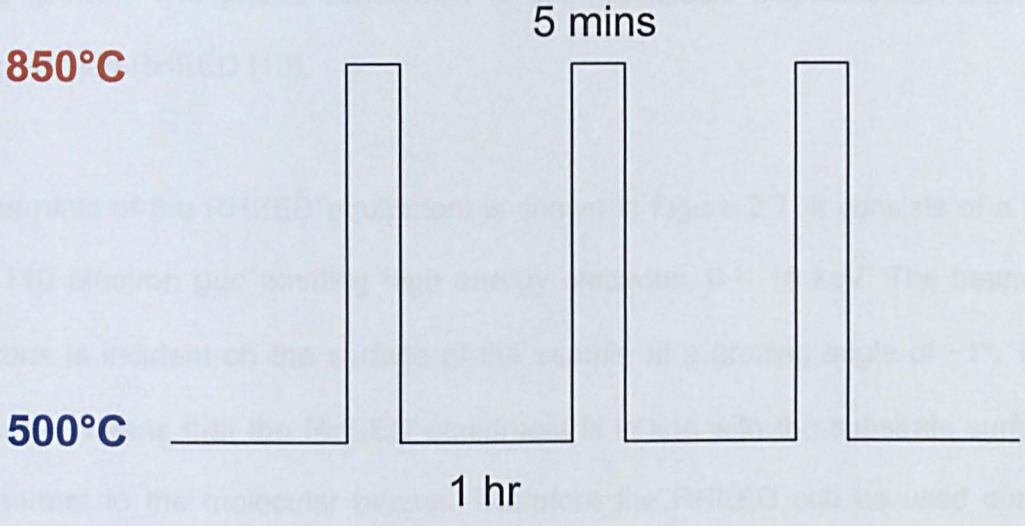

Figure 2.6: Temperature cycling of the Mn source used to remove contaminants and impurities from the source material.

2.5 RHEED

Reflection High Energy Electron Diffraction (RHEED) is a useful, *in situ*, analytical tool used during growth by MBE. It is used to observe the oxide desorption from substrates as well as monitoring the surface morphology both at the start of and during growth. The phase conversion of the metastable sulphides can also be observed with RHEED [10].

A schematic of the RHEED equipment is shown in Figure 2.7. It consists of a VG LEG 110 electron gun emitting high energy electrons, 0 – 15 keV. The beam of electrons is incident on the surface of the sample at a grazing angle of ~1°. The low angle means that the RHEED equipment is in line with the substrate surface and normal to the molecular beams. Therefore the RHEED can be used during growth as the set up does not block the cells and shutters. The low grazing angle also means that the electron beam only penetrates the uppermost monolayers of the sample, ensuring that only information about the surface of the layer is displayed in the RHEED pattern.

A phosphor coated screen is used to display the resulting diffraction pattern, the intensity of the diffraction pattern is converted into visible light. The use of a shutter behind the screen protects the coating when not in use.

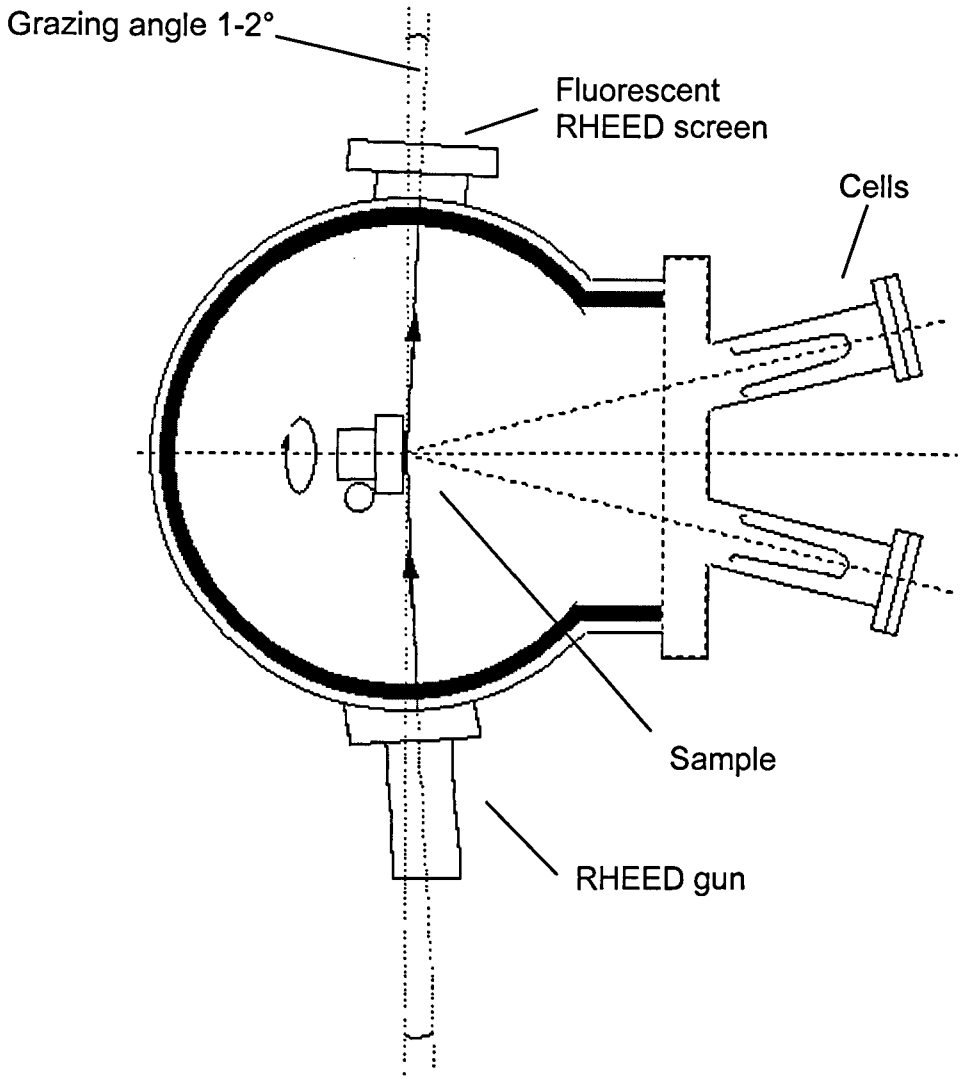

Figure 2.7: Schematic of the RHEED system used at Heriot-Watt. The electron beam is emitted from the RHEED gun at a grazing angle to the sample surface. It can be seen that the RHEED equipment does not interfere with the cells and therefore can be used during growth.

Electron Diffraction

When the electron beam hits the sample surface, it is scattered by the atoms in the periodic structure, generating spherical scattering waves. These waves interfere and cancel each other out in almost all directions. Constructive interference will only occur in a few directions which can be described in reciprocal space using the Laue conditions with reference to the Ewald sphere.

The Ewald sphere is a circle of radius $|\mathbf{k}_i|$, the incident electron wavevector, the origin of which is the center of the circle and the tip of $\mathbf{k}_i$ is the origin of reciprocal space (Figure 2.8). The scattering of the electrons is assumed to be elastic, therefore the magnitude of the diffracted wavevector $|\mathbf{k}| = |\mathbf{k}_i|$.

Diffraction occurs when the Laue conditions are satisfied, i.e. the wavevector of the electron coincides with the reciprocal lattice vector of a set of planes in the crystal as described by the Ewald sphere.

The diffraction pattern produced is determined by the periodicity of the crystal surface, since the electron beam only penetrates the upper few monolayers of the crystal, there is no periodicity in the direction normal to the surface. This means that the diffraction from the surface is the result of 2-D crystal interaction not 3-D, i.e. there is a relaxation of the third Laue condition. Due to this relaxation, the reciprocal lattice points become rods and where the rod crosses the Ewald sphere, diffraction may take place.

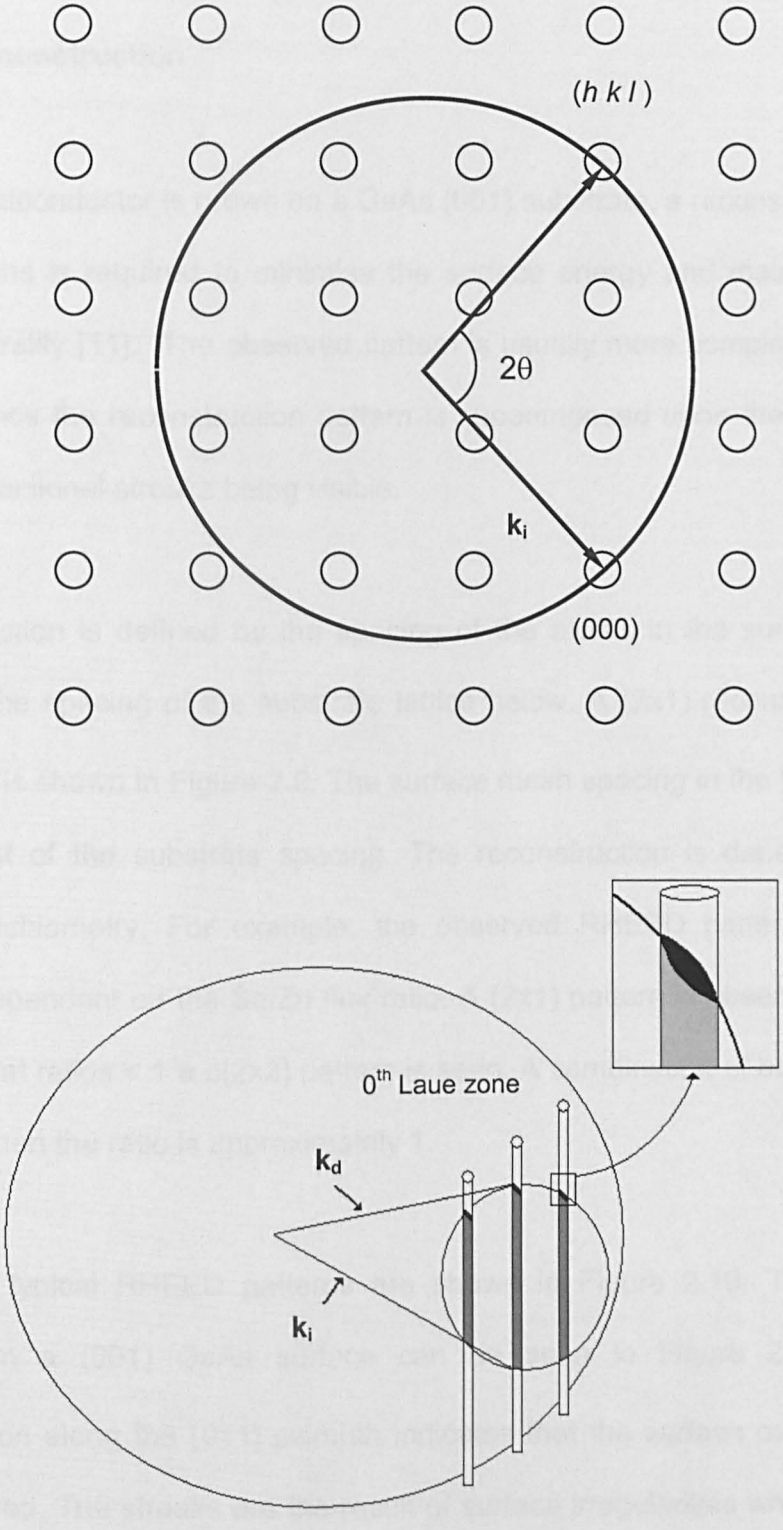

Figure 2.8: The Ewald sphere (top), $\mathbf{k_i}$ is the incident wavevector. Diffraction occurs where the reciprocal lattice intersects the Ewald sphere. The image at the bottom is a schematic of how the streaks are formed in RHEED patterns, $\mathbf{k_d}$ is the diffracted wavevector.

Surface Reconstruction

When a semiconductor is grown on a GaAs (001) substrate, a reconstruction of the surface atoms is required to minimise the surface energy and maintain average charge neutrality [11]. The observed pattern is usually more complex than that of the bulk, since the reconstruction pattern is superimposed upon the bulk pattern, leading to fractional streaks being visible.

A reconstruction is defined by the spacing of the atoms in the surface mesh in relation to the spacing of the substrate lattice below. A (2x1) reconstruction on a GaAs (001) is shown in Figure 2.9. The surface mesh spacing in the [$0\bar{1}1$] direction is twice that of the substrate spacing. The reconstruction is dependant of the surface stoichiometry. For example, the observed RHEED pattern from ZnSe growth is dependant on the Se/Zn flux ratio. A (2x1) pattern is observed when the ratio is > 1, at ratios < 1 a c(2x2) pattern is seen. A combination of both patterns is observed when the ratio is approximately 1.

Pictures of typical RHEED patterns are shown in Figure 2.10. The diffraction pattern from a (001) GaAs surface can be seen in Figure 2.10a, the 4x reconstruction along the [$0\bar{1}\bar{1}$] azimuth indicates that the surface oxide layer has been removed. The streaks are the result of surface irregularities which cause the reciprocal lattice rods to have finite width [12]. Figure 2.10b shows the RHEED diffraction pattern that is observed, along the [$0\bar{1}\bar{1}$] azimuth, during the growth of ZnSe. A rough (3-D) surface is depicted in the RHEED as a series of spots or

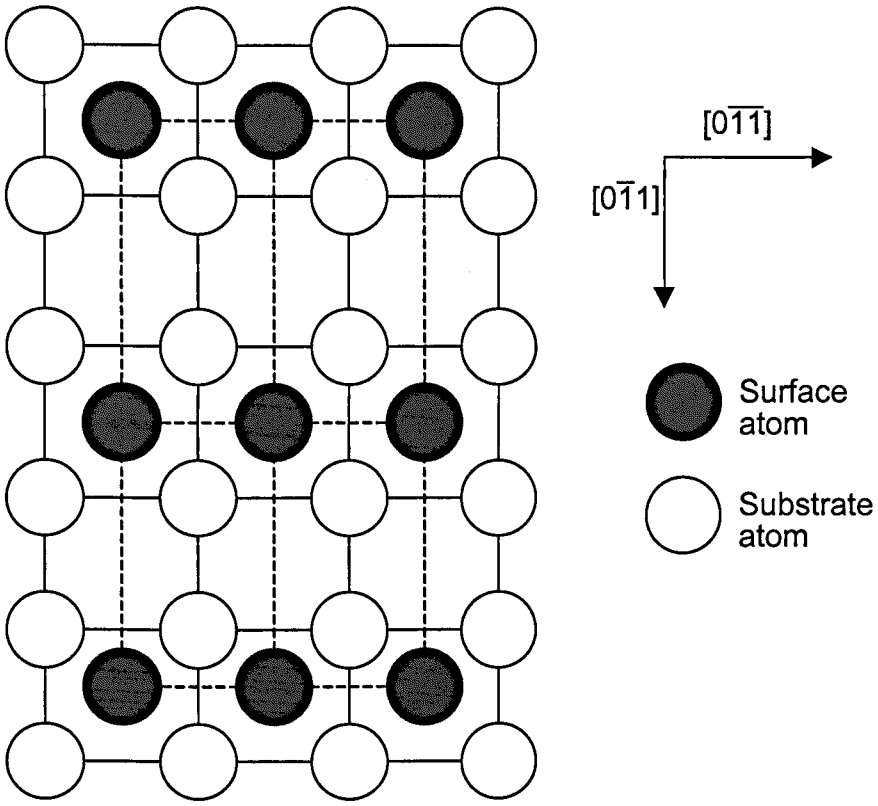

Figure 2.9: Schematic of surface atomic positions for a (2x1) reconstruction on a (001) surface.

Figure 2.10: RHEED diffraction patterns

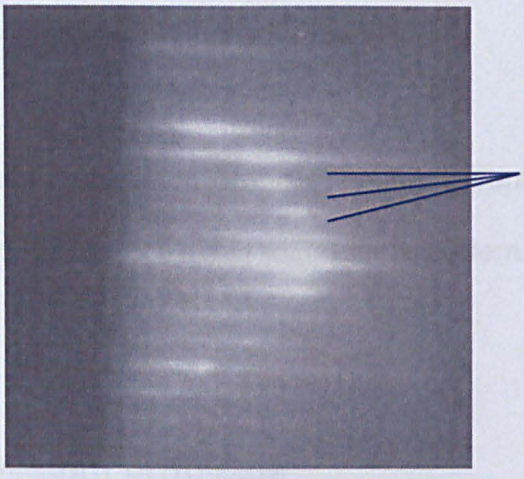

(a) - 4x reconstruction indicating that the surface oxide layer has been removed from the GaAs substrate.

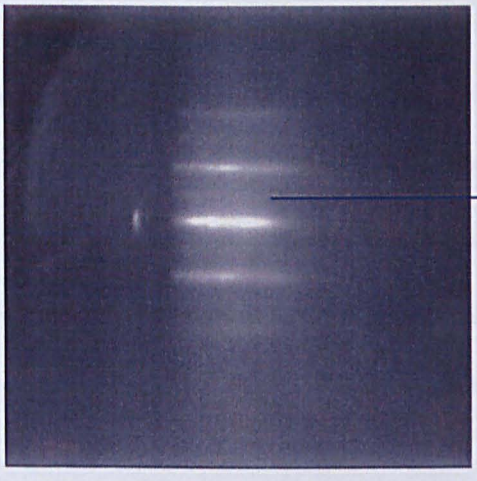

(b) - 2x reconstruction observed during the growth of ZnSe.

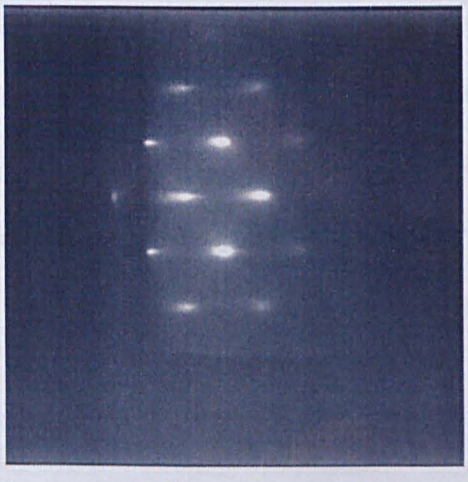

(c) - Spotty RHEED pattern indicating the onset of 3D growth.

chevron shaped features (Figure 2.10c) instead of the streaks typically observed during 2-D growth.

The phase conversion of the metastable from zinc blende to rocksalt can also be observed in the RHEED diffraction pattern. This will be discussed further in Chapter 4.

2.6 System problems

During the work on this thesis, growth of the metastable sulphides was hindered due to multiple equipment problems. In January 2004, the VAT gate valve connecting the A-end growth chamber to the preparation chamber had to be replaced as the bellows in the manual actuator developed a leak. The replacement valve was taken from the unused B-end chamber. Once the valve had been thoroughly cleaned, to avoid cross-contamination, it was incorporated into the system.

After this extended period of maintenance, normal operations resumed. However, photoluminescence (PL) of a ZnSe quantum well (QW) with MgS barriers, HWA1664 (Figure 2.11a), showed sub band gap energy emissions, indicating contamination of the sample. It was determined that the problem was in the MgS layer, as the low energy peaks were not present in the PL from single ZnSe layers. RHEED observations, during the growth of HWA1664, indicated that the growth was of good quality, with the streaky RHEED pattern present throughout the

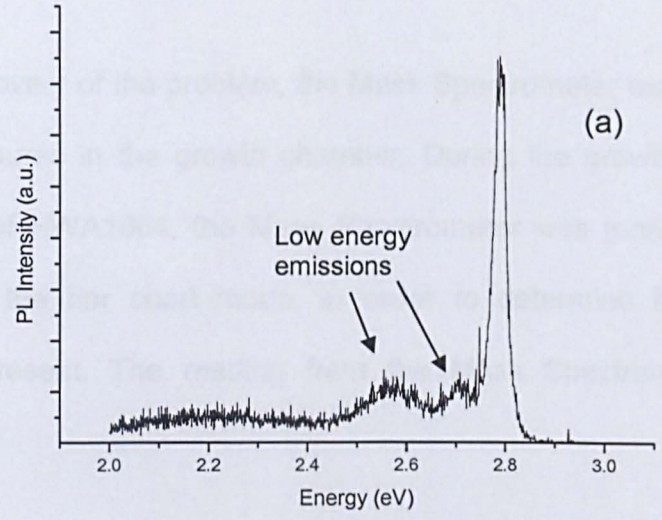

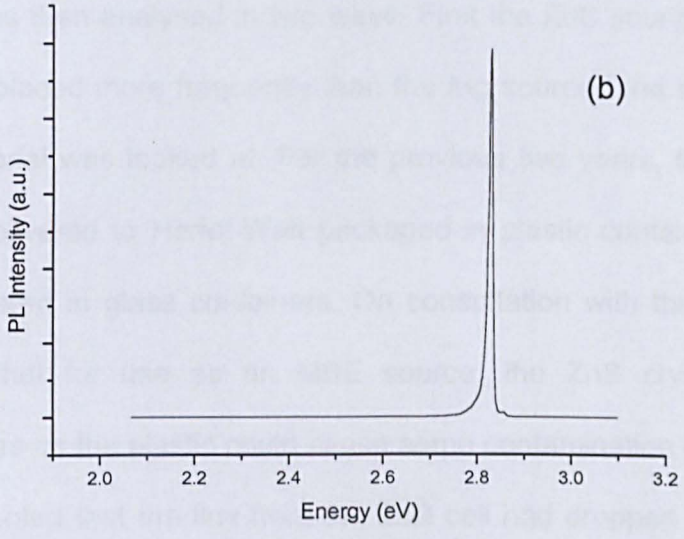

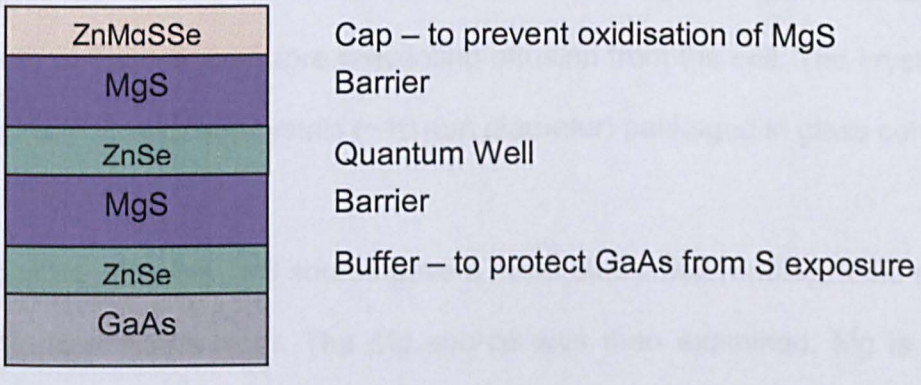

Figure 2.11: (a) Photoluminescence from HWA1664, a quantum well with the structure shown. The low energy emissions indicate that the sample has been contaminated. (b) Photoluminescence from HWA1795, a sample with the same structure as HWA1664. The ZnSe emission is sharp and there are no low energy emissions present indicating that the sample is of high quality.

growth. On discovery of the problem, the Mass Spectrometer was used to analyse the partial pressures in the growth chamber. During the growth of HWA1678, a repeat sample of HWA1664, the Mass Spectrometer was monitoring the growth chamber using the bar chart mode, in order to determine if there were any contaminants present. The reading from the Mass Spectrometer showed no unusual peaks.

The problem was then analysed in two ways. First the ZnS source was examined because it is replaced more frequently than the Mg source, and subsequently the Mg source material was looked at. For the previous two years, the 6N pure ZnS crystals were delivered to Heriot-Watt packaged in plastic containers, before this they were delivered in glass containers. On consultation with the suppliers, they recommended that for use as an MBE source, the ZnS crystals should be packaged in glass as the plastic could cause some contamination of the crystals. It had also been noted that the flux from the ZnS cell had dropped significantly and was erratic. Removal of the cell showed that the ZnS crystals had fused together at the mouth of the cell, therefore preventing effusion from the cell. The crystals were replaced with small ZnS crystals (~10 mm diameter) packaged in glass containers.

Although changing the ZnS source gave a more stable flux reading, it did not solve the contamination problem. The Mg source was then examined. Mg is a highly reactive material, which forms a protective oxide when exposed to air. The Mg in the source cell had been exposed to air repeatedly during routine maintenance of the machine. The material that was removed from the cell had an oxide coating over the surface (Figure 2.12) and was replaced with fresh ingots.

Figure 2.12: Photograph of Mg ingot removed from the Mg cell on 13/3/04. The surface of the ingot is covered with an oxide, which meant that the evaporating Mg surface was buried by an insulating protective layer.

Since the Mg and ZnS sources were replaced, the growth of MgS required reoptimisation. Subsequent PL of ZnSe QW's (Figure 2.11b) showed no sign of contamination, 10 months after initial breakdown of the system.

References

[1] A.Y. Cho, M.B. Panish and I. Hayashi, 3rd Int. Symp. on Gallium Arsenide and Related Compounds, The Institute of Physics, Cinference Series 9 (1970) 18

[2] Vacuum Generators Catalogue, Section 7-11 Foreline Traps – Introduction, (2005) 292

[3] Molecular Beam Epitaxy: Applications to key technologies, ed. R.F.C. Farrow, Noyes Publications, 1995

[4] S. Rutherford, Ion Pump Operation and Troubleshooting Guide, Duniway Stockroom Corp. (1997)

[5] C.T. Foxon and B.A. Joyce, Growth and Characterisation of Semiconductors, Edited by R.A. Stradling and P.C. Klipstein, Adam Hilger Bristol and New York, (1990) 35

[6] Vacuum Generators Catalogue, Section 8-06, Ion Gauge Heads – Introduction (2005) 312

[7] Mirage Temperature Measurement/Control System, Installation and Operation Manual, Ircon Incorporated (1994)

[8] K.A. Prior, Private Communication

[9] C. Bradford, PhD Thesis, Heriot-Watt University (2003)

[10] C. Bradford, K.A. Prior and B.C. Cavenett, Phys. Stat. Sol. (c) **1** (2004) 645

[11] E. A. Wood, J. Appl. Phys. **35** (1964) 1306

[12] P.J. Dobson. An Introduction to Reflection High Energy Electron Diffraction. Surface and Interface Characterisation by Electron Optical Methods, edited by A. Howie and U. Valdre. Plenum Press (1988) 159

Chapter 3: Characterisation Techniques

3.1 Introduction

In order to obtain complete characterisation of a semiconductor several aspects must be addressed. Analysis of the elemental, structural, optical, topographical and electrical properties give a complete picture of the characteristics of a semiconductor. In established systems, such as GaAs, elemental and structural analysis is not routinely required, however for new materials systems the characterisation must be methodical. Many different techniques are used to characterise the different aspects of a material. X-ray spectroscopy is non-destructive and can provide detailed information about the structural characteristics, such as the composition, thickness and quality of a grown layer. Optical spectroscopies, such as Photoluminescence (PL) can give information about the electronic structure of a material. Secondary Ion Mass Spectroscopy (SIMS) and X-ray Photoelectron Spectroscopy (XPS) provide information about the elements present in a layer. SIMS (discussed in Chapter 4) gives detailed information about the entire layer, while XPS is a surface sensitive technique. XPS is described in section 3.4, while the results from ZnSe and MnS layers will be discussed in Chapter 5. Another surface analysis technique used in this work is Atomic Force Microscopy (AFM), which produces a topographical scan of the sample surface.

This chapter outlines the different techniques used to characterise the II-VI semiconductors grown at Heriot-Watt including the MnS and CrS layers presented in this thesis.

3.2 X-ray Diffraction

X-Ray Diffraction (XRD) is a non-destructive characterisation technique which obtains structural information from the sample under study. The XRD technique used at Heriot-Watt is the Double Crystal X-Ray Diffraction (DCXRD) method. This has been widely used to determine the lattice parameter, relaxation and composition of structures [1]. In this work, XRD was used to optimise the growth of both MnS and CrS. The technique was also adapted to determine the growth rate of the samples produced, as discussed in the next section.

Diffraction occurs when waves interact with a regular structure whose repeat distance is about the same as the wavelength of the incident wave. The wavelength of X-ray radiation is of the order of a few angstroms (Å), the same as typical distances between crystal planes in solids. Bragg's law forms the basis of X-ray diffraction and states that it can be described as the reflection of plane waves off successive crystal planes [2].

The Bragg condition means that strong diffraction will occur when the angle of incidence of the X-rays results in a path length difference of an integral number of wavelengths between crystal planes. If the crystal planes are separated by a

distance, d, then the path length must be $2d\sin\theta$, leading to the Bragg equation: (see also Figure 3.1)

$$\lambda = 2d\sin\theta \qquad \text{Equation 3.1}$$

Where λ is the wavelength of the incident X-rays, d is the crystal spacing and θ is the incident angle of the X-rays.

There are two theories that can be used to describe X-ray diffraction: Kinematical and Dynamical, both of which will be described here briefly, for further information see references [3,4].

The Kinematical theory of XRD treats the scattering from each volume element in a crystal as independent, therefore the incident and diffracted beams are neither attenuated nor rediffracted. However this does not apply for a perfect or near perfect crystal with a large volume, as the summation of the scattering gives a diffracted intensity greater than the incident beam. Energy conservation laws require a different theory.

At Heriot-Watt, the BEDE RADS computer software uses the Dynamical theory as a basis to produce the simulation graphs. This theory is a solution of Maxwell's Equations for a model of a crystal lattice. Takagi [5] and Taupin [6] independently developed the theory to produce two coupled second order partial differentiation equations, representing the propagating wavefronts of the incident and diffracted

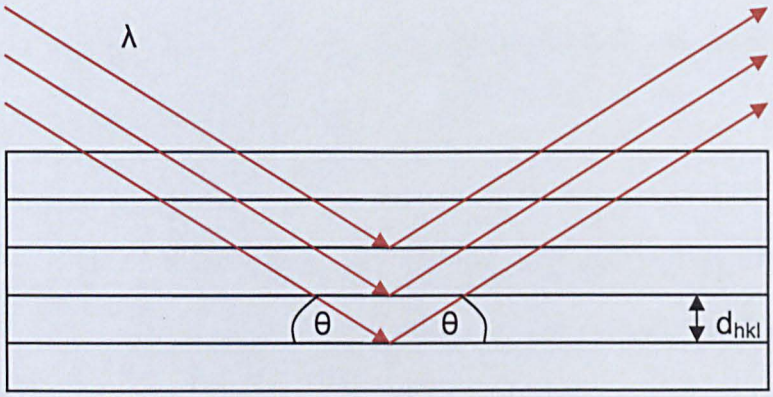

Figure 3.1: Bragg angle X-ray diffraction. X-rays of wavelength λ incident on crystal planes of spacing d_{hkl}, are strongly diffracted if incident angle is θ, the Bragg angle.

X-ray beams. Using analytical methods, these equations are used to predict the intensities of the incident and diffracted beams.

In order for the computer software to calculate accurate rocking curves, values of certain parameters of the crystal under analysis must be entered into the program, such as lattice parameter, density and Poisson's ratio.

Measurements of the intensity of the reflection of the X-ray beam are then compared to those produced by a simulation of the desired structure. The computer program iterates values for the thickness, composition and strain of the layers in the simulation until the theoretical results match the experimental ones, and the structural information can be determined. The simulation fit to the experimental data is measured by the standard error of the fit, a value calculated by the program, which is minimized through the iteration process to the best fit.

A schematic diagram of the Bede D200 X-ray kit, used at Heriot-Watt, is shown in Figure 3.2. It consists of an X-ray source, containing a copper target. The most intense radiation is the Cu $K\alpha_1$ line (1.5406Å). The radiation is randomly directed, and is only allowed to escape through a small (~2 cm diameter) circular beryllium window.

On leaving the source, the radiation is incident on a silicon crystal. This crystal has a channel cut into it to collimate the radiation [7]. Only X-rays impinging at the

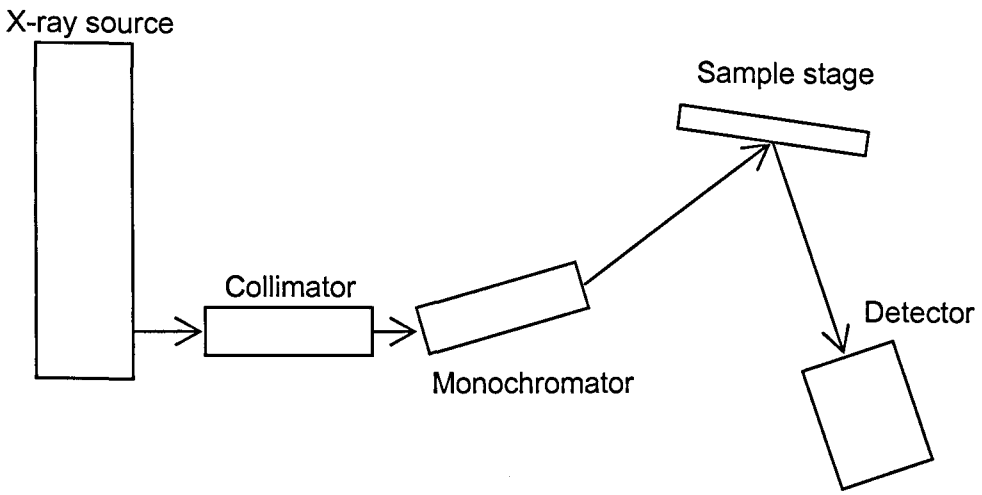

Figure 3.2: Schematic diagram of the Bede D200 X-ray kit used at Heriot-Watt.

correct angle will be diffracted through the channel and emerge from the crystal, all others are absorbed by the Si crystal.

The collimated X-rays are then incident on another (111) orientated silicon crystal, to monochromate the radiation. Since the X-rays are well collimated at this point, the Bragg condition is only satisfied for one wavelength for any given orientation of the monochromating crystal.

The collimated, monochromated X-rays are then incident on the sample. The sample stage is rotated about the Axis 2 (Figure 3.3) until the substrate peak is found. The substrate peak is the most intense peak unless the epilayers are over a micron thick. The sample stage and detector are rotated to optimize the diffracted peaks.

The sample stage has four degrees of freedom shown in Figure 3.3. The stage can be rotated around the incident beam so that the Bragg angle can be varied and rocking curve data taken. Since the samples under study are mounted for growth using indium, there can be uneven distribution of indium on the back of the sample. Although great care is taken when removing the sample from the molybdenum substrate holder after growth, occasionally the sample is not mounted flat on the stage. Rotating the stage around the Gonio 2 axis (Figure 3.3) corrects for the uneven mounting. The stage can also be moved backwards and forwards along the normal of the surface, this is important for maintaining sample position at the axis of rotation for samples with different thicknesses. It is also possible to rotate

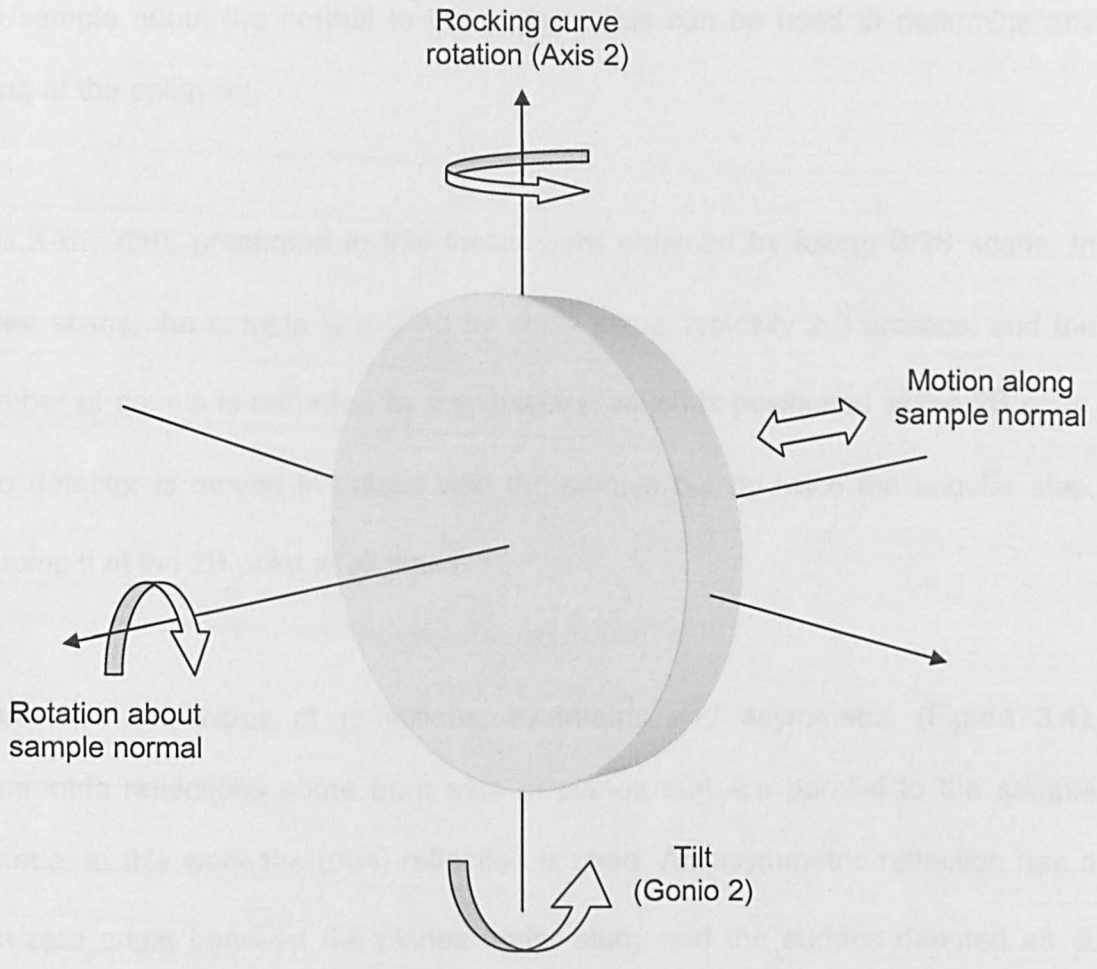

Figure 3.3: The sample stage indicating the four degrees of freedom available.

the sample about the normal to the surface, this can be used to determine any tilting of the epilayers.

The X-ray data presented in this thesis were obtained by taking $\theta/2\theta$ scans. In these scans, the sample is rotated by small steps, typically 2-3 arcsecs, and the number of counts is recorded by the detector, which is positioned at the 2θ point. The detector is moved in unison with the sample but by twice the angular step, keeping it at the 2θ point at all times.

There are two types of reflections, symmetric and asymmetric (Figure 3.4). Symmetric reflections come from sets of planes that are parallel to the sample surface, in this work the (004) reflection is used. An asymmetric reflection has a non-zero angle between the planes under study and the surface denoted as ϕ. This angle between the two planes, $(h_1k_1l_1)$ and $(h_2k_2l_2)$ can be found for a cubic crystal using:

$$\cos\varphi = \frac{h_1h_2 + k_1k_2 + l_1l_2}{\sqrt{h_1^2 + k_1^2 + l_1^2}\sqrt{h_2^2 + k_2^2 + l_2^2}} \qquad \text{Equation 3.2}$$

for a (001) surface this becomes

$$\cos\varphi = \frac{l_2}{\sqrt{h_2^{\,2} + k_2^{\,2} + l_2^{\,2}}} \qquad \text{Equation 3.3}$$

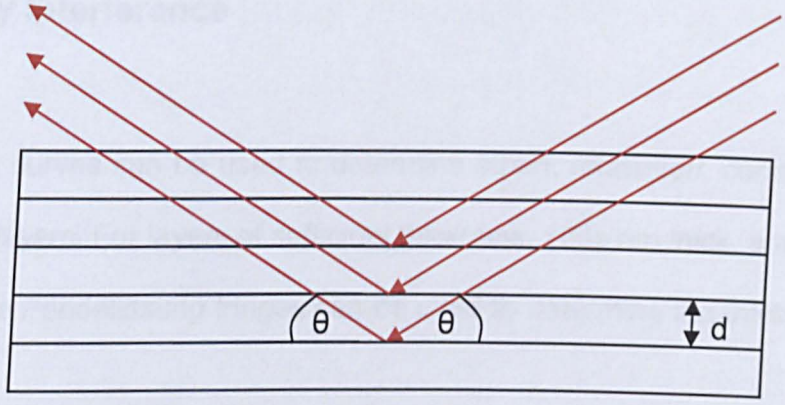

Symmetric reflection

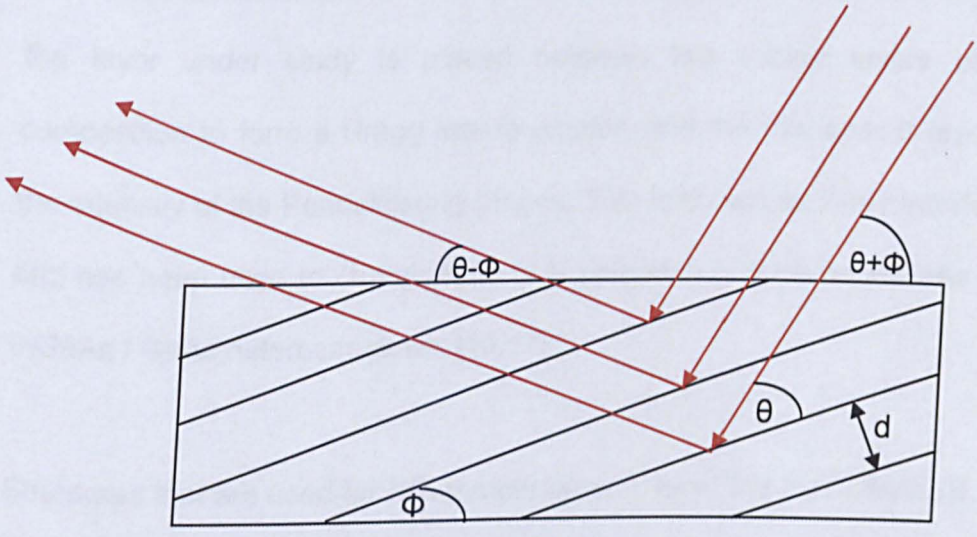

Asymmetric reflection

Figure 3.4: *Comparison of symmetric and asymmetric reflections, indicating the angles involved.*

3.3 X-ray Interference

XRD rocking curves can be used to determine strain, relaxation, composition and quality of epilayers. For layers of sufficient thickness, 100s nm thick, analysis of the spacing of the Pendellösung fringes can be used to determine the thickness of the epilayer [8,9].

Over the past 15 years, it has been demonstrated that DCXRC can be used to obtain thickness measurements for layers only nanometres thick. In this situation, the layer under study is placed between two thicker layers of a different composition to form a Bragg interferometer, and the thin spacer layer modulates the intensity of the Pendellösung fringes. This is known as X-ray Interference (XRI) and has been used to characterise III-V compounds such as AlGaAs / GaAs and InGaAs / GaAs heterostructures [10,11].

Structures that are used for XRI measurements have the form, A/B/C/B, where A is the substrate layer, B are cladding layers of equal composition and thickness and C is the thin layer under study. The spacer layer, C, introduces a phase shift between the diffracted rays from the two cladding layers, resulting in an interference pattern. The phase shift is dependent on the thickness of the spacer layer.

When there is no spacer layer present, the diffracted rays are in phase and the resulting X-ray diffraction is intense. As the separation between the cladding layers

is increased, the diffracted rays become progressively out of phase, and the interference reduces the X-ray intensity. Figure 3.5 shows the difference in rocking curves between a single ZnSe layer and a sandwich layer of ZnSe and MgS.

When the diffracted rays are completely out of phase, there is destructive interference. This occurs at a phase change of π, with constructive interference occurring when the phase change is increased to 2π. The 2π phase change corresponds to a physical separation equal to the (004) interplanar spacing of cladding layer B.

Each plane of spacer layer C introduces a phase change of $2\pi m^*$, where m^* is the effective mismatch between layers B and C. The XRI pattern produced is repeated when N extra planes of C are inserted into the structure, where $N = 1/m^*$ and corresponds to a thickness t. The repeated cycles of constructive and destructive interference with increasing spacer layer thickness, introduces an ambiguity to the results from the XRI technique. There are ambiguous results for the thickness of the spacer layer as the XRI pattern for a thickness x is identical to the pattern for a thickness $y = x + nt$, where n is an integer.

In order to uniquely identify the spacer layer thickness, the rocking curves from two different reflections must be analysed. The different reflections have different planar spacing, and therefore a different repeat period for the XRI patterns.

It has been suggested by Tanner [11] that in order to determine significant differences in the rocking curve, a phase change of $\pi/16$ is required. This means

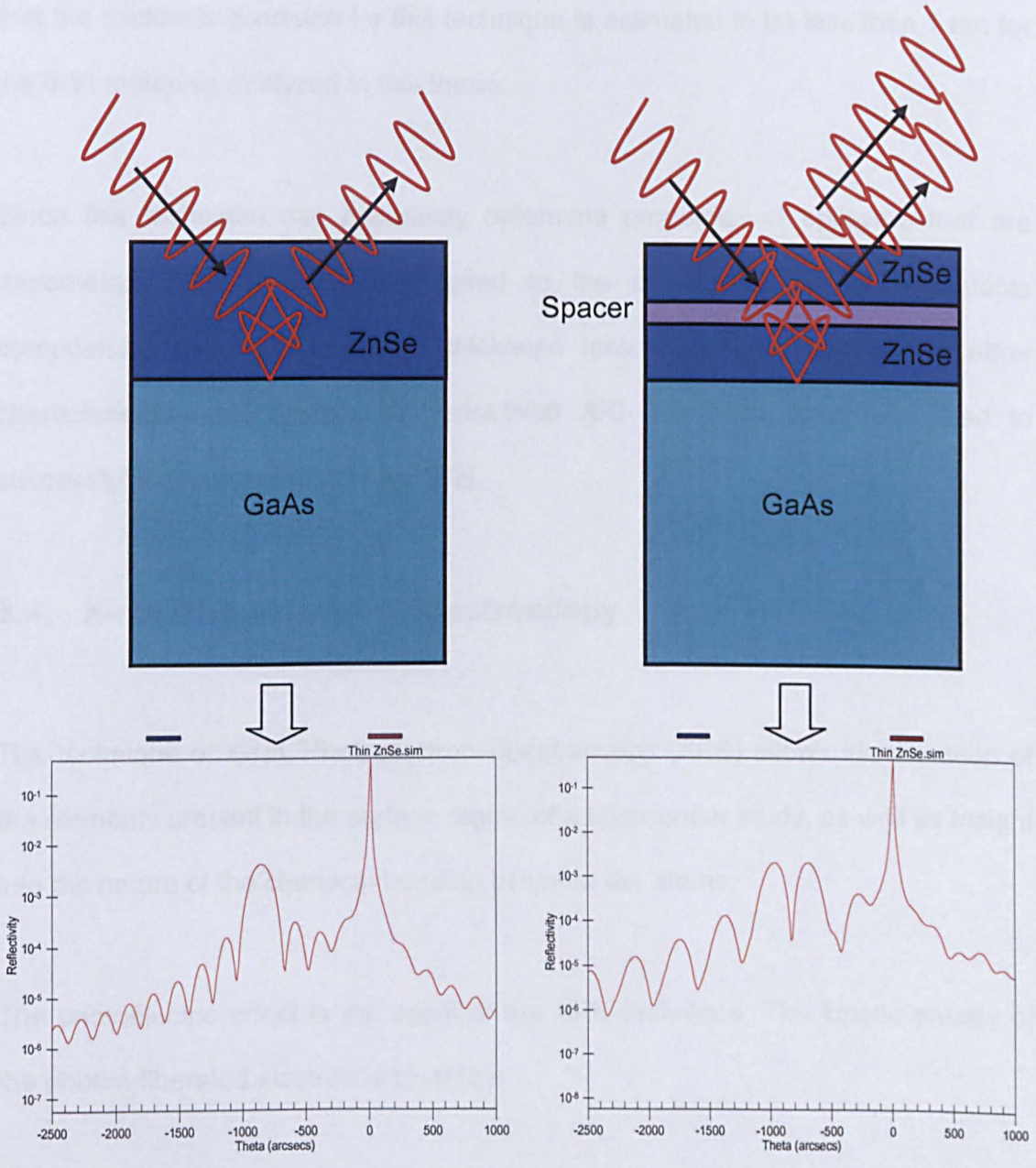

Figure 3.5: X-ray simulations and structures of a ZnSe epilayer and a ZnSe / Spacer / ZnSe multilayer, showing the effect the spacer layer has on the X-ray scan.

that the thickness precision for this technique is estimated to be less than 1 nm for the II-VI materials analyzed in this thesis.

Since this technique can accurately determine properties of epilayers that are nanometers thick, it is ideally suited to the characterisation of metastable compounds that have a critical thickness less than that required for other characterisation techniques. At Heriot-Watt XRI has been previously used to successfully characterise ZB MgS [12].

3.4 X-ray Photoelectron Spectroscopy

The technique of X-ray Photoelectron Spectroscopy (XPS) allows identification of the elements present in the surface region of a layer under study, as well as insight into the nature of the chemical bonding between the atoms.

The photoelectric effect is the basis of the XPS technique. The kinetic energy of the photon-liberated electron is given by:

$$E_{KE} = hv - E_{BE} \qquad \text{Equation 3.4}$$

Where E_{KE} is the kinetic energy of the emitted electron, hv is the x-ray photon energy and E_{BE} is the binding energy of the electron in the parent atom referenced to the vacuum level.

The sample under analysis is irradiated by monochromatic x-ray radiation. Energy is transferred to the core-level electrons of the atoms present, and photoelectrons are emitted. These emitted photoelectrons are then separated according to energy and counted. The energies of the photoelectrons are related to the atomic and molecular environment from which they originated, various bonding configurations (both with its own and different elements) affect the energy of the emitted photoelectron. The number of electrons emitted is related to the concentration of the emitting atom in the sample.

The sampling depth available with XPS is approximately 3 monolayers [13]. This is due to the escaping electrons, from deeper in the sample than 3 monolayers, losing part of their kinetic energy before reaching the sample surface through collisions with the crystal.

All the XPS spectra reported in this thesis were obtained using a Scientia ESCA300 spectrometer shown in Figure 3.6. The system forms part of the National Centre for Electron Spectroscopy and Surface Analysis (NCESS), formerly known as the Research Unit for Surface, Transforms and Interfaces (RUSTI), at the Central Laboratory of the Research Councils' Daresbury laboratory, and is operated on a daily basis by Dr. Graham Beamson.

X-rays are generated using one of two 8 kW sources; Al-Kα (1.49 keV) or Cr-Kβ (5.95 keV); in this case the Al-Kα source was used. The X-rays are then monochromated by seven toroidally bent α-quartz crystals, which focus the

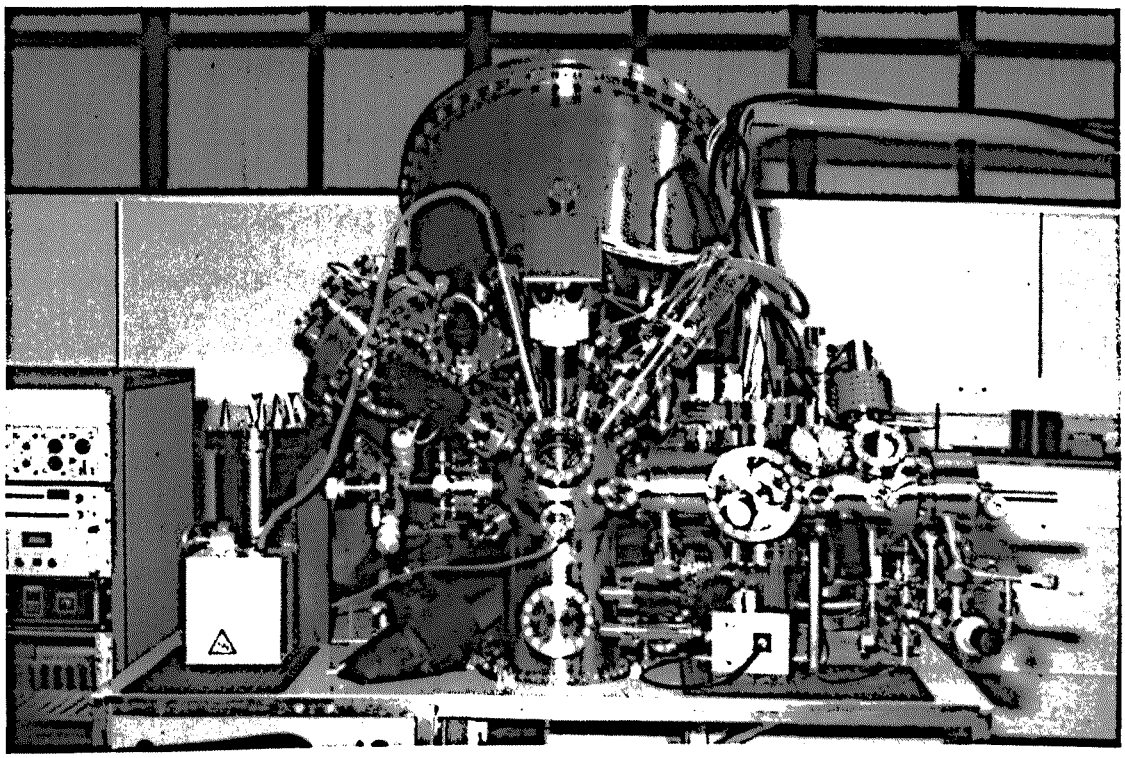

Figure 3.6: The Scientia ESCA300 X-ray Photoelectron Spectrometer.

radiation to a 6 x 1 mm area of the sample. The emitted photoelectrons are focused using an electrostatic lens. The energy of the electrons is then measured using a 300 mm hemispherical analyzer, and the resulting spectrum recorded on a PC using the Scientia ESCA300 software.

The samples were mounted on VG ESCALAB MkII stainless steel stubs using screws since the samples required heating to remove the Se cap. Wobble sticks are used to transport the mounted samples from the fast entry lock (atmosphere $\rightarrow$ $1x10^{-6}$ mbar) to the preparation chamber (< $2x10^{-8}$ mbar). The preparation chamber has two methods of heating the samples; an electron-beam heater can increase the temperature of the sample to 1000°C, however in this case, only the resistively heated sample stage was required to heat the samples to ~275°C.

A railway is then used to transfer the samples to the analysis chamber. Once there the sample is mounted onto a high precision manipulator, then orientated into the path of the incident radiation.

Initially a broad spectrum survey scan, across the full range of energies (0 eV – 1200 eV), is taken to identify the elements present. Based on the information provided by this scan, higher energy resolution regional spectra are taken over longer time intervals to improve the signal to noise ratio. Examples of broad and regional scans can be seen in Figure 3.7. The peaks identified in the regional scans are then analyzed by de-convolution, using the ESCA300 software provided by NCESS.

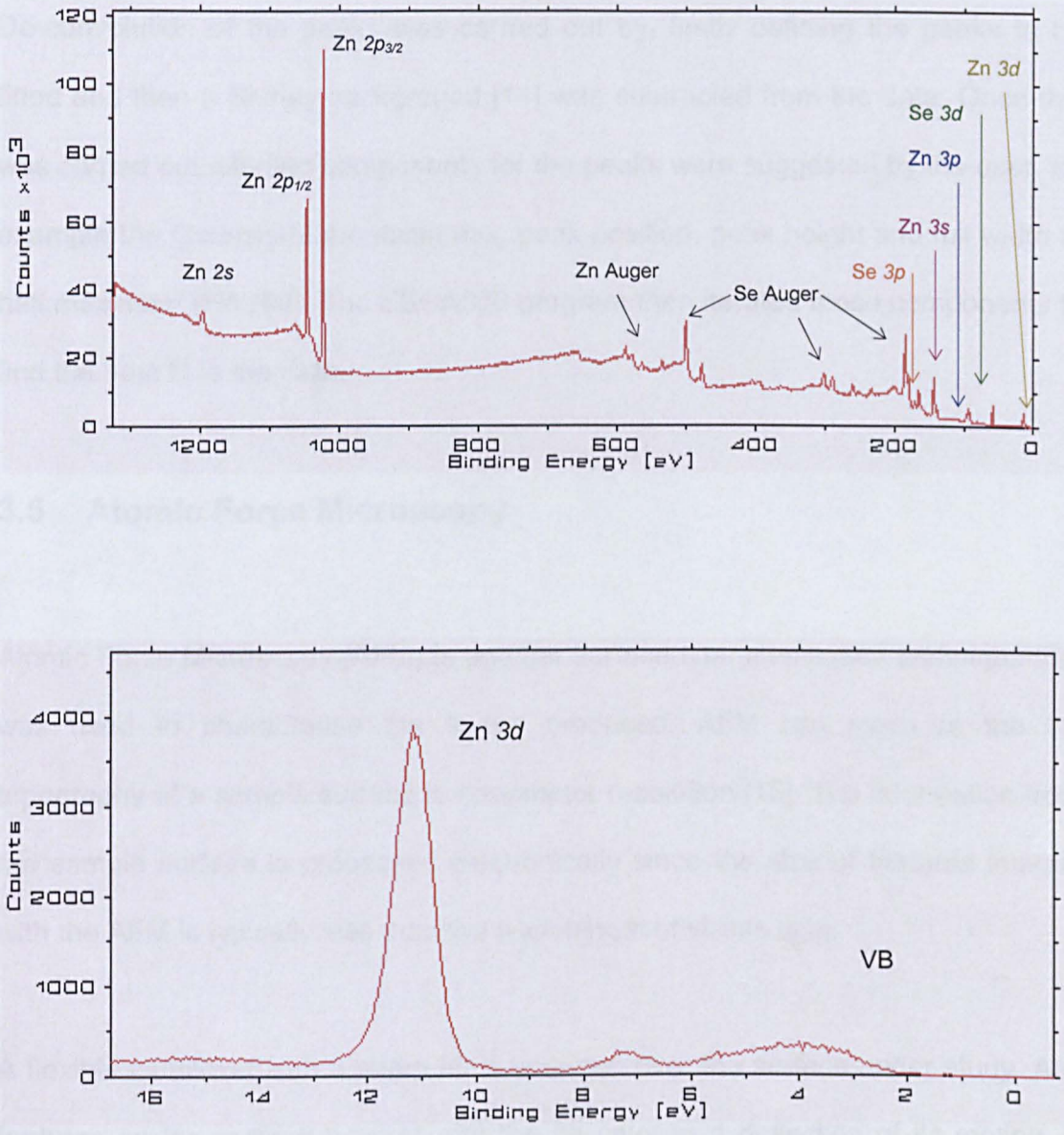

Figure 3.7: The upper graph shows the broad XPS scan for HWA1530, a 50 nm layer of ZnSe. The lower graph is a regional scan of the same sample. The peak labels were determined from the Binding Energy Lookup Table, www.xpsdata.com.

De-convolution of the peaks was carried out by, firstly defining the peaks to be fitted and then a Shirley background [14] was subtracted from the data. Once this was carried out, starting components for the peaks were suggested by the user, for example the Gaussian-Lorentzian mix, peak position, peak height and full width at half maximum (FWHM). The ESCA300 program then iterated these components to find the best fit to the data.

3.5 Atomic Force Microscopy

Atomic Force Microscopy (AFM) is another surface characterisation technique that was used to characterise the layers produced. AFM can measure the 3D topography of a sample surface to nanometer resolution [15]. The information from the sample surface is processed electronically since the size of features imaged with the AFM is typically less than the wavelength of visible light.

A flexible cantilever with a sharp tip is scanned over the surface under study. Any features on the surface interact with the tip causing a deflection of its motion. A split photodiode detector records this deflection via a laser beam. The detected signal is used to control the tip–sample interaction via an electronic feedback loop.

There are several different modes in which the AFM can be operated, the most common being Contact mode and Tapping mode. The images presented in this

thesis were collected using the Dimension™ 3100 Atomic Force Microscope at Heriot-Watt in either Contact mode or Tapping mode.

In Contact mode, the tip is in constant contact with the sample (Figure 3.8). The tip is attached to the end of a cantilever that has a low spring constant, lower than the effective spring constant holding the atoms of most solid samples together. As the scanner traces the tip across the sample with a force in the range of nN [15,16], the contact force causes the cantilever to bend and the feedback loop works to maintain a constant cantilever deflection.

Most surfaces, when in ambient air conditions, have a layer of condensed water vapour covering the surface, typically nanometers thick. When the tip touches this layer a meniscus forms and surface tension pulls the tip down into the layer. Electrostatic charge on the tip and sample can produce additional adhesive forces. The dragging motion of the tip combined with the adhesive forces between the tip and surface can cause damage to both the surface and tip and create artifacts in the image.

During a scan in Contact mode, a constant deflection is maintained between tip and sample by the feedback control loop. If the measured deflection varies from that required, a voltage is applied to the piezo crystal on which the cantilever is mounted. This voltage change adjusts the height of the scanner relative to the surface in order to maintain the desired deflection. The change in voltage is recorded, as it is a direct measure of the height of the features on the sample surface.

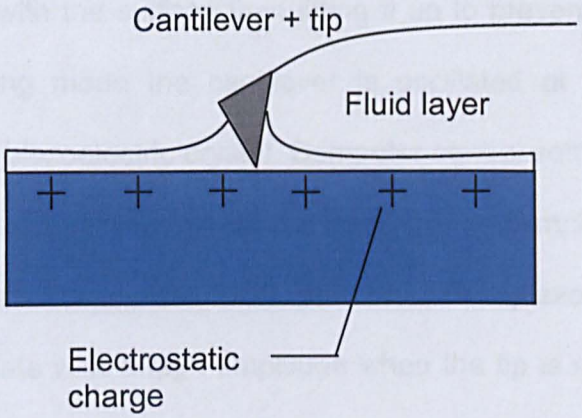

Figure 3.8: Schematic of the interaction between the AFM tip and surface during Contact mode operation.

Tapping mode overcomes the limitations of Contact mode by alternately placing the tip in contact with the surface then lifting it up to prevent dragging across the surface. In Tapping mode the cantilever is oscillated at or near its resonant frequency using a piezoelectric crystal. Computer control software is used to select the optimal oscillation frequency and the force on the sample is automatically set and maintained at the lowest level possible. The piezo motion causes the cantilever to oscillate with a high amplitude when the tip is not in contact with the surface. The tip is then lowered towards the surface until it begins to tap the surface (Figure 3.9). During a scan the oscillating tip contacts the surface and lifts off at a frequency of between 50,000 and 500,000 cycles per second.

As the tip begins to tap the surface, the amplitude of the oscillation is reduced due to energy losses caused by contacting the surface. The cantilever oscillation amplitude is maintained by feedback loop. When the tip passes over a raised area, the cantilever has less room to oscillate and the amplitude decreases. Conversely, when the tip passes over a depression, the amplitude increases since there is more room for the cantilever to oscillate. The oscillation amplitude of the tip is measured and the feedback loop adjusts the tip-sample separation to maintain a constant amplitude. This adjustment is recorded and is used to produce the surface topography image.

Although the use of Tapping mode overcomes many of the limitation of Contact mode AFM, there are limitations associated with the tip itself that must be considered. The pyramidal shape of the tips (Figure 3.10) is problematic for

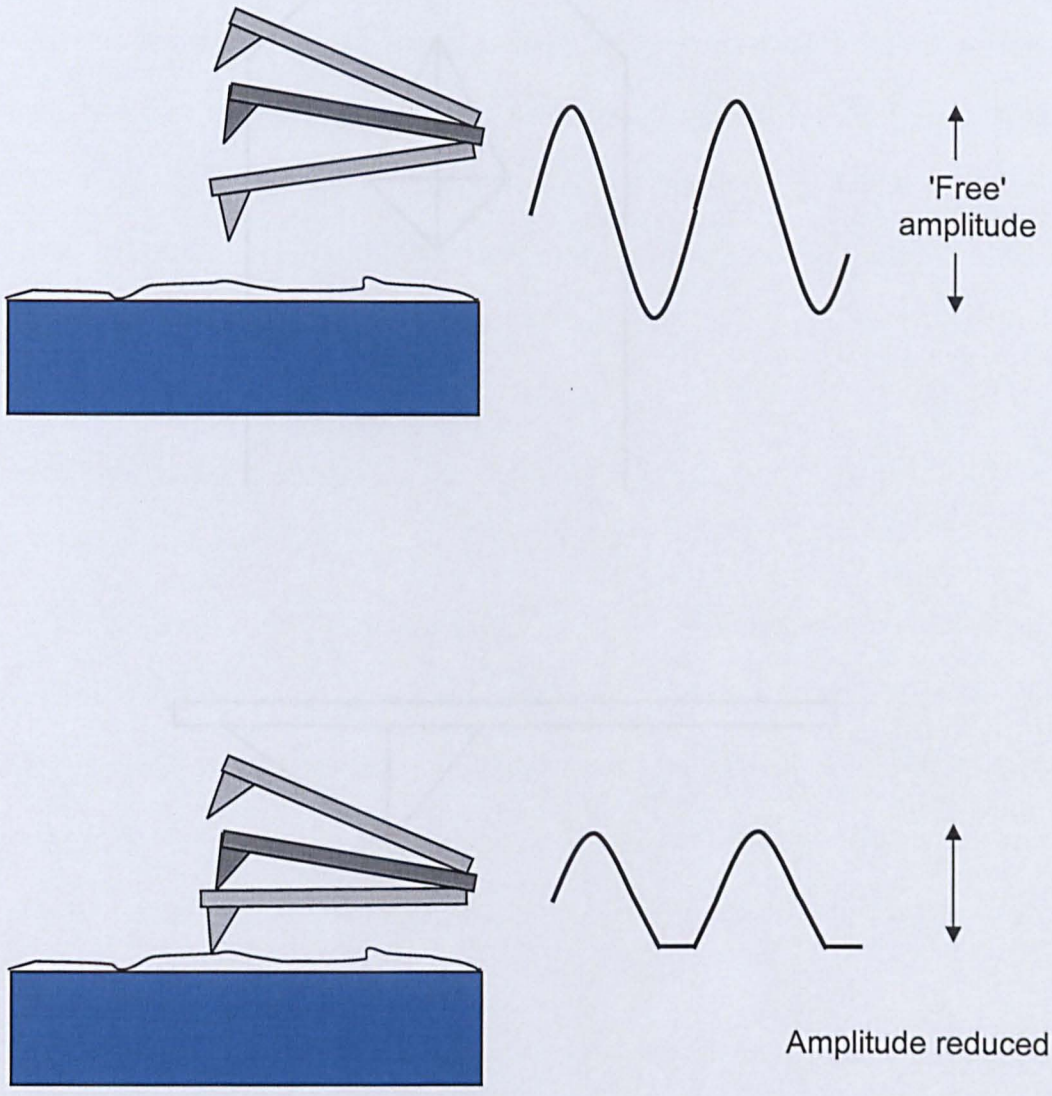

Figure 3.9: Diagram of cantilever oscillation in Tapping mode operation.

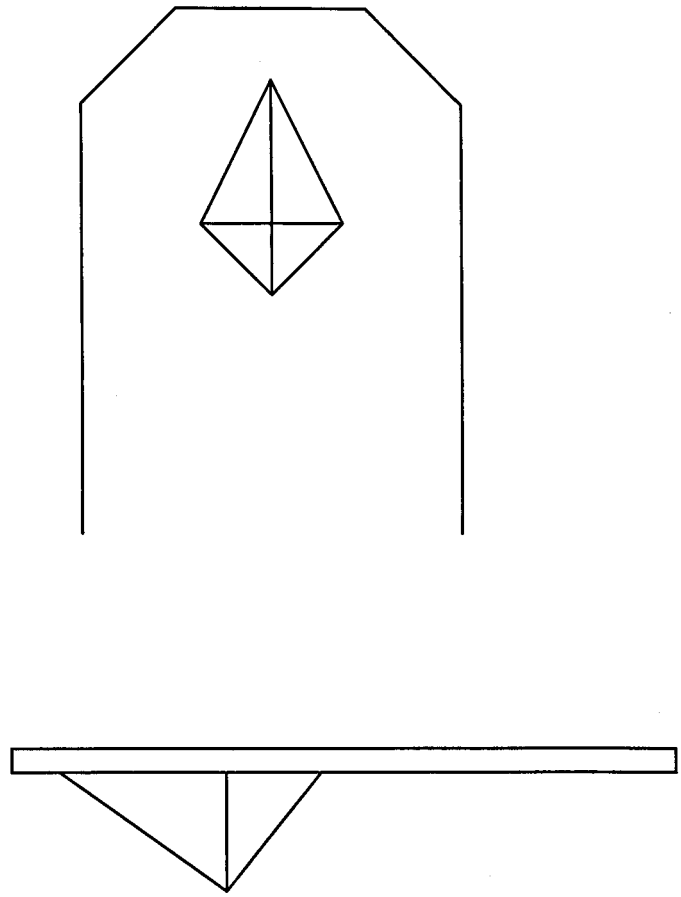

Figure 3.10: Schematic of the pyramidal shape of the cantilever tips used for AFM scans.

imaging certain types of features. Those surfaces with a step type feature are difficult to image because the sloped side of the tip interacts with the step before the apex reaches the edge of the step, as demonstrated in Figure 3.11. Features that are smaller than the radius of curvature of the tip are imaged as being broader than in reality. This is similar to the step surface problem in that the side of the tip makes contact with the feature before the apex.

3.6 Photoluminescence

Photoluminescence (PL) spectroscopy is a non-contact, non-destructive characterisation technique. Samples are optically excited by laser radiation incident on the sample surface. The laser radiation must have energy greater than that of the band gap of the semiconductor under study in order to excite the electrons out of the valence band into the conduction band, leaving holes in the valence band.

The electrons decay through non-radiative processes to the lowest energy level in the conduction band. When the electron and hole pair recombine, a photon is released (Figure 3.12), the energy and intensity of which indicates the quality of the material under study.

The electron hole pair may form a bound state known as an exciton. This usually occurs in high quality materials. The recombination of an exciton produces a sharp peak in the PL data at an energy equal to that of the band gap less the binding energy of the exciton. Excitons can also be created which are bound to defects

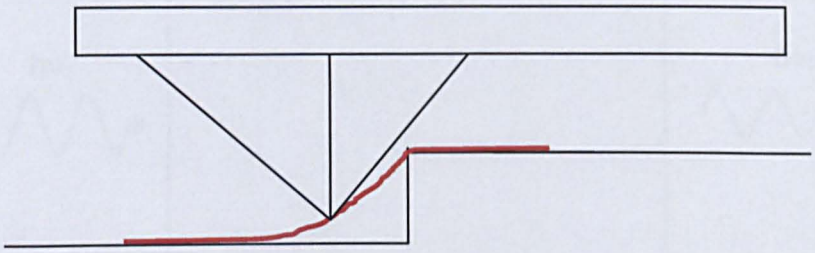

Figure 3.11: Diagram showing how the pyramidal shape of the tip limits the ability of the AFM to accurately image step features.

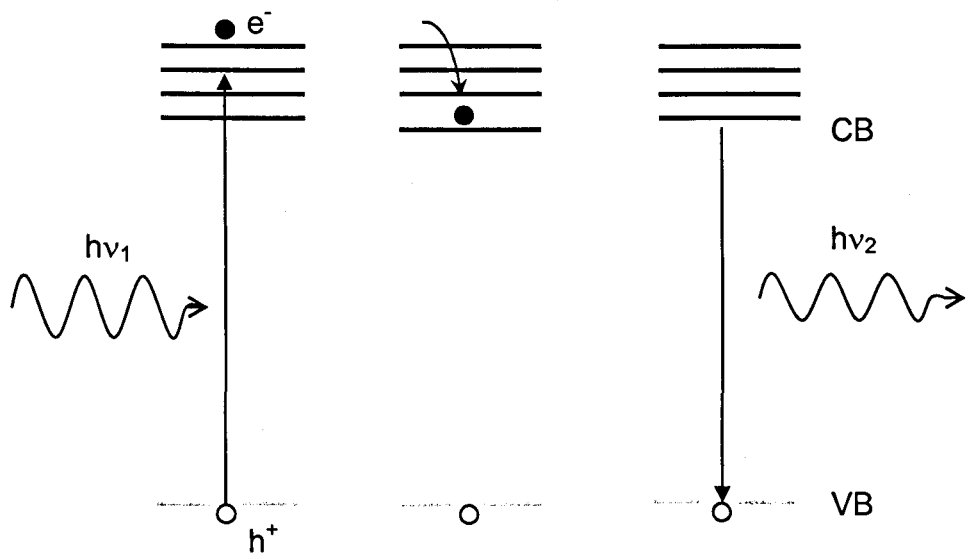

Figure 3.12: Schematic of electron excitation, decay in the conduction band (CB) and recombination with hole releasing a photon.

present in the crystal. These bound excitons emit at an energy lower than the bandgap and can be used to identify the defects present in a crystal. No studies of bound excitons were carried out in this thesis.

Epilayers are required to be relatively thick (several hundred nms) to produce enough excitons to provide a strong PL signal. Low dimensional structures, such as quantum wells (QW), do not have this restriction. An example of a QW structure is a thin (<10 nm) layer of a low band gap material encased in a high band gap barrier material. The excitons created in the barrier during PL excitation travel by drift or diffusion before being captured by the QW. These excitons drop in energy by thermalisation to the energy of the smaller band gap material, and are now trapped by the barriers. As a result of the increased number of excitons in the well, an increase in the intensity of the PL signal can be observed.

Members of the Nano-Optics Group at Heriot-Watt carried out the PL experiments presented in this thesis. The 350 nm line from an argon ion laser was used as the excitation source. Samples were placed in a cryostat at a temperature of 77K. Figure 3.13 shows a schematic of the equipment used.

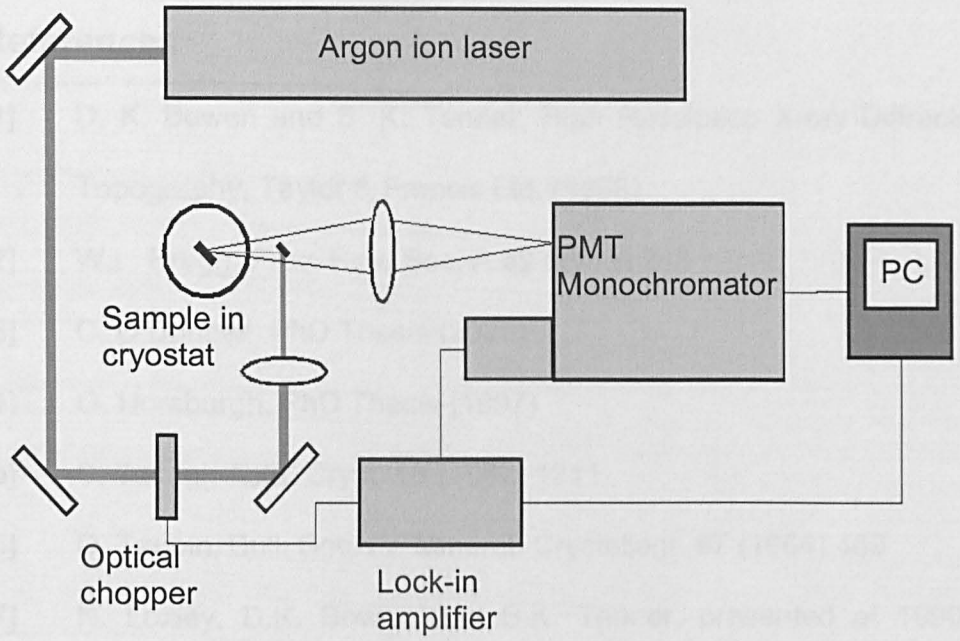

Figure 3.13: Schematic of Photoluminescence equipment used at Heriot-Watt.

References

[1] D. K. Bowen and B. K. Tanner, High Resolution X-ray Diffractometry and Topography, Taylor & Francis Ltd. (1998)

[2] W.L. Bragg, Proc. Roy. Soc. A **89** (1913) 248

[3] C. O'Donnell, PhD Thesis (2000)

[4] G. Horsburgh, PhD Thesis (1997)

[5] S. Takagi, Acta. Cryst. **15** (1962) 1311

[6] D. Taupin, Bull. Soc. Fr. Mineral. Crystallogr. **87** (1964) 469

[7] N. Loxley, D.K. Bowen and B.K. Tanner, presented at 1990 Fall MRS meeting, Channel Cut Collimator Reference and Instruction Manual

[8] A.T. Macrander and K.E. Strege, J. Appl. Phys. **59** (1985) 442

[9] W.J. Bartels and W. Nijman, J. Cryst. Growth **44** (1978) 518

[10] L. Tapfer, K. Ploog, Phys. Rev. B **40** (1989) 9802

[11] B. K. Tanner, J. Phys. D: Appl. Phys. **26** (1993) A151

[12] C. Bradford, C.B. O'Donnell, B. Urbaszek, A. Balocchi, C. Morhain, K.A. Prior and B.C. Cavenett, Appl. Phys. Lett. **76** (2000) 3929

[13] M.P. Seah and D. Briggs, Practical Surface Analysis, 2nd edition, Volume 1 – Auger and X-ray Photoelectron Spectroscopy, John Wiley and Sons (1990) 15

[14] D. Shirley, Phys. Rev. B **5** (1972) 4709

[15] Dimension™ 3100 Series Scanning Probe Microscope Instruction Manual, Digital Instruments (2000)

[16] Scanning Probe Microscopy Training Notebook, Version 3.0, Digital Instruments (2000)

Chapter 4: Growth and characterisation of MnS

4.1 Introduction

Naturally occurring materials usually adopt the lowest energy crystal structure available to them because it is the most stable form of the crystal. However, when a thin film of a particular crystal structure is deposited on a substrate of different crystal structure, it is not clear whether the film will adopt its lowest energy structure (stable) or the crystal structure of the substrate (metastable). Many examples exist where the growth occurs in a higher energy metastable crystal structure, for example the plasma chemical vapour epitaxy of diamond where, in fact, the lowest energy carbon structure is graphite. Other examples of compounds that can be grown in a metastable state are CdSe [1] and CdS [2] on (100) substrates where the four-fold periodicity of the underlying layer causes the deposited layer to adopt the metastable zinc blende (ZB) structure rather than the stable wurtzite crystal structure.

In this chapter, the novel growth method used to produce metastable ZB manganese sulphide (MnS) is described. Structural characterisation of the layers was carried out by X-ray interference (XRI) and X-ray diffraction (XRD) techniques. XRI analysis of thin layers was used to determine the growth rate of ZB MnS and the crystal quality of thicker layers was confirmed using XRD. Topography of the MnS surface, measured by AFM, will also be included in this chapter. The results obtained from the characterisation of the MnS layers will be compared to those

determined for ZB magnesium sulphide (MgS) layers, which were grown using the same novel growth technique.

4.2 MnS Overview

MnS is a wide band gap semiconductor with a band gap of 3.7eV. The stable crystal structure is rocksalt (NaCl), however there have been attempts to produce metastable ZB MnS.

Theoretical calculations [3] and experimental measurement [4] give a lattice constant for ZB MnS close to that of both GaAs and ZnSe, when grown in the ZB crystal structure. When compared to GaAs, MnS has a tensile strain of 0.7% and ZnSe has a compressive strain of –0.25%. Therefore, it is possible to grow multilayers of ZnSe/MnS as strain symmetrised structures.

Vacuum evaporation has been used to produce layer of MnS. Goede *et al* [5,6,7,8] produced polycrystalline layers up to a micron thick on glass or quartz substrates, by the evaporation of pure MnS powder. The layers were characterised using X-ray diffractometry and depending on the substrate temperature used during growth tetrahedrally co-ordinated MnS (T_{sub} ~ 50°C) or octahedrally co-ordinated MnS (T_{sub} ~ 200°C) was produced.

Previous attempts to grow ZB MnS by conventional MBE were carried out by Skromme *et al.* [4]. This technique used elemental Mn and a sulphur cracker as the

source of sulphur, and produced layers of only 50 nm thick before the crystal structure reverted to NaCl [4,9]. Cross sectional TEM of the layers showed that they were single crystal and selected area electron diffraction (SAED) indicated that they were pseudomorphic with no evidence of additional phases. Further analysis from low temperature photoluminescence of samples grown under a range of conditions showed emission from the internal transition of the Mn ion at 1.64 eV for MnS layers in the NaCl crystal structure, and when in the ZB crystal structure the Mn ion emitted at 2.13 eV.

Work on the growth of metastable sulphides at Heriot-Watt commenced in 1999 with the production of ZB MgS [10] by the novel growth method described in the next section. Previously, layers of MgS of less than a nanometre thick had been available when grown by conventional MBE. Using the Heriot-Watt method, layers of up to 134 nm were produced without any conversion from the metastable ZB to the stable NaCl crystal structure. Continuing from this success, work was begun on growing ZB MnS.

4.3 Growth of MnS

All ZnSe / MnS multilayer samples were grown using 6N Zn and Se elemental sources, a 6N ZnS compound source and a 5N8 elemental Mn source. The Mn source was further purified during the outgas process by repeated temperature cycling between 500°C and 800°C as described in section 2.4.

During the initial work on MnS, analysis of other samples grown without the use of the Mn cell indicated Mn contamination of those structures. Sample HWA1424, grown by X. Tang, with the structure shown in Figure 4.1 was analyzed using Secondary Ion Mass Spectrometry (SIMS) (discussed in section 4.4.2). Figure 4.1 also shows the raw SIMS data for sample HWA1424. The level of Mn in the sample is relatively uniform throughout the selenide layers, indicating that there was a problem of contamination, since only the quantum dot layer should have contained Mn. Examination of the Mn shutter during maintenance, showed a reflective material on the side facing the sample. This layer was believed to be Mn although it is not clear how it became transported to the front face of the shutter. The idle temperature of the Mn cell is 200°C; this temperature was sufficient to allow the Mn to effuse from the shutter into the sample grown. This problem was rectified by the use of a liquid nitrogen cooled shutter in front of the Mn cell, which restricted the cell aperture and ensured that no residual Mn flux escaped past the shutter, as well as preventing material build up on the front face of the shutter. Structures grown subsequently in the system have shown no Mn incorporation above the SIMS detection limit.

The samples were grown on GaAs (100) substrates. The 2 inch epi-ready wafers from Wafer Technology Ltd and American Crystal Technology (AXT) were quartered prior to growth, then etched in a 15:2:2 solution of H_2SO_4:H_2O_2:H_2O [11] for 90 seconds. The wafers were rinsed in 18MΩ deionised water and quickly dried with dry nitrogen gas.

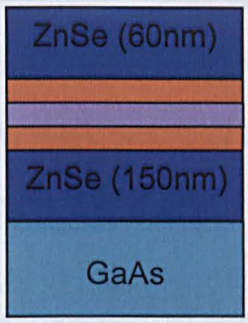

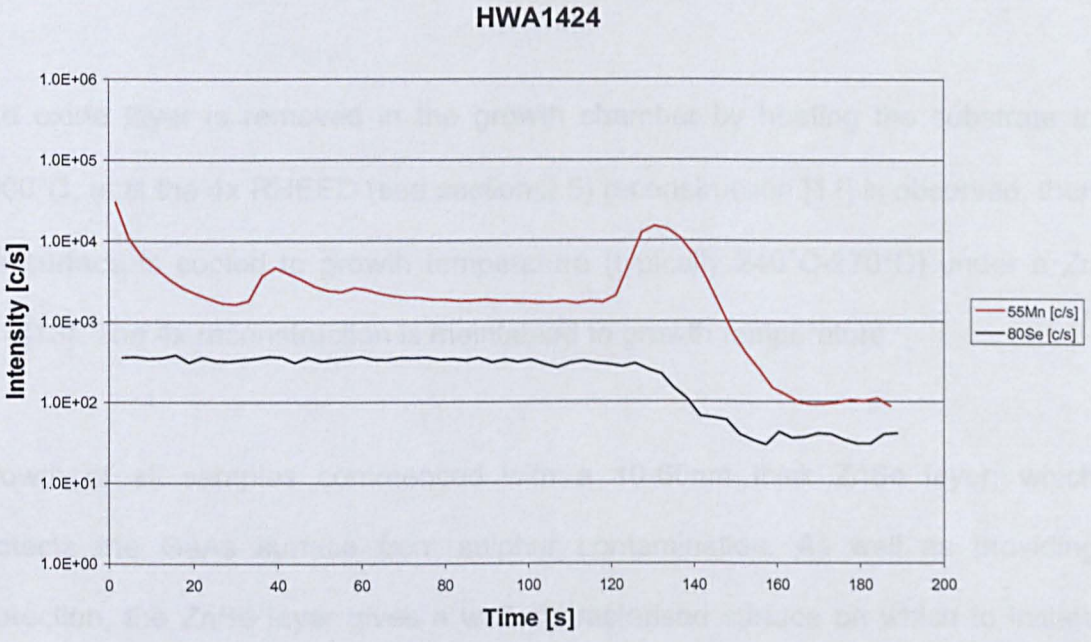

Figure 4.1: Raw SIMS data for sample HWA1424, a CdSe quantum dot sample with the structure shown.

Molten indium was used to bond the wafer to the molybdenum substrate holder used to transport the substrate in the vacuum system. Massies *et al.* [12] showed that the bonding process produces an oxide on the surface, which protects the surface until removed in the vacuum system. The layer is 2-3 nm thick dependant on the temperature used during bonding and the time taken to bond.

Once mounted the sample is introduced into the vacuum via the fast entry lock to the preparation chamber. The substrate holder is then heated to ~200°C for 10 minutes to remove water from the sample and substrate holder before transfer to growth chamber.

The oxide layer is removed in the growth chamber by heating the substrate to ~600°C, until the 4x RHEED (see section 2.5) reconstruction [11] is observed, then the surface is cooled to growth temperature (typically 240°C-270°C) under a Zn flux [13]. The 4x reconstruction is maintained to growth temperature.

Growth of all samples commenced with a 10-60nm thick ZnSe layer, which protects the GaAs surface from sulphur contamination. As well as providing protection, the ZnSe layer gives a well characterised surface on which to initiate the growth of MnS. RHEED showed that during the deposition of this buffer layer, the growth mode transforms from initially 3D growth to a flat surface, shown by the (2x1) RHEED pattern with long streaks typically observed from a ZnSe epitaxial layer.

After growing the ZnSe buffer layer, MnS was grown using the Mn and ZnS sources with cell temperatures of 780°C and 840°C, respectively. During the MnS growth, the surface morphology was monitored by RHEED. Initially, the MnS surface shows a (2x1) RHEED pattern, and any subsequent conversion from ZB to rocksalt can be clearly observed as a spotty RHEED pattern with visible off axis spots. An identical transition has been previously seen with MgS [14]. The RHEED patterns observed during the growth of MnS are discussed in detail in section 4.8.

4.4 X-ray characterisation

4.4.1 Growth rate measurement

Most thickness measurements and growth rate determinations are carried out by reflective or optical interference methods. The growth rate of ZnSe layers produced at Heriot-Watt is determined using reflectivity. The ZnSe epilayer acts as a Fabry-Perot etalon [15], the reflecting surfaces are the interfaces between the substrate and epilayer and the epilayer and air, due to the differences in the refractive indices of the materials. Light incident on the sample reflects from both the interfaces causing constructive and destructive interference. Epilayer thickness can be determined from the separation of the maxima and minima of the interference fringes, when plotted on a graph of intensity versus the wavelength of incident light. This method requires the thickness of the epilayer to be several hundred nanometres, as well as knowledge of the refractive index of the epilayer as a

function of wavelength. Layers of metastable ZB MnS could not be grown to the thicknesses required for this technique.

XRD can also be used to obtain structural quality information [16] and a measurement of the material thickness. The X-rays diffracted from the crystal have a constant phase relationship and the resulting interference produces Pendellösung fringes in the rocking curve. The periodicity of the fringes is inversely proportional to the thickness of the layer [16]. Unfortunately, the MnS layers grown were too thin to obtain such information directly.

Since MnS could not be grown to the thicknesses required for the use of these techniques, the method of X-ray interference (XRI) was used. As stated previously, this technique has been used successfully in the characterisation of MgS. A more detailed description of this method can be found in Chapter 3 and references [17,18,19].

Four samples of the structure ZnSe (X nm) / MnS / ZnSe (X nm) with varying thicknesses of the MnS layer were produced (where X nm is the intended thickness of ZnSe). RHEED observations indicated that the growth was in the zinc blende phase. The ZnSe layers were used in these structures because the lattice and elastic constants are well known, and the total ZnSe thickness is sufficient to provide well-defined X-ray peaks while still remaining below the critical thickness. The XRI analysis that follows was carried out by X. Tang as part of his doctoral work. It is presented here for completeness and to put further characterisation of MnS layers into context.

Figure 4.2 shows the 004 and 115 XRI experimental spectra and the corresponding simulations obtained from sample HWA1476, a structure GaAs / ZnSe (62nm) / MnS (4.3nm) / ZnSe (62nm). As mentioned previously, the computer simulation program requires the value of Poisson's ratio to be entered into the program. Since the value of Poisson's ratio for MnS is unknown, for initial simulations a value of 0.425 was used. This was the value previously obtained for MgS [10].

Although the fit was excellent, the simulation indicated that the MnS layers were 1-4% relaxed. The Pendellösung fringes should be faint or missing from the scan if such a relaxation had occurred, but many sharp fringes are present. Altering Poisson's ratio rectified this problem. It was found that increasing the value to 0.475 maintained the excellent fit to the experimental data, without any relaxation in the MnS layer. Further improvements to the fit were obtained by the inclusion of thin (0.5-0.6 nm) layers of $MnS_{0.45}Se_{0.55}$ between the ZnSe and MnS layers. The 004 and 115 experimental and simulated spectra of sample HWA1616, a 1.8 nm MnS layer, sandwiched between two 60 nm ZnSe layers with a 0.6 nm MnSSe layer and Poisson's ratio of 0.475, are shown in Figure 4.3. The significance of this value will be discussed in section 4.9.

The XRI simulations for the MnS layers were carried out using a ternary alloy of $Zn_{0.03}Mn_{0.97}S$, to account for the Zn incorporation determined by SIMS (see section 4.4.2). The other samples in this growth rate series were grown with increasing

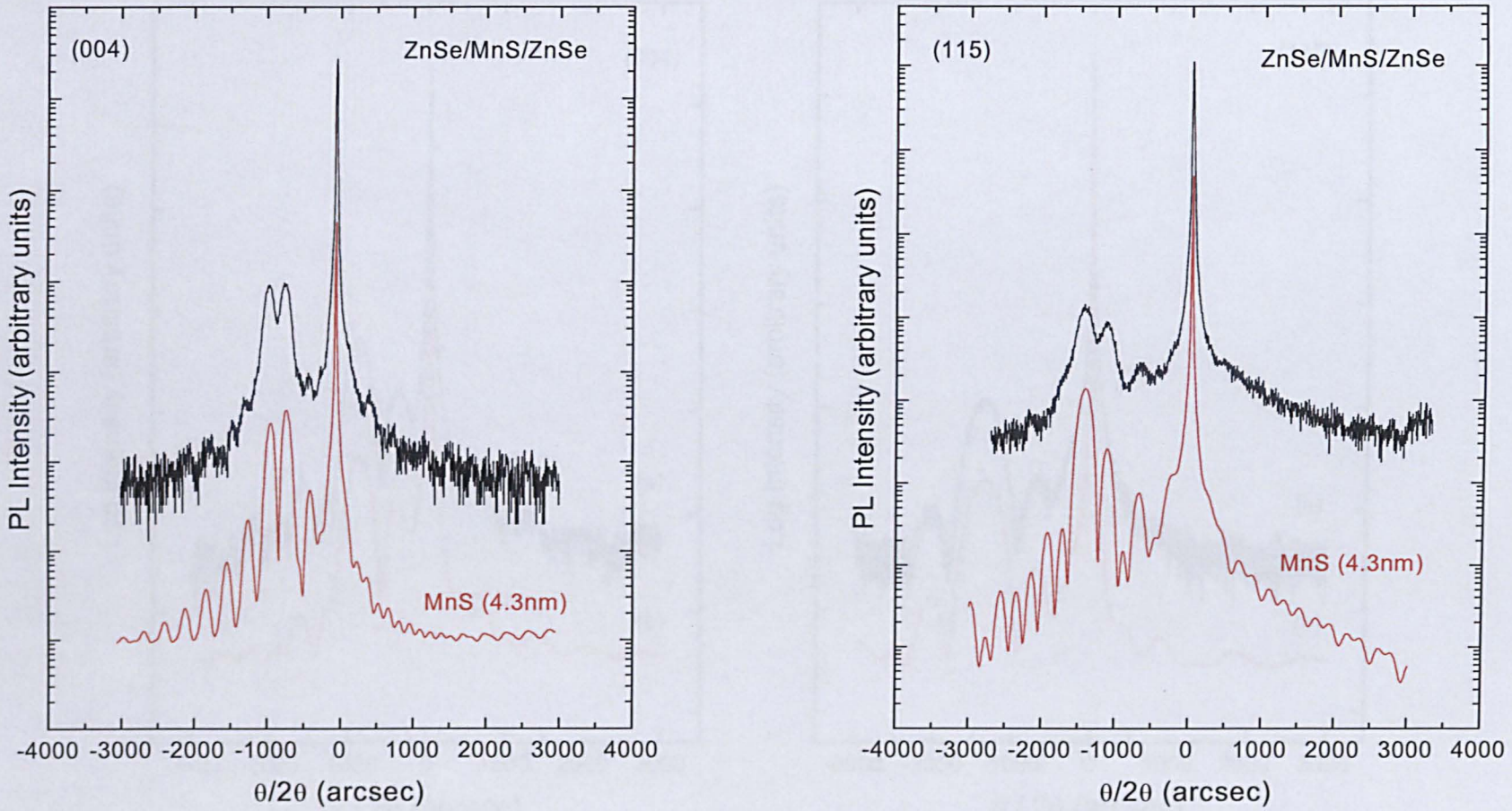

Figure 4.2: 004 and 115 XRI experimental spectra and corresponding simulations (in red) for HWA1476, with a structure GaAs (sub) / ZnSe (62 nm) / MnS (4.3 nm) / ZnSe (62 nm).

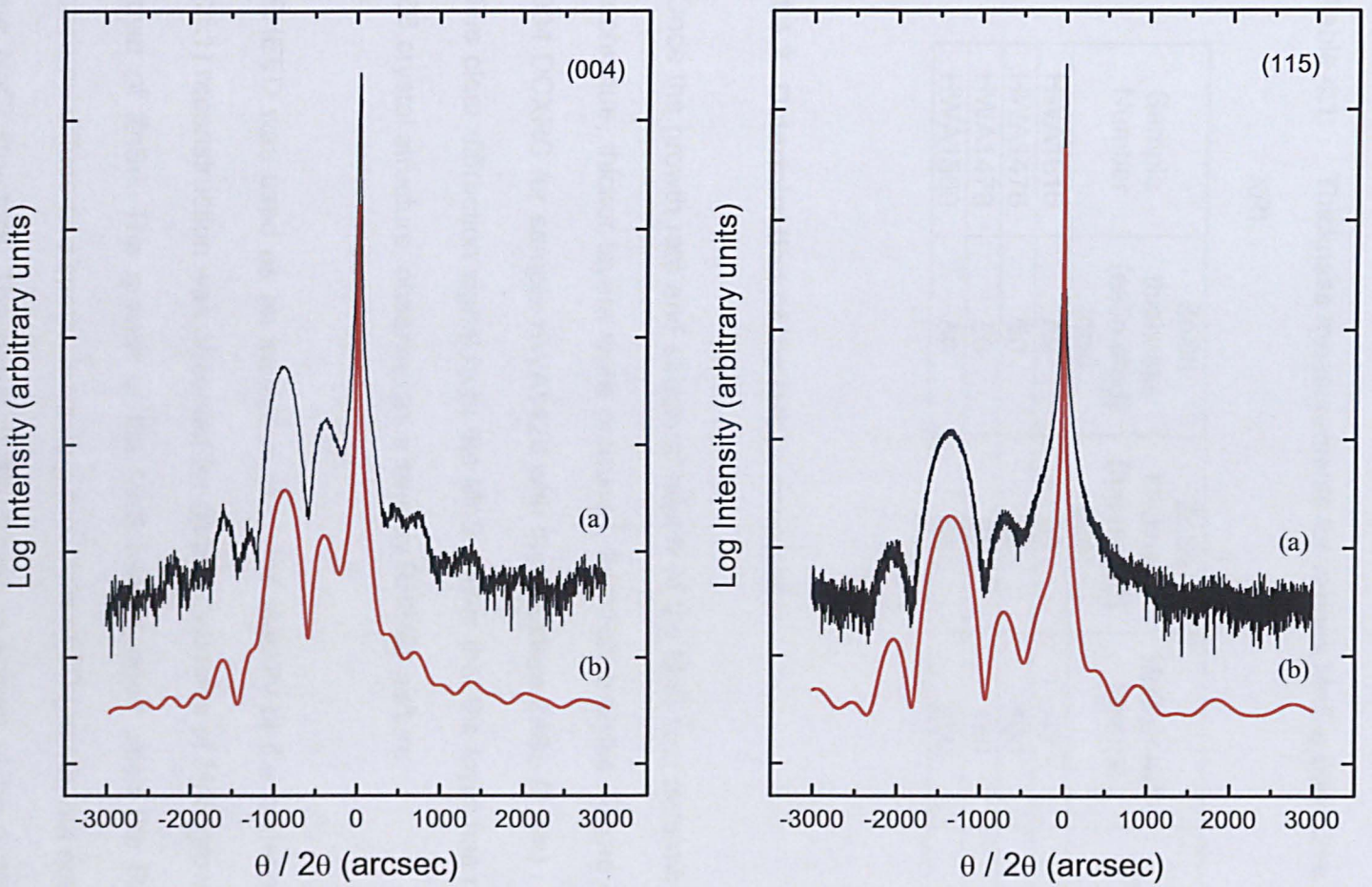

Figure 4.3: 004 and 115 XRI experimental spectra and corresponding simulations (in red) for HWA1616, with a structure GaAs (sub) / ZnSe (60 nm) / MnS (1.8 nm) / ZnSe (60 nm).

growth times for the MnS spacer layer, as shown in Table 4.1. From these samples, a growth rate of 0.15 μmh^{-1} was obtained which is similar to that of MgS.

Table 4.1: Thickness measurements for various MnS growth time determined by XRI.

Sample Number	ZnSe thickness (estimated) (nm)	ZnSe thickness (measured) (nm)	MnS growth time (s)	MnS thickness (nm)
HWA1616	50	60	47	1.8
HWA1476	50	62	100	4.3
HWA1478	50	65	150	6.5
HWA1500	50	61	200	8.6

4.4.2 Determination of the lattice constant

Once the growth rate and structural quality of the MnS was determined by the XRI technique, thicker layers were produced, for XRD analysis. Figure 4.4 shows the 004 DCXRC for sample HWA1423 with the structure ZnSe (5 nm) / MnS (17 nm). The clear diffraction signal from the MnS shows that the layer has maintained the ZB crystal structure, observed as a streaky RHEED pattern.

RHEED was used as an indication of phase stability of the material. The streaky (2x1) reconstruction was observed for up to 27 minutes of MnS growth on a 10 nm layer of ZnSe. The growth of the MnS was stopped when the RHEED pattern became diffuse and spotty, indicating the onset of 3D growth, but not conversion to the NaCl structure. The onset of 3D growth is known to be a precursor to the crystal structure conversion from previous growths of both MgS [20] and MnS.

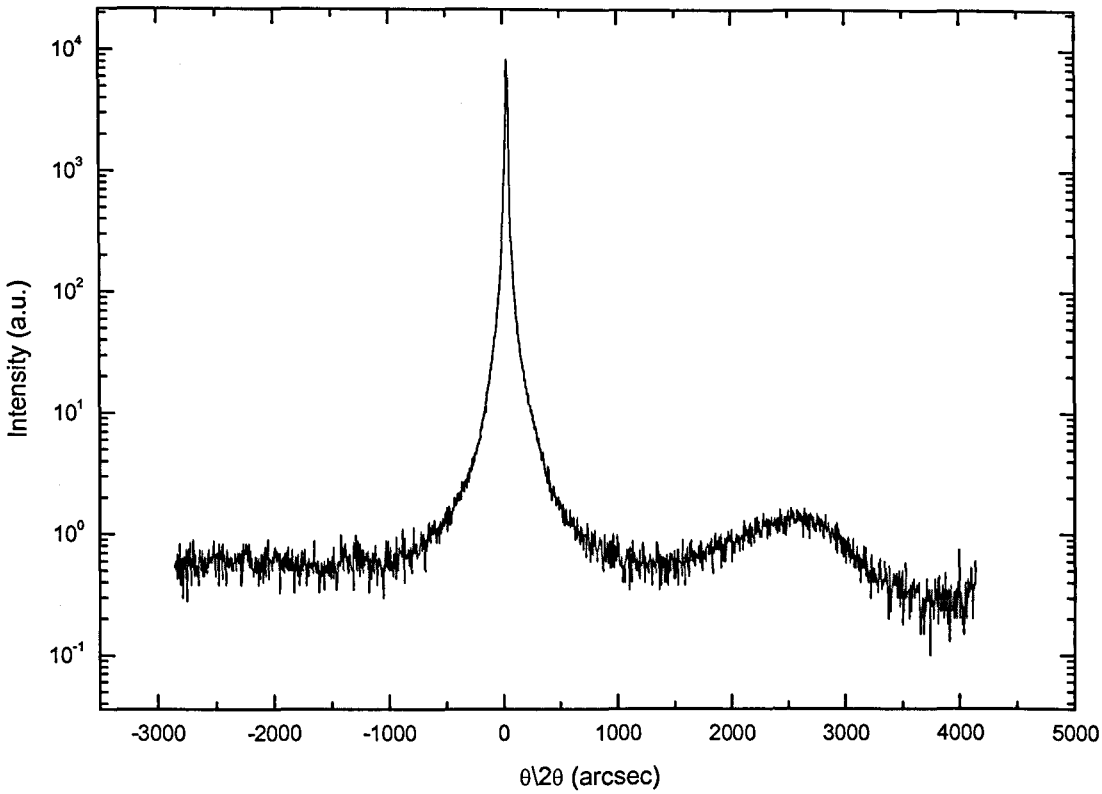

Figure 4.4: 004 XRD scan of HWA1423, a 17 nm layer of MnS.

Using the growth rate determined in the previous section, 27 minutes of growth (sample HWA1432) is calculated to be a 68 nm MnS layer.

Since a compound ZnS source was used as the sulphur source in the growth of MnS layers, it was expected that there would be some residual Zn incorporation in the samples. Sample HWA1432 was sent to Loughbrough Surface Analysis (LSA) for SIMS and Auger depth profiling.

The MnS layer was capped with a thin layer of ZnSe which was removed by Secondary Ion Mass Spectrometry (SIMS). This is a destructive technique where a high energy (1-30 keV) beam of ions (Cs^+ or O^+) is incident on the sample. The bombardment of the sample results in the ejection or sputtering of atoms from the material. A small percentage of these ejected atoms leave as either positively or negatively charged ions, referred to as secondary ions. These secondary ions are collected and analysed by mass to charge spectrometry to give information on the composition of the sample.

The SIMS results, shown in Figure 4.5, show sharp interfaces between the ZnSe and MnS layers with a residual Zn signal detected in the MnS layer. Simultaneous Auger spectroscopy was used to determine the residual Zn incorporation in the MnS layers, which was estimated to be approximately 3%. This result is comparable to the 0.5-2% residual zinc content found in MgS grown by the same method [10].

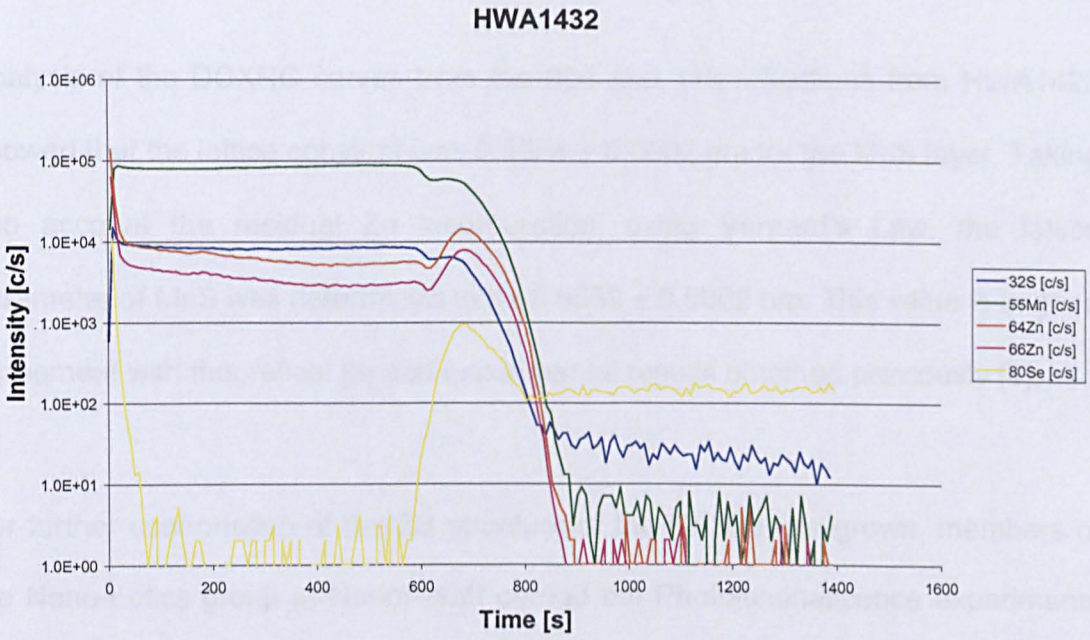

Figure 4.5: SIMS results from HWA1432, a 68 nm layer of MnS.

Analysis of the DCXRC curves from the 004 and 115 reflections from HWA1423 showed that the lattice constant was 0.5554 ± 0.0002 nm for the MnS layer. Taking into account the residual Zn incorporation, using Vergard's Law, the lattice parameter of MnS was determined to be 0.5559 ± 0.0002 nm. This value is in good agreement with theoretical [3] and experimental results obtained previously [4].

For further confirmation of the ZB structure of the MnS layers grown, members of the Nano-optics group at Heriot-Watt carried out Photoluminescence experiments on thick MnS layers. Figure 4.6 shows a weak emission peak at 2.13 eV from sample HWA1432, a 68 nm layer of MnS. This emission has been assigned to tetrahedrally co-ordinated Mn atoms [4] in the layer. Octahedrally co-ordinated Mn atoms emit at 1.67 eV, this emission was never observed (not shown in figure).

4.5 Increase of the maximum thickness by using a smoothing layer

Previous work with MgS showed that using a ZnSe / MgS multilayer in place of the ZnSe buffer layer could increase the maximum thickness of the ZB material from 67 nm to 134 nm.

Sample HWA1528 was grown replacing the ZnSe buffer layer with a ZnSe / MnS multilayer, again monitoring the phase stability with RHEED. Growth of the upper MnS layer was stopped when the RHEED pattern became diffuse and spotty, however the spots were not off axis, indicating that the layer remained in the ZB

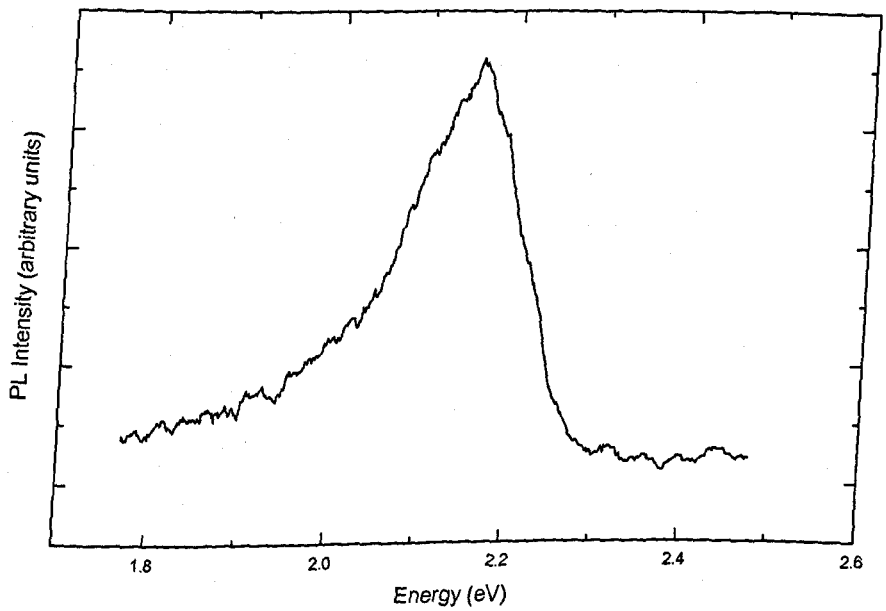

Figure 4.6: PL spectrum from a 68 nm MnS layer (HWA1432) showing emission from tetrahedrally coordinated Mn atoms.

structure. Figure 4.7 shows the 004 DCXRC for this sample with the structure ZnSe (53 nm) / MnS (23 nm) / ZnSe (18 nm) / MnS (132 nm). The MnS signal is intense and asymmetric, comparison with simulations show that the layer is ~ 90 % relaxed. The ZnSe signal to the left of the GaAs substrate peak, is due to the amount of ZnSe present in the ZnSe / MnS multilayer.

4.6 Comparison of MnS and MgS

As previously stated, ZB MnS and MgS are grown using the same novel method developed at Heriot-Watt. Ultra pure (6N) magnesium is used with the ZnS compound source to produce ZB MgS. The results from the X-ray characterisation, SIMS and critical thickness experiments show similarities between the values determined for MnS and those found previously for MgS. Table 4.2 shows a summary of the results for both MnS and MgS.

Table 4.2: Comparison of growth and structural properties of MgS and MnS.

	MgS	MnS
Lattice Constant (nm)	0.5622±0.0002	0.5559±0.0002
Strain to GaAs	5.6×10^{-3}	1.7×10^{-2}
Poisson's Ratio	0.425	0.475
Residual Zinc Content (%)	0.5-2	3
Growth Rate ($\mu m\ h^{-1}$)	0.15	0.15
Maximum Thickness		
on ZnSe buffer (nm)	67	68
on ZnSe multiplayer (nm)	134	132

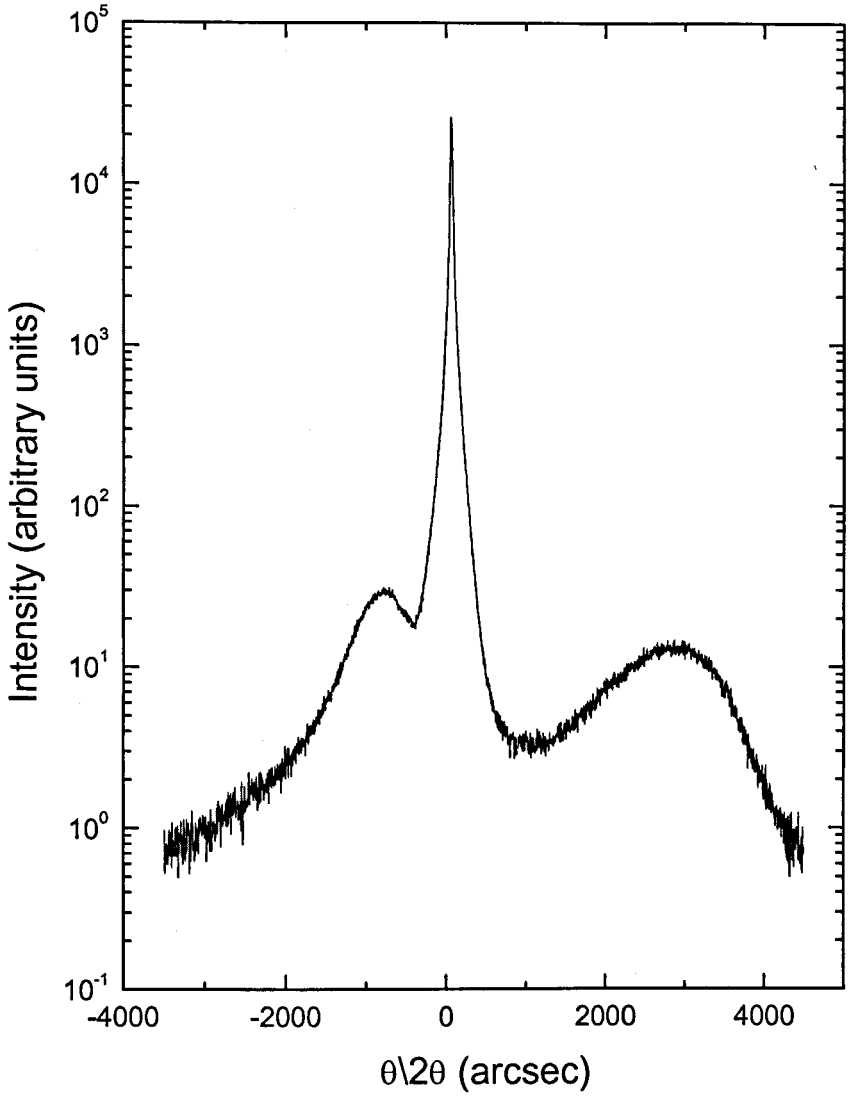

Figure 4.7: 004 XRD scan for HWA1528, a 132 nm layer of MnS grown in a ZnSe / MnS multilayer buffer.

The metastable ZB crystal structure of MgS and MnS is easily lost. This can be observed during growth by RHEED, and after growth using DCXRC and AFM analysis. It was not possible to record RHEED images during the work on MnS layers, due to the condition of the RHEED gun in the MBE system. Attempts were made to improve the RHEED intensity so that the images could be captured, including refocusing of the beam and replacing the fluorescent screen on a regular basis. However, the RHEED patterns observed during the growth of MnS were consistent with those recorded for layers of MgS [20], which, for the purposes of illustration, are given below.

Figure 4.8 shows the RHEED patterns from a series of MgS layers. The thinnest layer in the series was a 10 nm layer (Figure 4.8a). The RHEED pattern shows long streaks indicating 2D growth. This is the same pattern that was found during the growth of thin MnS layers. Figure 4.9 shows a 5 μm^2 AFM surface scan of sample HWA1838, a 5 nm thick layer of MnS. The surface is rougher than that of a similar thickness of MgS, with a mean roughness value of 1.708 nm. For comparison, the mean roughness value for a layer of MgS grown under similar conditions is 0.435 nm [14].

Thicker layers, up to 60 nm, maintain this streaky pattern except in the $[1\bar{1}0]$ azimuth, which becomes spotty as shown in Figure 4.8b. The spotty RHEED pattern indicates the onset of 3D growth, at this point the layer is still growing in the ZB crystal structure. The spotty RHEED pattern is evident in the AFM scans as a

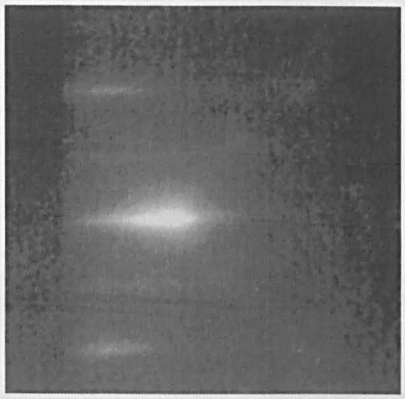

a) After 10nm growth
Atomically flat surface

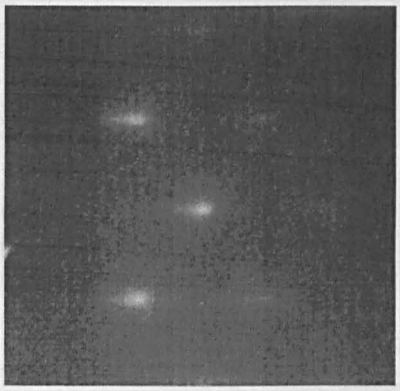

b) After 20nm+ growth
1D ridges on surface

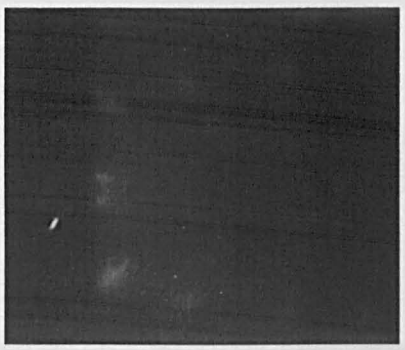

c) After 200nm growth
Phase change to rocksalt

Figure 4.8: RHEED pictures taken during different stages of MgS growth.

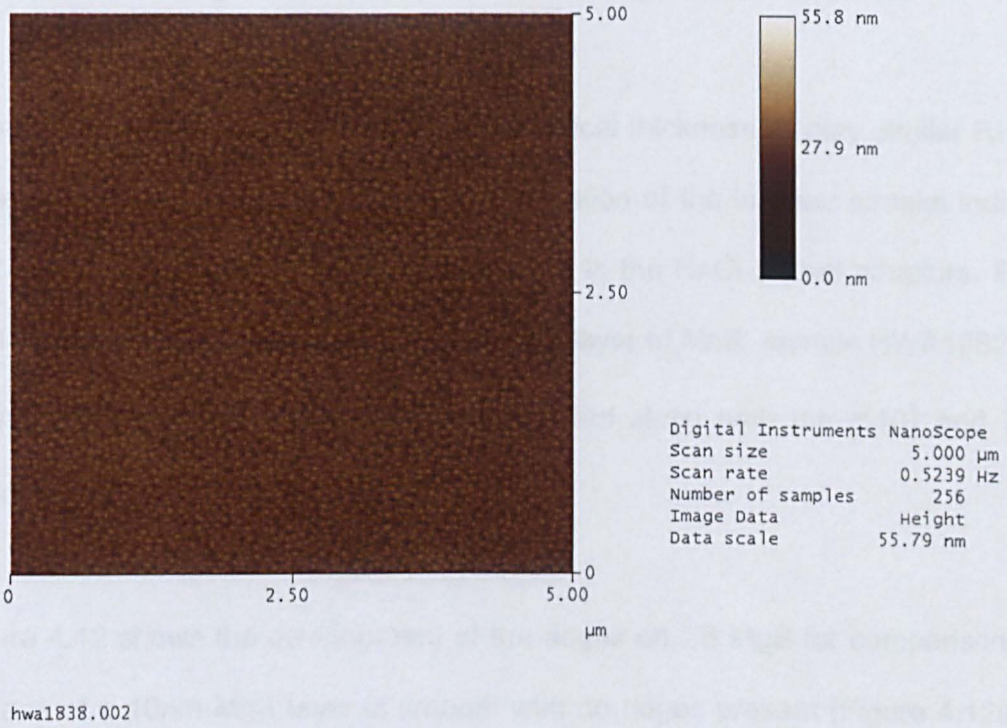

Figure 4.9: 5 µm^2 AFM scan of HWA1838, a 5 nm layer MnS.

series of ridges in the [110] direction. Figure 4.10 is a 5 μm^2 scan of sample HWA1841, a 28 nm layer of MnS. The 3 nm high ridges are parallel to the [110] direction. The background surface has a mean roughness of 0.478 nm.

Layers that have been grown beyond the critical thickness display similar RHEED patterns to those in Figure 4.8c. The observation of the inclined streaks indicates that the structure has converted from the ZB to the NaCl crystal structure. Figure 4.11 shows a 20 μm^2 AFM scan of a 200 nm layer of MnS, sample HWA1852. The scan shows both ridges and cracks, orientated along both the [110] and $[1\bar{1}0]$ directions.

Figure 4.12 shows the development of the ridges on ZB MgS for comparison. The surface of a 10nm MgS layer is smooth with no ridges present (Figure 4.12a). As the thickness of the MgS layer is increased to 20nm, AFM scans of the surface show periodic ridges orientated in the [110] direction (Figure 4.12b). Layers of MgS grown beyond the critical thickness (Figure 4.12c) have developed cracks on the surface in the [110] and $[1\bar{1}0]$ directions. The cracks have propagated from the surface through the ZB MgS layer to the underlying ZnSe buffer layer.

While both surfaces of the MnS and MgS layers develop ridges, the ridges on MnS are less uniform than those on MgS. Once the materials have converted to the NaCl crystal structure, the difference in the AFM scans is more defined. While the MgS cracks propagate down to the ZnSe layer, the MnS features remain in the upper section of the MnS layer.

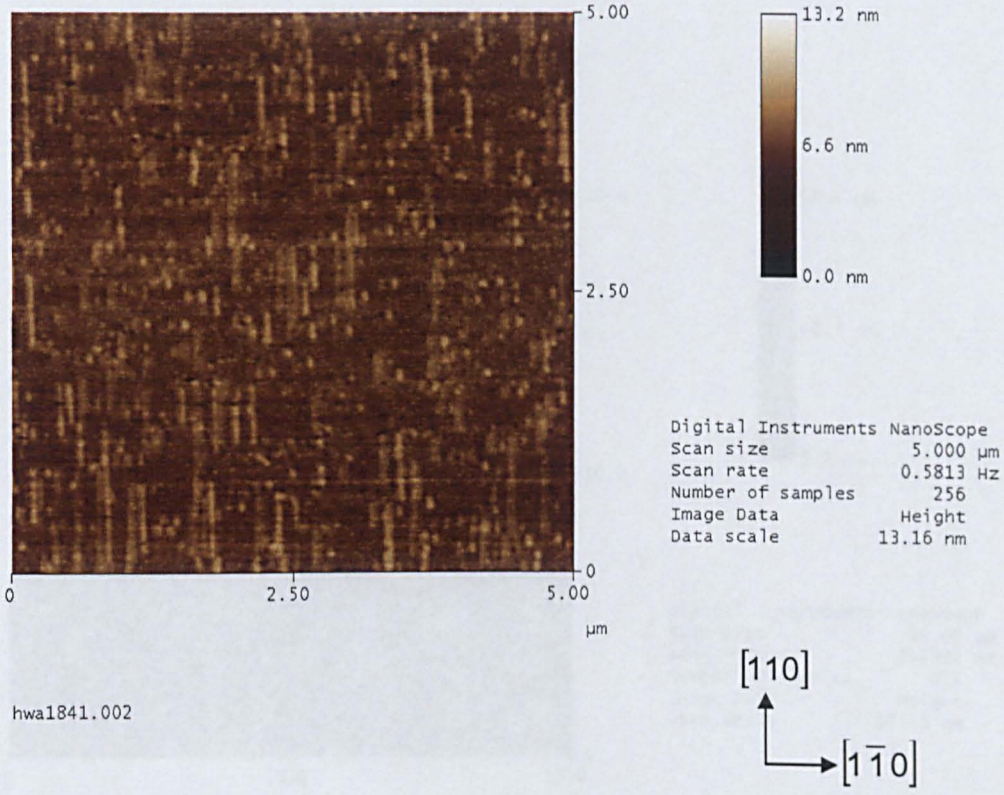

Figure 4.10: 5 µm^2 AFM scan of HWA1841, a 28 nm layer MnS.

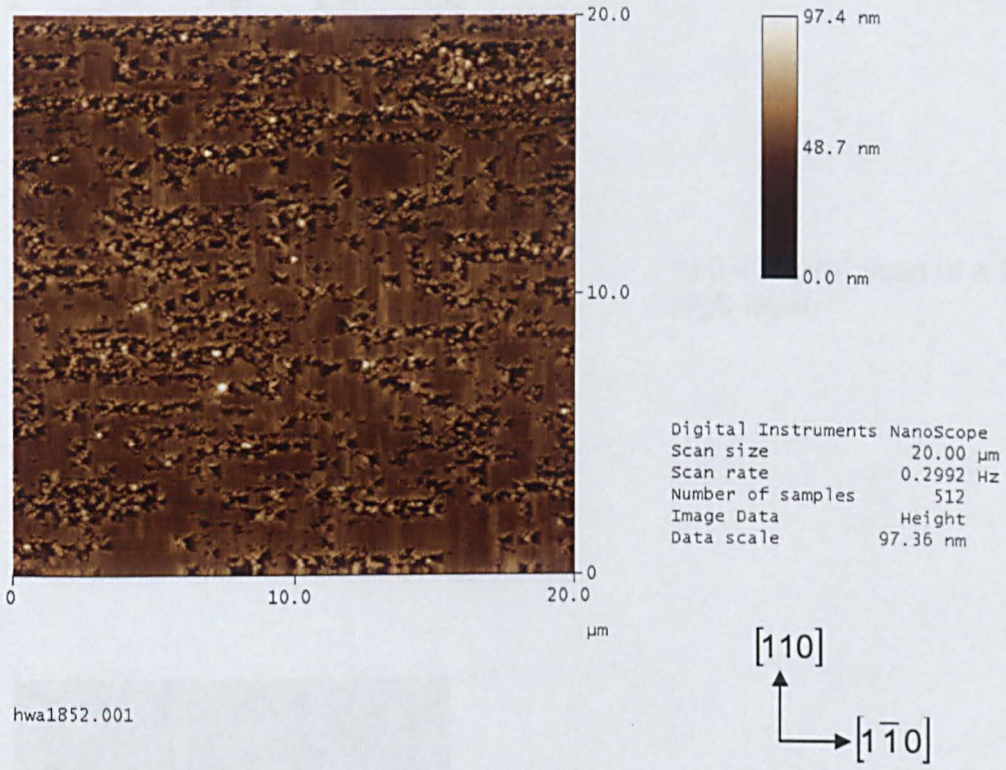

Figure 4.11: 20 µm^2 AFM scan of HWA1852, a 200 nm layer MnS.

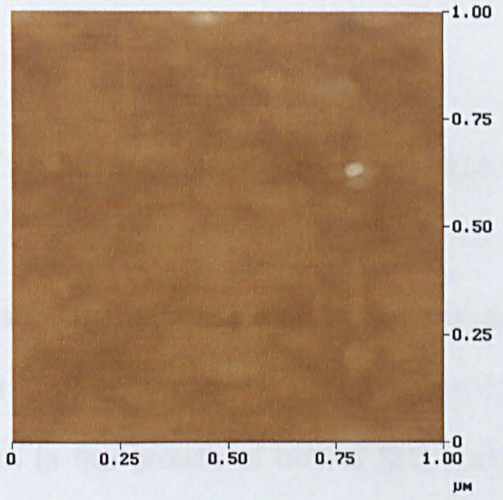

a) 1 μm^2 scan of a 10 nm MgS layer

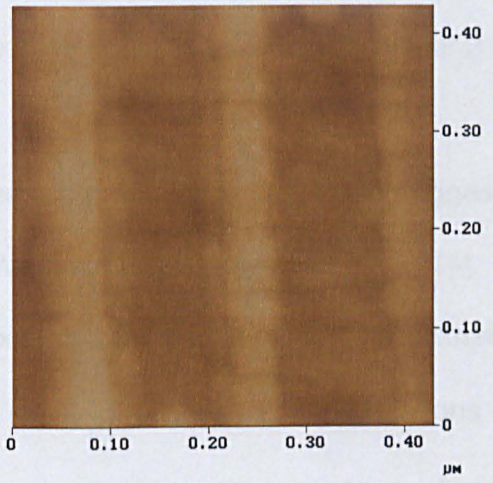

b) 0.425 μm^2 scan of a 20 nm MgS layer

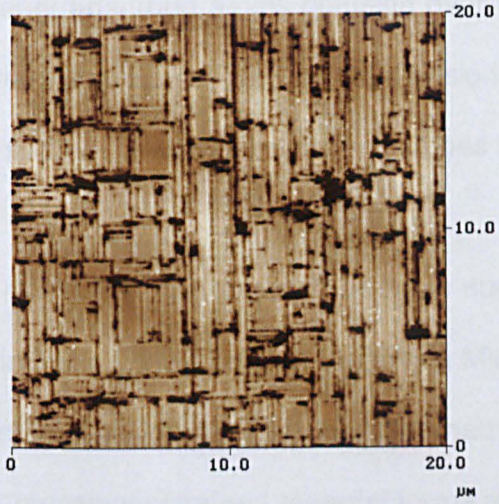

c) 20 μm^2 scan of a 200 nm MgS layer

Figure 4.12: AFM images of MgS layers of various thicknesses.

4.7 Surface stability and ridge formation

As shown in the previous section, the surface morphology of both metastable MnS and MgS layers evolve into a series of parallel ridges. Similar ridges have been seen in the growth of InAlAs [21] and InGaAs [22] on InP. The tensile strain in these alloys is found to cause significant anisotropy within the layers, with relaxation occurring preferentially along the $[110]$ direction rather than $[1\bar{1}0]$.

Anisotropic relaxation has been suggested as being responsible for the formation of the ridges in metastable MgS [14]. The suggested mechanism of anisotropic relaxation creates a network of mismatched dislocations orientated along one of the $\langle 110 \rangle$ directions. The dislocations could act as a template for the confined nucleation of nanostructures from adatoms, since mismatch dislocations are known to repel adsorbed atoms diffusing over a surface [23]. The network of dislocations increases the anisotropy of the diffusion coefficient for material on the surface thus the surface is more likely to form ridges than a flat uniform surface.

An alternative explanation has been suggested for the formation of surface ridges on InGaAs [22]. Scanning Tunneling Microscope (STM) images were taken of both compressively and tensilely strained InGaAs layers on InP. Deposition of compressively strained material forms isolated flat platelets which are longer in the $[1\bar{1}0]$ direction than $[110]$. As the amount of material deposited increases, the platelets are elongated to ridges in the $[1\bar{1}0]$ direction while maintaining the same

width. The height of the ridges also increases with the amount of material deposited, with a ridge height of 15-20 ML where 10 ML of material had been deposited. This is compatible with a model involving stress driven mass transport of material from the regions between the ridges.

The evolution of the morphology appears to be different for the tensile case. A great number of smaller platelets as well as narrow holes with a high aspect ratio are formed when tensilely strained material is deposited on the surface. These holes deepen as the amount of material deposited is increased, and are elongated along the $[1\bar{1}0]$ direction. As more material is deposited the material around these holes form ridges across the surface along the $[1\bar{1}0]$ direction. The spontaneous generation of surface undulations with a preferred periodicity under stress is known as the Asaro–Tiller–Grinfeld instability [24,25].

Both the anisotropic relaxation and Asaro–Tiller–Grinfeld instability mechanisms predict that the ridges form on the surface if the epitaxial layer has relaxed anisotropically, but the ridges form in orthogonal directions. In the case suggested for MgS [14], the ridges will be parallel to the strained direction, while the Asaro–Tiller–Grinfeld instability predicts that they will be orthogonal. Triple crystal X-ray reciprocal space mapping measurements on partially relaxed layers are required to distinguish between the two mechanisms.

4.8 Conversion from zinc blende to rocksalt crystal structure

The transformation of crystals from the ZB to NaCl structure has been studied experimentally under high pressure [26] and theoretically [27,28,29] for many III-V and II-VI semiconductors. The co-ordination number for all atoms changes from four to six during the transformation process. The transformation is diffusionless and is a martensitic transition [30].

There are different diffusionless mechanisms possible for the transformation from ZB to NaCl. Sowa [27] has shown that all these possible transformations must occur via a lower symmetry intermediate structure with a space group that is a subset of the space groups of both ZB and NaCl. The following shows a transformation mechanism similar to that determined for ZnS [29], proceeding via an orthorhombic intermediate, therefore fulfilling the criteria of Sowa. This transformation is not necessarily the one adopted by MgS and MnS but the pathway seems to depend on the ionicity of the compound and ZnS (0.623) [31] is the best match for MgS (0.786) [31] and MnS (0.784) [32].

Figure 4.13 shows a unit cell of ZB ZnS, zinc atoms are in blue and sulphur atoms are in yellow. The nearest neighbour bonds are red and are 2.42 Å long. In order to make the transition clearer, the set of axes are changed so that the *a* and *b* axes are along the ZB $[110]$ and $[1\bar{1}0]$ directions. The new unit cell, a tetragonal-I cell, is shown in Figure 4.14, the red bonds indicate the four fold co-ordination.

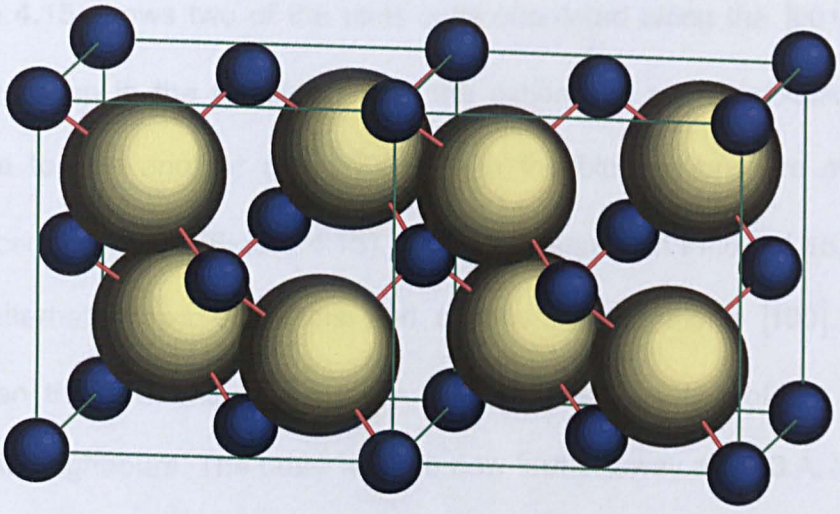

Figure 4.13: Two adjoining unit cells of ZnS, zinc atoms are blue and sulphur atoms are yellow.

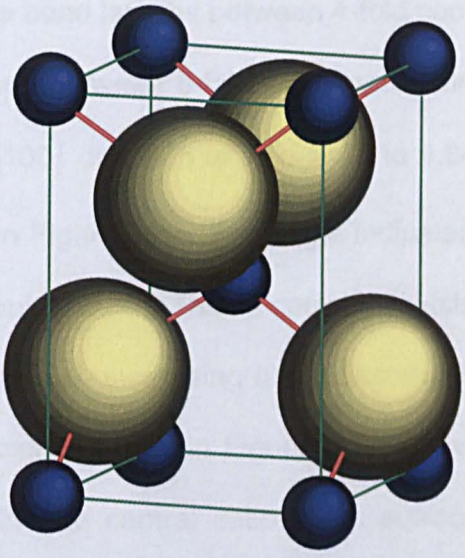

Figure 4.14: New unit cell of ZnS with a change of axes.

Figure 4.15 shows two of the units cells orientated along the [001] direction. For this first step in the transformation, the cation and anion sublattices are moved relative to one another along [001], with the blue cations are moved up by a displacement of c/4 (Figure 4.15). It can be seen from Figure 4.16, that there are now alternate rows of anions and cations spaced along [100]. The distance between these atoms is now only 1.98 Å; these are two of the cations former nearest neighbours. The other two are now further away at 3.43 Å. However, there are now another two atoms also at the same distance, indicated by the blue bonds in Figure 4.16. These four anions lie on the same (011) plane. At this point there is 2+4 co-ordination and the next step is to get the bonds the same length.

Assuming that the bonds should be the same length as in the ZB structure simplifies the calculation, although it is unlikely that the bonds will end up exactly the same length. The bond lengths between 4-fold coordinated atoms are generally 5% smaller than those between 6-fold coordinated atoms [33,34]. First, the lattice constant along the [100] direction is increased to 4.84 Å, producing a more open structure as shown in Figure 4.17. The angle indicated is only 70°, whereas in the NaCl structure it should be 90°. This is corrected while simultaneously making the bonds the correct length by increasing *b* and decreasing *c* as shown in Figure 4.17. The new NaCl unit cell is shown in Figure 4.18, the values for the NaCl structure are $b = c = a_{new}/\sqrt{2}$. The central cations are surrounded by anions at identical distances. The axes of the NaCl crystal lie along the close packed directions of the new crystal; [100], [011] and $[0\bar{1}1]$.

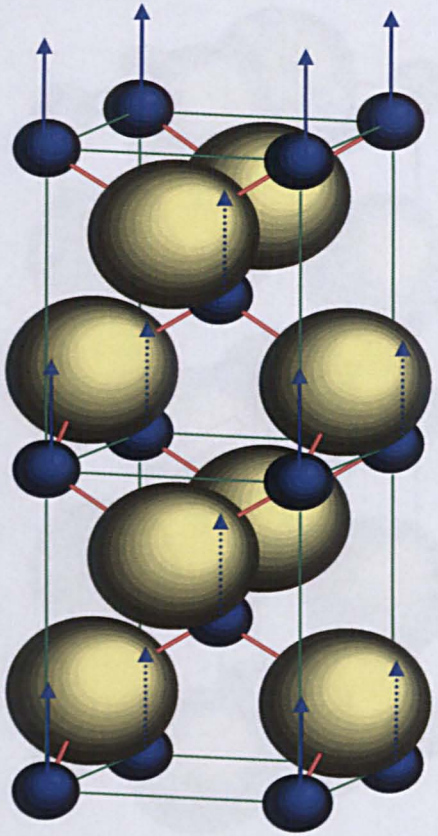

Figure 4.15: Two unit cells of ZnS showing the cations moving up by c/4

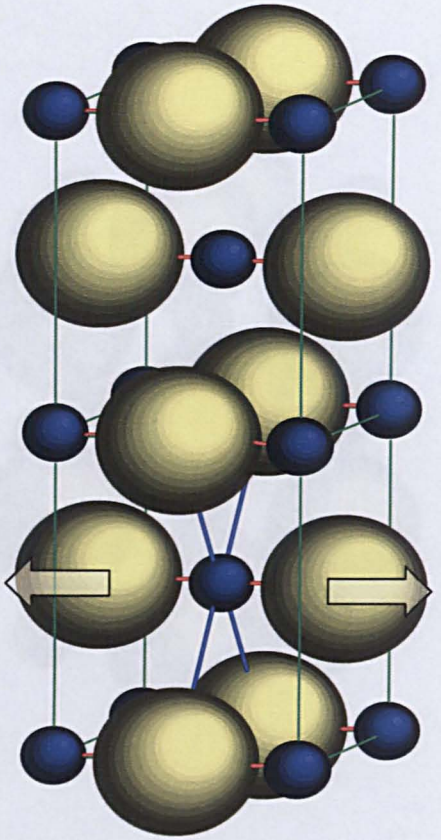

Figure 4.16: Alternate rows of cations and anions.

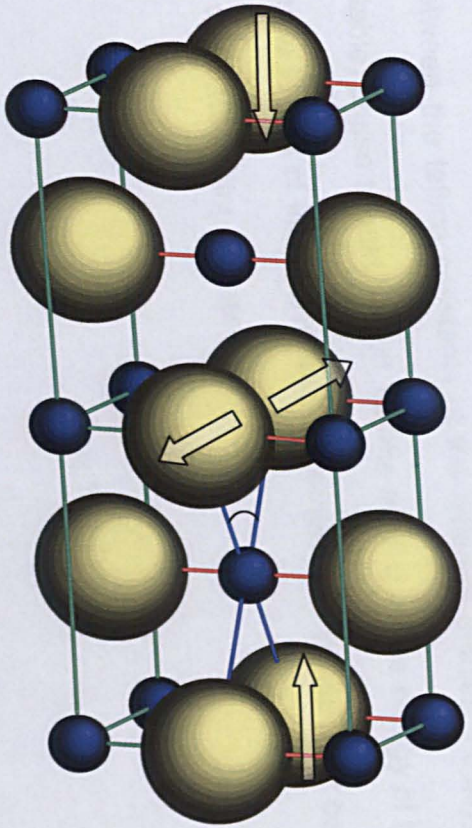

Figure 4.17: The open structure showing the compression along the c axis and lengthening along the b axis.

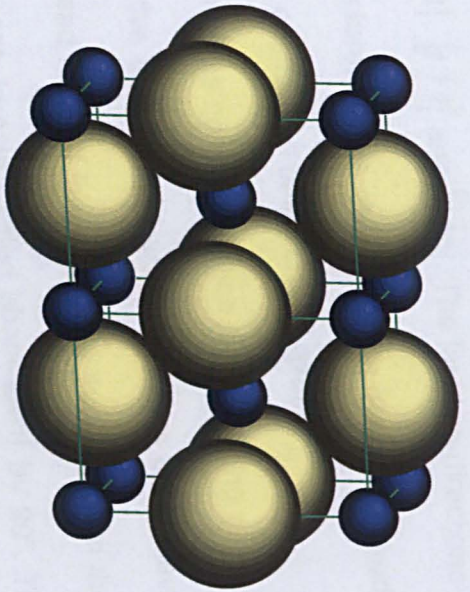

Figure 4.18: The final NaCl structure after the transformation.

There are two points to note with this transformation:

1. The direction of the NaCl axes compared to the original ZB axes are along $[110]$, $[1\bar{1}1]$ and $[\bar{1}11]$. The last two directions are not orthogonal in the ZB structure. This is caused by the distortion introduced during the lengthening and contraction of the crystal axes.
2. There was no single option in the shifting of the anion and cation sublattices relative to one another. The cations could have been moved down by c/4 instead of up. If that had been the case then the NaCl crystal would have a different domain rotated about $[001]$ by 90°. The axes of the NaCl crystal would then be along $[1\bar{1}0]$, $[111]$ and $[\bar{1}\bar{1}1]$.

Froyen *et al.* [35] have determined three requirements for systems in order to predict if they would exhibit epitaxial phase transitions. The first is that the difference between the minimum structural energies of the two competing phases should be small. A second requirement is that there should be a large difference between the lattice constants of the different phases. Finally, the lowest energy (stable) phase should be stiff, i.e. the ratio, *q*, of the energy of the relaxed epitaxial phase to that of the hydrostatically compressed phase must be large. The *q* value is calculated using equation 4.1 [35]:

$$q_{[100]} = \frac{2}{3}\left[1 - \frac{c_{12}}{c_{11}}\right] \qquad \text{Equation 4.1}$$

Where c_{11} and c_{12} are the elastic constants of the stable phase of the material and the subscript of q indicates the growth direction.

There are no calculations at present for the elastic constants of NaCl MnS, however the elastic constants of MgS are detailed in Table 4.3 below.

Table 4.3: Elastic constants for ZB and NaCl MgS.

MgS elastic constants (GPa)	ZB [36]	NaCl [37]
C_{11}	74.00	183.45
C_{12}	54.7	34.92

Therefore $q_{[100]}$ for the stable NaCl phase of MgS is:

$$q_{[100]} = \frac{2}{3}\left[1 - \frac{34.92}{183.45}\right]$$

$$= 0.5398$$

This value is large as the maximum value for q is 0.666 [35], so the third requirement is fulfilled for MgS. The second requirement, that the difference in lattice parameter of the two phases must be large is satisfied for MgS as the lattice parameter for ZB MgS is 5.619 Å [10] and 5.203 Å [37] for NaCl MgS. This requirement is also satisfied for MnS as the lattice parameter for ZB MnS is 5.559 Å and for NaCl MnS the lattice parameter is 5.224 Å [3].

The first requirement, that the difference between the minimum energies of the two different phases should be small, is fulfilled for MgS since it has been shown by

Navrotsky and Phillips [38] that the free energy for the transformation between the ZB and NaCl phases of MgS is close to zero (Figure 4.19). Navrotsky and Phillips also suggested that the position of MnS on Figure 4.19 would lie between MgS, MgSe and CdO, therefore satisfying the criteria for the MnS transition as well.

4.9 Poisson's Ratio

The value of Poisson's ratio for ZB MnS, 0.475, determined from XRI in section 4.4.1, is rather high, and indicates that the compressibility of the layers is also very low. This is unusual since the layers are metastable and beyond a critical thickness (132 nm) the crystal structure reverts back to its stable NaCl structure, so a high compressibility (low Bulk modulus) would be expected. From the value of Poisson's ratio, we can calculate the difference in the elastic constants c_{11} and c_{12} in terms of c_{11}, as in Equation 4.2.

$$c_{11} - c_{12} = c_{11}\frac{(1-2\nu)}{(1-\nu)} \qquad \text{Equation 4.2}$$

Structurally, the value of $(c_{11} - c_{12})$ is a measure of the resistance of the crystal to shear along the $[0\bar{1}1]$ on (110) plane [30]. In the present case, $(c_{11} - c_{12}) = 0.095c_{11}$, and the structure is easily sheared in this direction. The same quantity is also used to calculate the bond bending force constant, C_1 [39],

$$C_1 = \frac{a^3}{32}(c_{11} - c_{12}) \qquad \text{Equation 4.3}$$

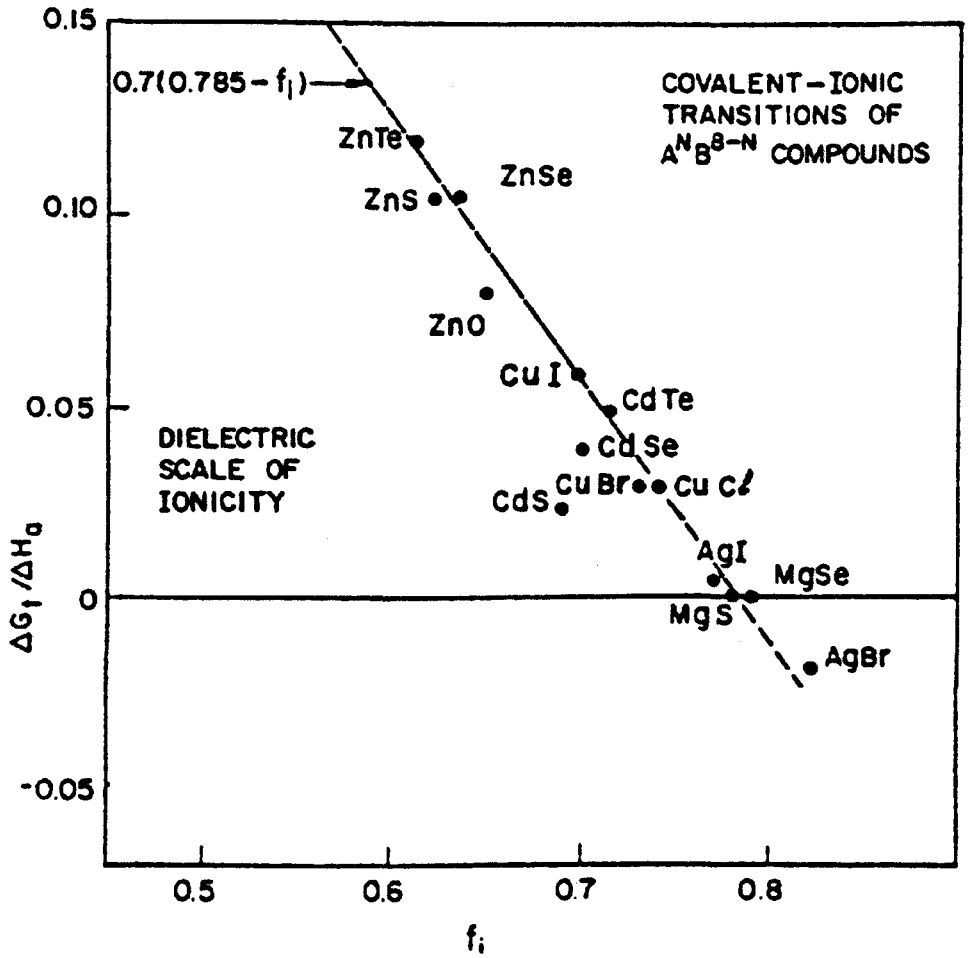

Figure 4.19: Graph of free energy versus ionicity, taken from Navrotsky and Philips [38].

and a low value implies that the bond angle can be easily distorted. In comparison, the values for MgS are at least twice as large.

4.10 Summary

A novel growth technique has been used to grow thick layers of up to 68nm of zinc blende MnS. The process involves the use of ZnS and Mn sources, instead of an elemental S cracker cell. Only a small residual Zn content (~3%) remains in the MnS layer as determined by both SIMS and Auger Spectroscopy.

XRI techniques were used to determine the thickness of thin MnS layers inserted in ZnSe. The information obtained was used to calculate the growth rate of 0.15 μmh^{-1}. Growth of the thick MnS layers has enabled the characterisation of this material by XRD for the first time. The lattice parameter of zinc blende MnS was determined from the 004 and 115 reflections to be 5.559 Å ± 0.002 Å.

Improvements to the total thickness of the material grown were obtained by including a thin ZnSe spacer layer prior to MnS deposition. The maximum thickness achieved using this method was 132 nm and improvement in the material quality was observed in the XRD rocking curves. This value is the thickest recorded to date for ZB MnS.

AFM topography of MnS layers show the development of 1-dimensional ridges along the [110] direction. Suggestions have been made as to the cause of this

development, however X-ray reciprocal space mapping is required to correctly identify the mechanism.

The conversion from the metastable zinc blende to the stable rocksalt crystal structure has been discussed, as well as the criteria outlined in Froyen *et al.* [35] for phase transitions in materials. The high value of Poisson's ratio for ZB MnS, which was determined from the XRI results, has also been discussed.

References

[1] N. Samarth, H. Luo, J.K. Furdyna, S.B. Qadri, Y.R. Lee, A.K. Ramdas and N. Otsuka, Appl. Phys. Lett. **54** (1989) 2680

[2] A.G. Cullis, G.M. Williams, B. Cockayne, P.J. Wright, P.W. Smith, P.J. Parbrook and M.P. Halsall, Inst. Phys. Conf. Ser. **100** (1990) 217

[3] R.I. Hines, N.L. Allan, G.S. Bell and W.C. Mackrodt, J. Phys. Condens. Matter **9** (1997) 7105

[4] B.J. Skromme, Y. Zhang, D.J. Smith and S. Sivananthan, Appl. Phys. Lett. **67** (1995) 2690

[5] O. Goede, W. Heimbrodt, V. Weinhold, E. Schnürer and H.G. Eberle, Phys. Stat. Sol. (b) **143** (1987) 511

[6] O. Goede, W. Heimbrodt and V. Weinhold, Phys. Stat. Sol. (b) **136** (1986) K49

[7] O. Goede, W. Heimbrodt, M. Lamla and V. Weinhold, Phys. Stat. Sol. (b) **146** (1988) K65

[8] B.J. Skromme, Y. Zhang, W. Liu, B. Parameshwaran, D.J. Smith, and S. Sivananthan, in *Growth, Processing, and Characterization of Semiconductor Heterostructures*, edited by G. Gumbs, S. Lieryi, B. Weiss, and G.W. Wicks, MRS Symposia Proceedings No. 326 (Materials Research Society, Pittsburgh, 1994) 15.

[9] S. Sivananthan, L. Wang, R. Sporken, J. Chen, B.J. Skromme and D.J. Smith, J. Crystal Growth **159** (1996) 94

[10] C. Bradford, C.B. O'Donnell, B. Urbaszek, K.A. Prior and B.C. Cavenett, Phys. Rev. B **64** (2001) 195309

[11] V. Bosquet, C. Ongaretto, M. Laugt, M. Behringer, E. Tournie and J.-P. Faurie, J. Appl. Phys. **81** (1997) 7012

[12] J. Massies and J.P. Contour, J. Appl. Phys. **58** (1985) 806

[13] L.H. Kuo, K. Kimura, T. Yasuda, S. Miwa, C.G. Jin, K. Tanaka and T. Yao, Appl. Phys. Lett. **68** (1996) 2413

[14] C. Bradford, K.A. Prior and B.C. Cavenett, Phys. Stat. Sol. (c) **1** (2004) 645

[15] E. Hecht, Optics, 2nd edition, Addison-Wesley (1987)

[16] D. K. Bowen and B. K. Tanner, High Resolution X-ray Diffractometry and Topography, Taylor & Francis Ltd. (1998)

[17] L. Tapfer, K. Ploog, Phys. Rev. B **40** (1989) 9802

[18] B. K. Tanner, J. Phys. D: Appl. Phys. **26** (1993) A151

[19] K.A. Prior, X. Tang, C. O'Donnell, C. Bradford, L. David and B.C. Cavenett, J. Crystal Growth **251** (2003) 565

[20] C. Bradford, PhD Thesis, Heriot-Watt University (2003)

[21] O. Yastrubchak, J. Bar-Misiuk, E. Lusakowska, J. Kaniewski, J.Z. Domagala, T. Wosiński, A. Shalimov, K. Regiński and A. Kudla, Physica B **340-342** (2003) 1082

[22] P. Krapf, Y. Robach, M. Gendry and L. Porte, J. Crystal Growth **181** (1997) 337

[23] H. Brune, M. Giovannini, K. Bromann and K. Kern, Nature **394** (1998) 451

[24] R.J. Asaro and W.A. Tiller, Metall. Trans. A **3** (1972) 1789

[25] M.A. Grinfeld, Soviet Phys. Dokl. **31** (1986) 831

[26] R.J. Nelmes and M.I. McMahon, Semicond. Semimet. **54** (1998) 145

[27] H. Sowa, Z. Crystallogr. **215** (2000) 335

[28] M. Wilson, F. Hutchinson and P.A. Madden, Phys. Rev. B **65** (2002) 094109

[29] M. Catti, Phys. Rev. B **65** (2002) 224115

[30] A. Kelly, G.W. Groves and P. Kidd, Crystallography and Crystal Defects, revised ed. (Wiley, Chichester, 2000)

[31] N.E. Christensen, S. Satpathy and Z. Pawlowska, Phys. Rev. B **36** (1987) 1032

[32] B.F. Levine, Phys. Rev. B **7** (1973) 2591

[33] R.C. Evans, An Introduction to Crystal Chemistry (Cambridge University Press, 1966)

[34] D. McKie and C. McKie, Crystalline Solids (Nelson, 1974)

[35] S. Froyen, S-H. Wei and A. Zunger, Phys. Rev. B **38** (1988) 10124

[36] D. Wolverson, D.M. Bird, C. Bradford, K.A. Prior and B.C. Cavenett, Phys. Rev. B **64** (2001) 113203

[37] F. Drief, A. Tadjer, D. Mesri and H. Aourag, Catalysis Today **89** (2004) 343

[38] A. Navrotsky and J.C. Phillips, Phys. Rev. B **11** (1975) 1583

[39] W.A. Harrison, Electronic Structure and Properties of Solids (W.W. Freeman, San Francisco, 1980)

Chapter 5: Characterisation of heterostructures containing MnS

5.1 Introduction

This chapter details the characterisation carried out on heterostuctures of MnS with either ZnSe or MgS layers. First, a series of thin MnS layers were grown on layers of ZnSe in order to determine the Valence Band (VB) offset between ZnSe and MnS. X-ray Photoelectron Spectroscopy (XPS) data was taken at National Centre for Electron Spectroscopy and Surface Analysis (NCESS), which is part of the Central Laboratory of the Research Councils' Daresbury laboratory, and used to calculate the VB offset. The calculation is detailed here and the result showed a small VB offset with a type II band alignment.

Although the XPS results indicated that the VB offset between ZnSe and MnS is a type II offset, a series of ZnSe quantum wells (QW) with MnS barriers were grown for completeness. Photoluminescence (PL) results from these structures will be discussed in this chapter.

Completely metastable structures of MnS QW's in MgS barriers have been successfully grown with no evidence of degradation in morphology observed in the RHEED pattern. PL from these structures is discussed in this chapter. Raman spectroscopy was also carried out on layers of MnS, preliminary results are discussed in Chapter 7.

5.2 X-Ray Photoelectron Spectroscopy (XPS)

The technique of X-ray Photoelectron Spectroscopy (XPS) has been discussed previously (section 3.4, [1]). In this chapter, the XPS spectra were obtained at NCESS at the CLRC Daresbury Laboratory in Warrington, UK, using a Scienta ESCA 3000 spectrometer. The XPS measurements were used to monitor the core levels of Mn, S, Zn and Se as the thickness of the MnS layer was increased and from these measurements, the valence band offset between ZnSe and MnS was determined using an indirect method [2].

5.2.1 Previous XPS work on MnS

XPS experiments on zincblende MnS layers have been previously carried out by L. Wang *et al.* [3]. The layers were grown on (100) GaAs substrates, which were etched in a 4:1:1 solution of H_2SO_4:H_2O_2:H_2O and rinsed in HCl and H_2O before being loaded into the MBE system. The surface of the GaAs was cleaned by heating the substrate to approximately 600°C. A ZnSe buffer was deposited at a growth temperature of 350°C, using elemental Zn and Se sources, before the growth of MnS layers. The MnS layers were grown using a conventional effusion cell for the elemental Mn and a sulphur cracker cell producing S_2. The growth temperature of the MnS was between 100 and 125°C, which was necessary to maintain the ZB structure. This growth technique yielded layers of up to 50 nm thick without loss of crystallinity.

An SSX-100 instrument with a monochromatic and focused Al Kα x-ray source and a hemispherical analyser with a constant pass energy was used to take the XPS measurements. A spot size of 300 μm diameter and a pass energy of 25 eV was used, resulting in a resolution of 700 meV. The XPS experiments were carried out under UHV conditions in a dedicated chamber connected to the growth chamber. The growth of the MnS layer was interrupted several times and the sample transported to the XPS chamber for analysis. Figure 5.1 shows the structure of the sample and indicates the thicknesses at which the XPS scans were taken.

The spectra obtained are shown in Figure 5.2. They were analysed by subtracting a Shirley-type background [4] then fitting them to the sum of several spin-orbit doublets with mixed Gaussian-Lorentzian line shape. The Se *3p* and Zn *3d* spectra shift to slightly lower binding energy upon the first deposition of MnS (0.5 nm) due to different band bending, but their position does not alter with the subsequent increase in MnS thickness. For thin layers, the binding energy of the S *2p* core level decreases slightly (about 150 meV) with increasing thickness. For the 30 nm layer, the S *2p* core level shows a weaker emission near 164 eV, which was determined to be due to elemental sulphur on the surface present because the S flux was maintained during the initial cooldown after growth.

The Mn *3p* core levels are also shown in Figure 5.2. Two methods were used to analyse the binding energy position of the MnS *2p* core levels. The first method was to determine the position from the half-width point at half height. This was done after subtracting either a linear base line or Shirley-type background. The second method involved fitting a single peak of mixed Gaussian-Lorentzian line

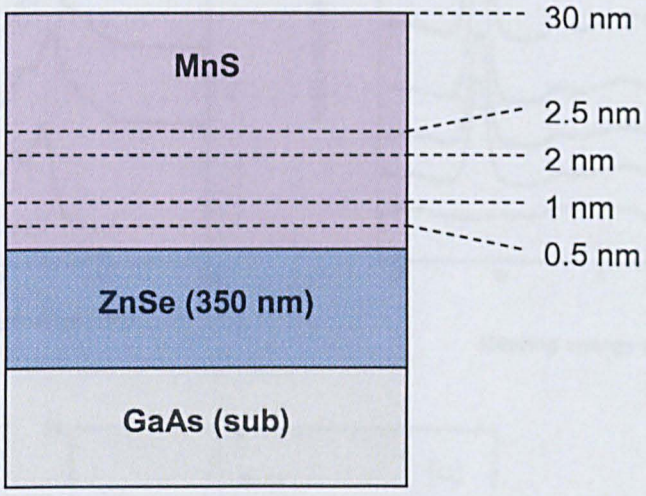

Figure 5.1: Structure schematic of MnS sample analysed by Wang *et al.* [3]. Thicknesses at which the XPS measurements were taken are indicated.

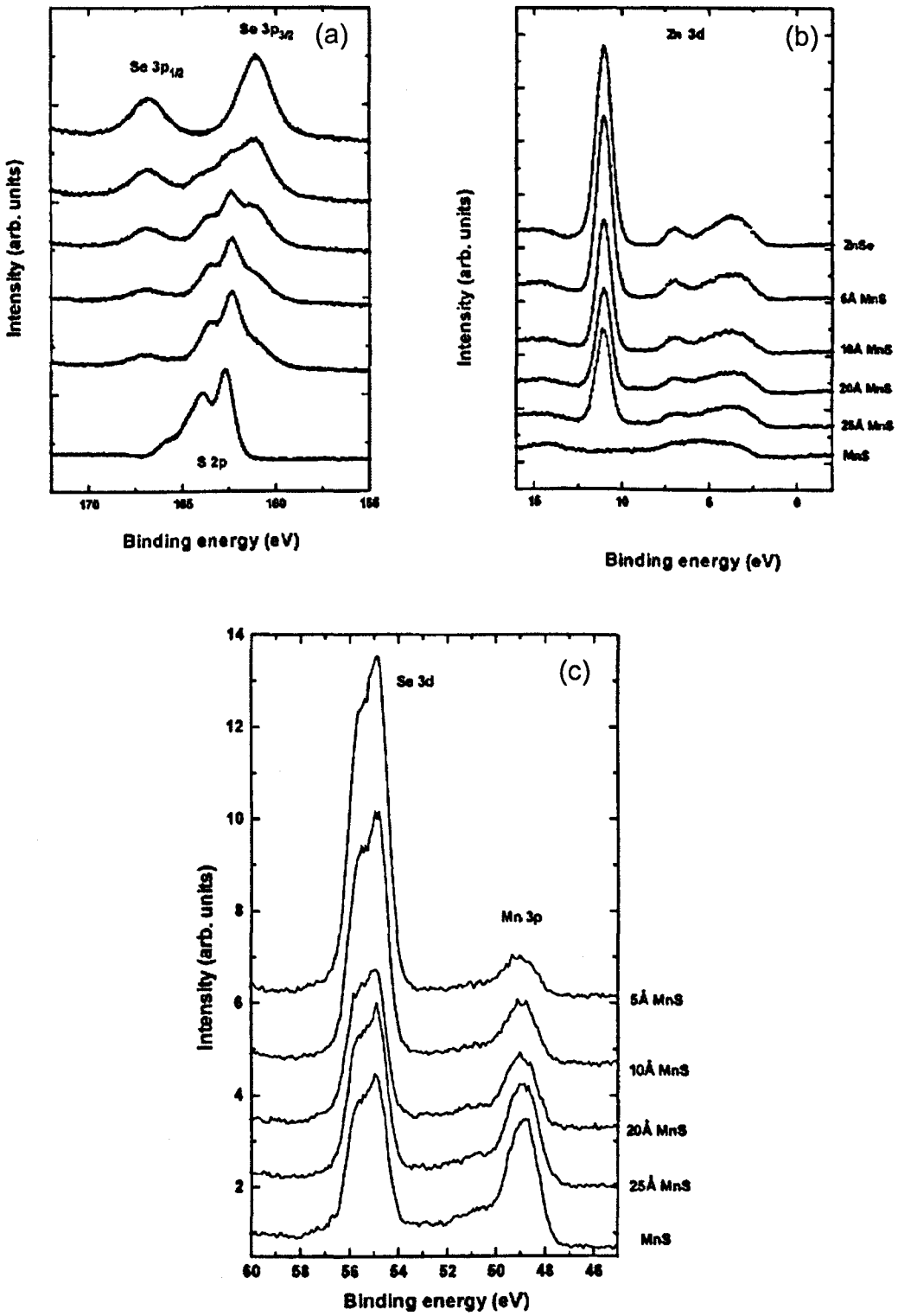

Figure 5.2: XPS spectra from Wang *et al.* (a) shows the Se *3p* and S *2p* core levels, (b) the Zn *3d* core level and valence band and (c) is from the Se *3d* and Mn *3p* core levels.

shape to the spectrum. The centre of this peak followed the position of the half-width at half height within 50meV. The position of the Mn *3p* peak was found to be independent of MnS thickness, except for the 30 nm layer, for which the Mn *3p* followed the S *2p* peak.

In the valence band, no new features were observed at any stage of the growth. Instead, the MnS valence band progressively replaced the one from ZnSe. It was concluded that there was no significant reaction at the ZnSe / MnS interface. None of the elements were detected in a different electronic environment than the pure binary compounds, within the resolution of the spectrometer. It was suggested that the interface formation starts with the adsorption of sulphur since the S peak was the only one to change position as a function of MnS thickness.

The valence band offset was calculated using the same method that was used in the present MnS work (section 5.2.4). The valence band maxima of ZnSe and MnS were determined by linear extrapolations of the leading edge spectrum, which again was the same method as used in the present work. A type II valence band discontinuity of 150 ± 100 meV was found.

5.2.2 XPS analysis of Heriot-Watt samples

A series of four MnS samples were produced, using the growth method described in Chapter 4, for XPS measurements. Each sample has the structure, GaAs (substrate) / ZnSe (50 nm) / MnS (X nm), where X ranges from 0 to 15 nm (Table 5.1). After growth, the samples were capped with Se by exposing the surface to a

Se flux for 30mins while the sample cooled from T_{sub} = 330°C to ~150°C. The cap was intended to protect the surface of the samples because they were grown over a period of a month before the scans were taken. An additional method used to protect the surface was to store the samples in the preparation chamber of the MBE system, at a pressure of $2x10^{-8}$ mbar, after growth to minimise exposure to air. Additional reference spectra were obtained from a single layer ZnSe sample, and from the thickest MnS sample, HWA1528, which has the structure ZnSe (50 nm) / MnS (23 nm) / ZnSe (18 nm) / MnS (132 nm).

Table 5.1: XPS sample numbers with MnS layer thickness.

Sample No	MnS thickness (nm)
HWA1530	0
HWA1535	0.5
HWA1537	1
HWA1545	2.3
HWA1547	15

The samples were transported to Daresbury and secured on the sample holder by two screws and then placed into the entry lock of the ESCA system, as discussed in section 3.4. Spectra were obtained from the samples both before and after thermal removal of the Se cap. The cap was removed by heating the sample to ~300°C for ~1 hour in the preparation chamber of the ESCA system. Comparisons of the scans taken before and after Se removal showed no distinct difference in any of the peak positions or intensity, it is possible that the cap degraded during transport to the Daresbury facility or the 30 minute cooling time with Se exposure was not long enough to produce a layer which stayed coherent on exposure to air.

Initially a fast survey scan (Figure 5.3), covering the full range of energies (0 – 1300 eV), was collected in order to identify the elements present on the sample surface. Based on the information obtained, higher energy resolution spectra were taken over energy ranges of interest. Table 5.2 shows the energies of interest in this study as well as the associated core element.

Table 5.2: Energies of core elements of interest.

Element	Core Level	Energy (eV) [5]
Zn	3d	9.7
Mn	3p	47.0
Se	3d	54.9
Se	3p	161.7
S	2p	164.0

5.2.3 Analysis

All the spectra obtained were analysed by fitting curves of mixed Gaussian and Lorentzian (Voigt) line shapes [6], added to a Shirley type background [4] by the ESCA300 software. The result of the curve fitting for the S *2p* and Se *3p* core levels from a MnS layer 1 nm thick can be seen in Figure 5.4. The experimental data is displayed as red dots and the green curve indicates the calculated fit.

Figures 5.5 – 5.7 show the spectra obtained from increasing thicknesses of MnS on ZnSe. The uppermost spectrum in each figure is from the thick (50nm) layer of ZnSe. The lowest spectrum is from the thickest layer of MnS grown to date with the

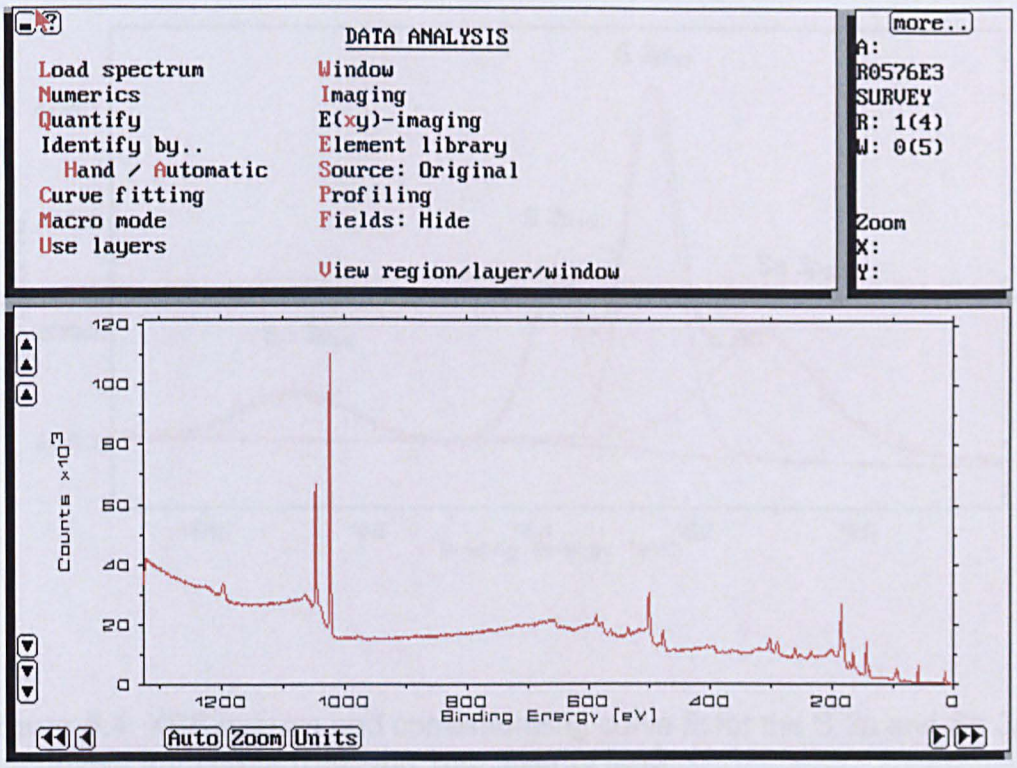

Figure 5.3: Screenshot of the ESCA300 software showing the fast survey scan from HWA1530, the 50nm ZnSe layer under study.

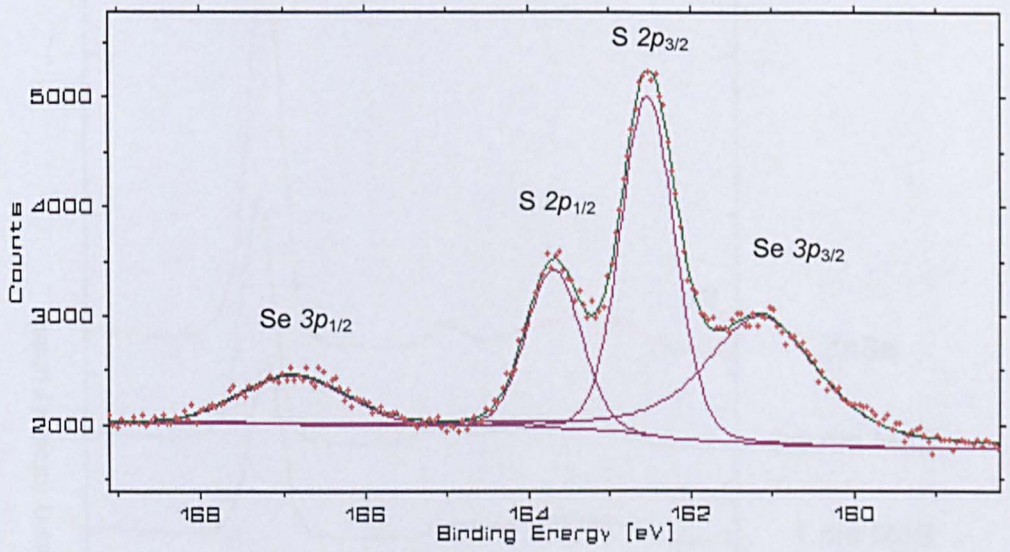

Figure 5.4: XPS spectra and corresponding curve fit for the S *2p* and Se *3p* core levels from HWA1537, the 1nm layer of MnS.

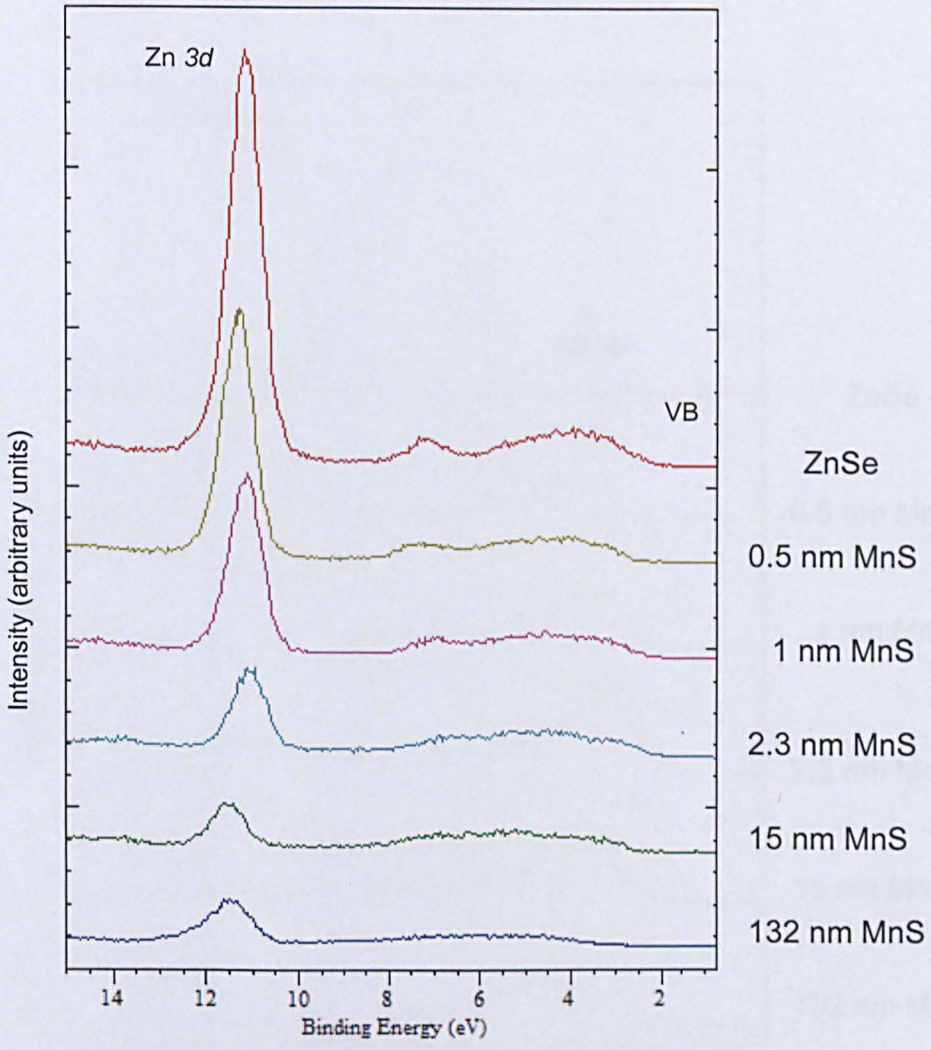

Figure 5.5: XPS spectra from the Zn 3*d* core level and the valence band. The uppermost spectrum is from the 50 nm layer of ZnSe and the lower spectra are from MnS layers of increasing thickness.

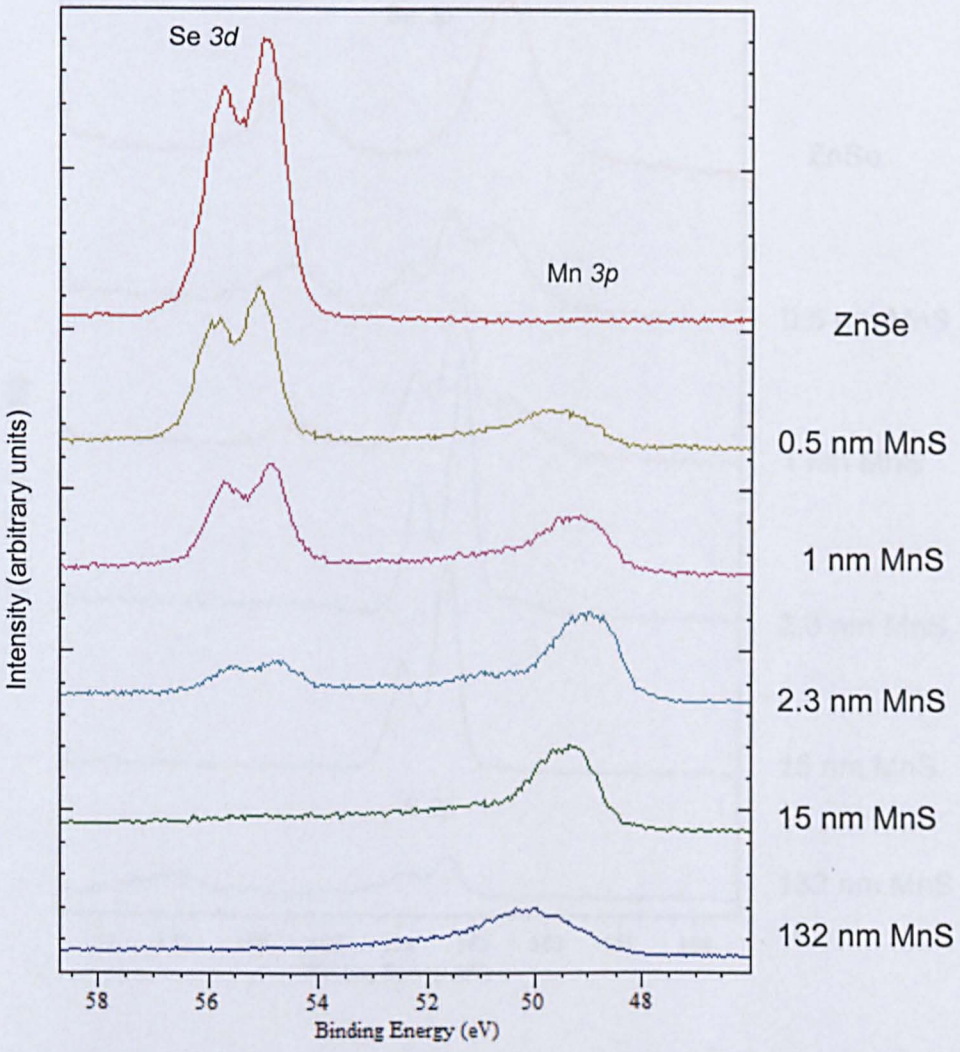

Figure 5.6: XPS spectra from the Se 3*d* and Mn 3*p* core levels. The spectra show that as the MnS layer increases the emission from the Se 3*d* core level decreases and is absent in the spectra from the 15 nm and 132 nm layers. The Mn 3*p* core level emission intensity increases as the MnS thickness increases. Results from the 132 nm MnS layer are discussed in section 5.2.4.

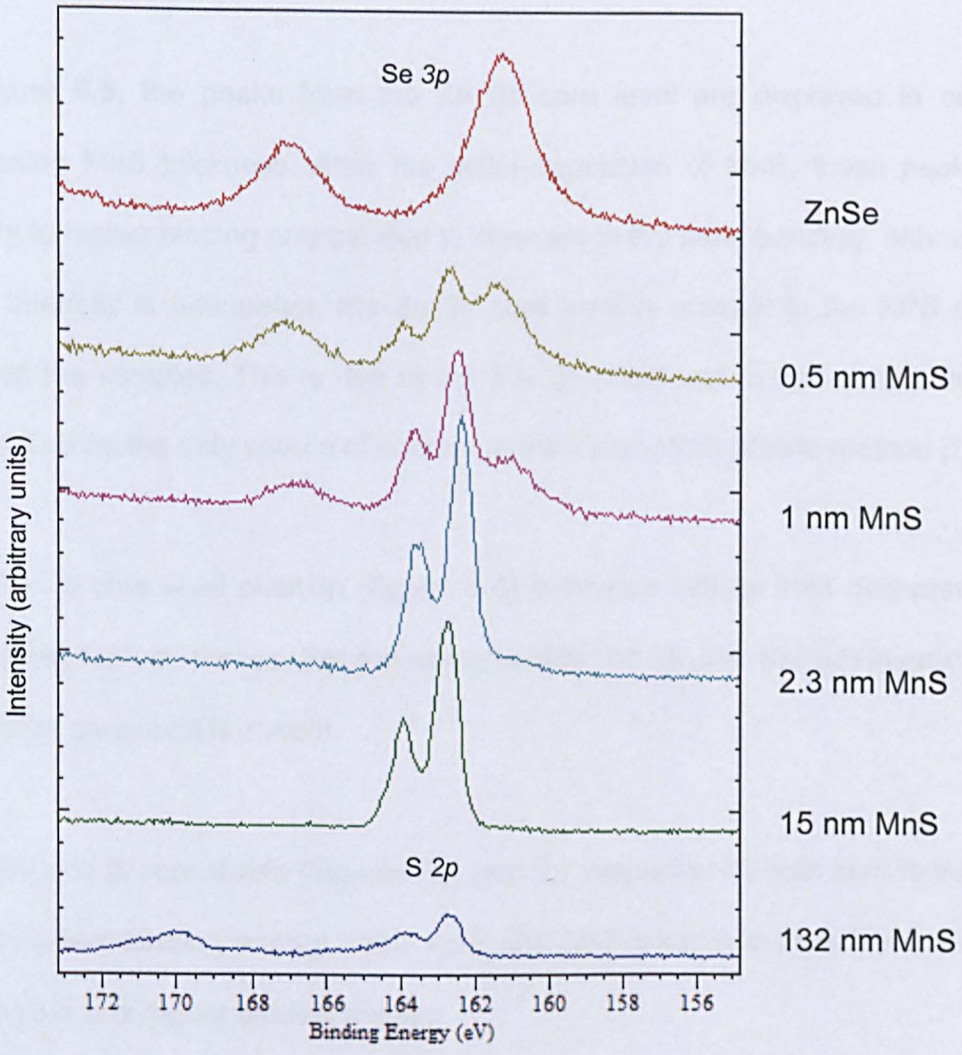

Figure 5.7: XPS spectra from the S 2*p* and Se 3*p* core levels. As the MnS thickness increases, the S 3*p* core level increases and the Se 3*p* core level decreases. The results from the 132 nm MnS layer are discussed in section 5.2.4.

structure ZnSe (53 nm) / MnS (23 nm) / ZnSe (18 nm) / MnS (132 nm). The spectra in between are from various thin layers of MnS in order of thickness.

In Figure 5.5, the peaks from the Zn *3d* core level are displayed in order of increasing MnS thickness. After the initial deposition of MnS, these peaks shift slightly to higher binding energy, due to changes in the band bending. Although the peak intensity is attenuated, the Zn *3d* core level is present in the XPS spectra from all the samples. This is due to the 3% Zn incorporation that occurs from the use of ZnS as the only source of sulphur in the Heriot-Watt growth method [7].

The Se *3d* core level position (Figure 5.6) increases initially then decreases with increasing MnS thickness. For the samples with the 15 and 132 nm layer of MnS, the Se *3d* core level is absent.

The Mn and S core levels (Figures 5.6 and 5.7 respectively) both shift to initially a slightly lower binding energy, then when the MnS layer is a thick layer, the core levels shift to a higher binding energy.

In the previous study [3], it was found that only the S peak position changed slightly as a function of MnS thickness. In the present work, there was a clear change in the Mn peak position as a function of the MnS thickness, which is associated with the chemical shift of the Mn. This suggests that the interface between the ZnSe and MnS layers in this case comprises of a plane of Mn atoms. In the previous study, it was determined that the interface would be a layer of S atoms (Figure 5.8). This difference between the two studies is believed to be real and reflects the

Heriot-Watt growth

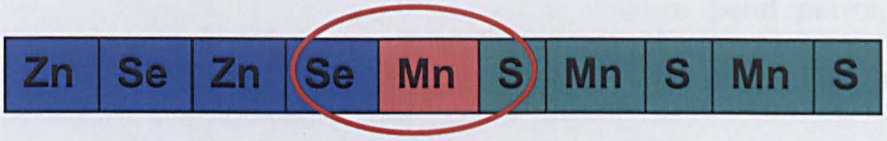

Consistent with XRI - MnSSe

Wang *et al.* [3] growth

Figure 5.8: Schematic of interface between ZnSe and MnS for both the previous growth method and the one presented in this thesis.

different growth methods used to prepare the two sets of samples. From Figure 5.8, it can be seen that an interface layer of MnSSe forms during the growth of MnS at Heriot-Watt, which is consistent with the layer observed by XRI analysis in section 4.4.1.

No striking new features were observed in the valence band peaks, as the thickness of the MnS layer was increased. The MnS valence band progressively replaces that of the ZnSe (see Figure 5.5).

5.2.4 Calculation of the Valence Band Offset

In order to determine the valence band offset, an indirect procedure was used since the offset is known to be small [3]. This procedure [8] uses the separation of the valence band maximum and a core level position for each of the binary compounds as well as the separation of the same core levels at the interface (Figure 5.9). The equation used to calculate the valence band offset is:

$$\Delta E_v = (E_v - E_{CL})_{MnS} - (E_v - E_{CL})_{ZnSe} + \Delta E_{CL}$$

Where $(E_v - E_{CL})_{MnS}$ is the difference between the valence band maximum of MnS and the core level of either Mn or S, $(E_v - E_{CL})_{ZnSe}$ is the difference between the valence band maximum of ZnSe and the core level of either Zn or Se, and ΔE_{CL} is the difference between the chosen core levels at the interface.

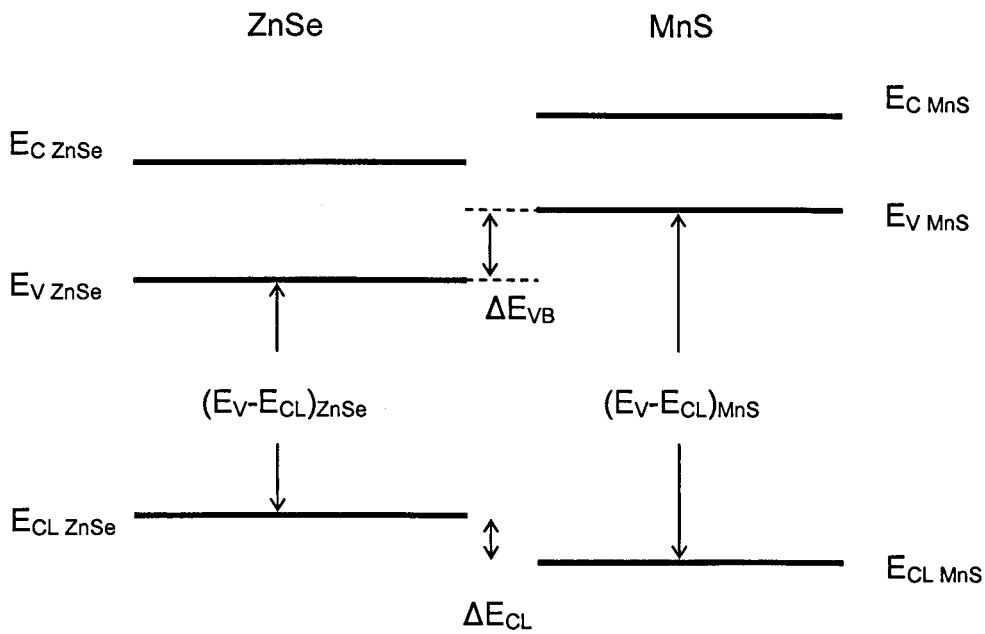

Figure 5.9: Schematic energy band diagram for the ZnSe / MnS interface, indicating the method used to determine the VB offset.

The above calculation requires the valence band maximum and core levels from two reference samples, one a thick layer of ZnSe and another thick MnS layer. Figure 5.10 shows the XPS spectrum obtained from the 132 nm thick layer of MnS, over the energy range 0-200 eV. Although the peaks attributed to the Zn, S and Mn core levels are clearly visible, there are other peaks present not found in spectra from the other samples.

The peaks at energy 168-172 eV ((a) in Figure 5.10) have been determined to be the result of sulphur oxides present on the surface [5]. The peak labeled (b) at 25 eV is from the oxygen *2s* core level confirming the slight oxidisation of the surface. This sample is the thickest layer of MnS grown to date, and was not intentionally produced for the XPS study. Therefore it was not capped with Se or stored under vacuum, as the other samples were.

Due to the presence of these oxide peaks, this spectrum cannot be used as the MnS reference spectrum in the calculation of the VB offset. Therefore the spectra obtained from the ZnSe layer and the 15 nm thick MnS layer have been used as references.

The valence band maxima of the reference samples have been taken to be the intercept between a linear fit of the leading edge in the photoelectron spectra and a horizontal background [3] shown in Figure 5.11. A more accurate determination can be found by comparing the measured spectra to a theoretical density of states, however there is no such theoretical calculation for MnS at this time.

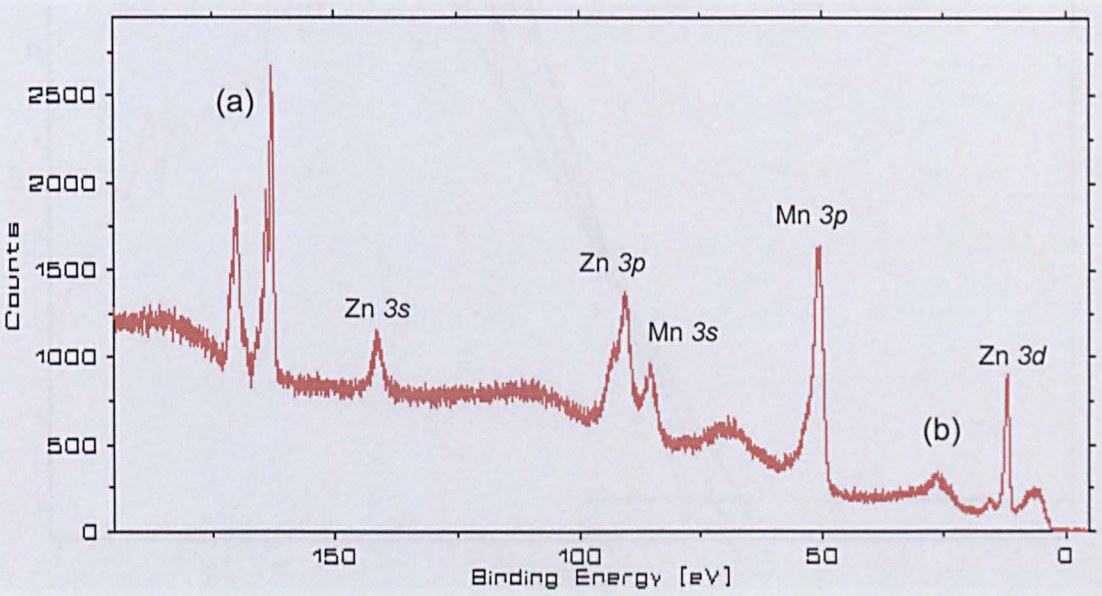

Figure 5.10: XPS spectrum from HWA1528, a 132 nm layer of MnS.

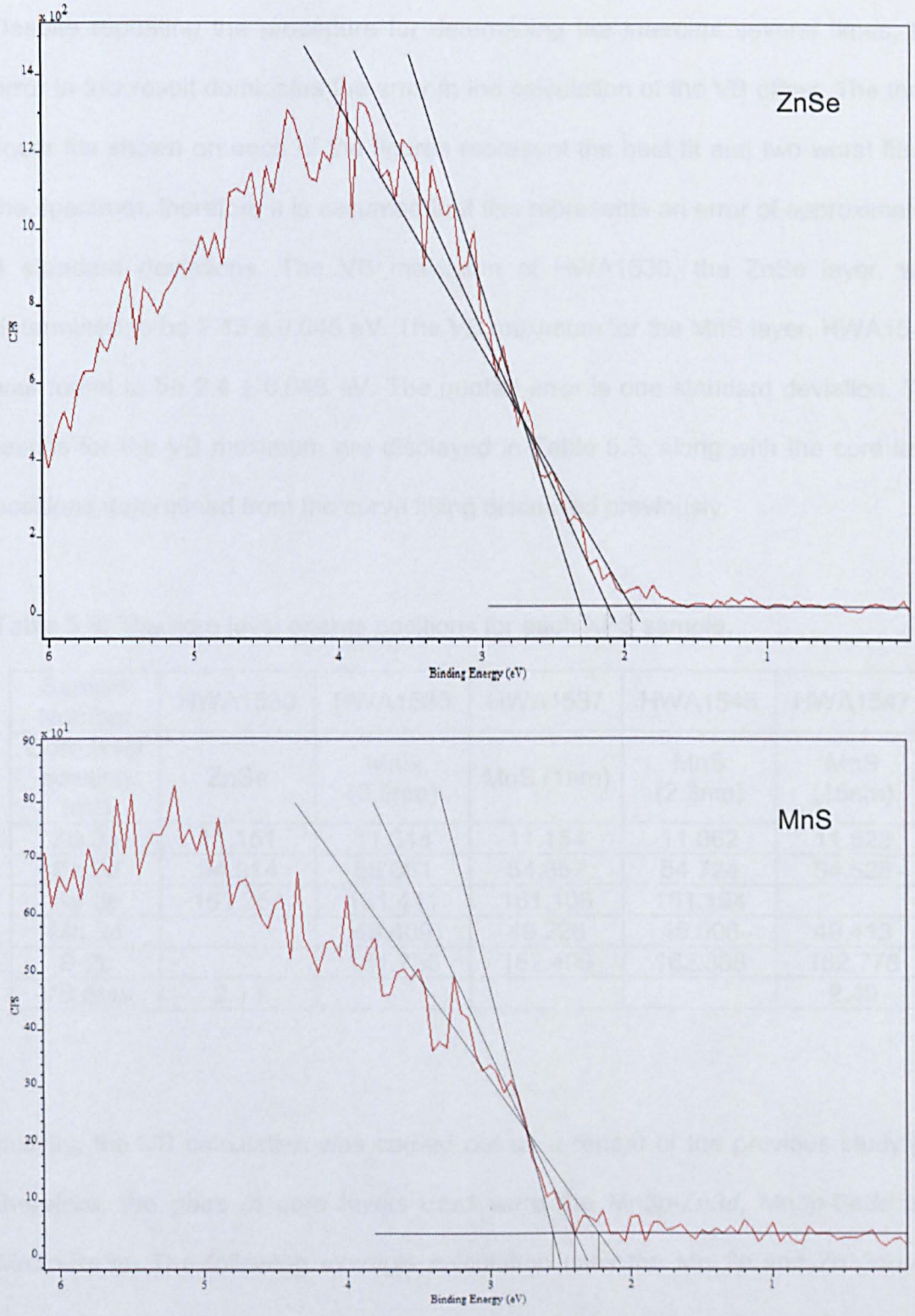

Figure 5.11: Determination of the valence band maximum of the 50 nm ZnSe layer and 15 nm MnS layer by linear extrapolation of the leading edge in the spectrum.

Despite repeating the procedure for determining the intercept several times, the error in this result dominates the error in the calculation of the VB offset. The three linear fits shown on each of the figures represent the best fit and two worst fits to the spectrum, therefore it is assumed that this represents an error of approximately 4 standard deviations. The VB maximum of HWA1530, the ZnSe layer, was determined to be 2.13 ± 0.045 eV. The VB maximum for the MnS layer, HWA1547, was found to be 2.4 ± 0.045 eV. The quoted error is one standard deviation. The results for the VB maximum are displayed in Table 5.3, along with the core level positions determined from the curve fitting discussed previously.

Table 5.3: The core level energy positions for each XPS sample.

Sample Number	HWA1530	HWA1535	HWA1537	HWA1545	HWA1547
Core level position (eV)	ZnSe	MnS (0.5nm)	MnS (1nm)	MnS (2.3nm)	MnS (15nm)
Zn *3d*	11.151	11.314	11.154	11.062	11.523
Se *3d*	54.914	55.061	54.857	54.724	54.526
Se *3p*	161.254	161.411	161.108	161.194	
Mn *3p*		49.409	49.228	49.006	49.413
S *2p*		161.758	162.499	162.388	162.778
VB max	2.13				2.40

Initially, the VB calculation was carried out as a repeat of the previous study [3], therefore, the pairs of core levels used were the Mn*3p*-Zn*3d*, Mn*3p*-Se*3d* and Mn*3p*-Se*3p*. The following example calculation uses the Mn *3p* and Zn *3d* core levels.

$$\Delta E_v = (E_v - E_{CL})_{MnS} - (E_v - E_{CL})_{ZnSe} + \Delta E_{CL}$$

$$(E_v - E_{CL})_{ZnSe} = 2.13 - 11.151$$
$$= -9.021eV$$

$$(E_v - E_{CL})_{MnS\,15nm} = 2.40 - 49.4131$$
$$= -47.0131eV$$

$$\Delta E_{CL} = E_{CL}^{Mn} - E_{CL}^{Zn} \text{ at the different junctions}$$

Table 5.4: Difference in core level energy with reference to MnS thickness.

MnS thickness (nm)	0.5	1	2.3
ΔE_{CL} (eV)	38.0949	38.0739	37.9436

ΔE_{VB} was calculated for each of the three pairs of core levels and the average and standard deviation of the data taken (Table 5.5). The valence band discontinuity between MnS and ZnSe was found to be 79 ± 90 meV, using the Mn pairs of core level positions.

Table 5.5: VB offset calculated from each of the Mn *3p* core level pairs.

Core level pair	ΔE_{VB} for MnS thickness (meV)		
	0.5 nm	1 nm	2.3 nm
Mn *3p* – Zn *3d*	103	82	-49
Mn *3p* – Se *3d*	119	143	53
Mn *3p* – Se *3p*	109	231	-77
Average ΔE_{VB} (meV)	79		

When the interface is formed, the binding energy of the core levels can change due to a chemical shift or band bending. Only contributions from band bending can be

taken into account in the calculation of the VB offset. As stated previously, the Mn core level showed a clear change in position associated with the chemical shift of Mn. Therefore the Mn core level contributions should not be taken into account when calculating the ZnSe / MnS VB offset for these samples. Table 5.6 shows the ΔE_{CL} and ΔE_{VB} calculations using the S*2p*-Zn*3d*, S*2p*-Se*3d* and S*2p*-Se*3p* core level pairs.

Table 5.6: VB offset calculated from each of the S *2p* core level pairs.

Core level pair	ΔE_{VB} for MnS thickness (meV)		
	0.5 nm	1 nm	2.3 nm
S *2p* – Zn *3d*	87	-12	-31
S *2p* – Se *3d*	104	49	137
S *2p* – Se *3p*	94	137	-60
Average ΔE_{VB} (meV)	49		

Using the S *2p* core level pairs, the valence band offset between ZnSe and MnS was determined to be 49 ± 90 meV. The results from both calculations agree within the experimental error. However, as investigated by Nicolini *et al.* [9], the interface layer can affect the valence band offset between GaAs and ZnSe depending on whether it is Zn-rich (1.2 eV) or Se-rich (0.58 eV). As the interface in the present samples is Mn-rich and the previous study determined a S-rich interface, a direct comparison of the two results may not be valid.

According to this experiment, the valence band maximum of ZnSe is likely to be below that of MnS, and since the band gaps of ZnSe and MnS are 2.82 and 3.7 eV respectively, the band alignment would be type II (Figure 5.12).

The result for the VB offset determined in this study corresponds to the value determined in the previous study within the errors stated. Despite the improved energy resolution available at NCESS (400 meV compared to 700 meV previously), we have not been able to improve significantly the accuracy of the result compared to the work by L. Wang *et al.* [3]. This is because, as with the original study, the primary source of error in the uncertainty in calculating the VB offset is the determination of the VB edges. These were determined by empirical curve fitting, and without a theoretical model of the MnS density of states at the band edge, this result cannot be improved.

5.3 Photoluminescence of MnS heterostructures

The difference in bandgap between MnS and ZnSe is approximately 1 eV, which would give good confinement for carriers in ZnSe if the band alignment were type I. However as shown in the previous section and references [3], the band alignment between ZnSe and MnS is type II, with a small valence band offset of 49 ± 90 meV. This result implies that the holes created in the VB of the ZnSe quantum well (QW), due to excitement of the electrons, would not be confined in the QW. A series of single QW samples with the structure ZnSe buffer (50 nm) / MnS barrier (13 nm) / ZnSe QW (X nm) / MnS barrier (13 nm) were grown for PL measurements with X =

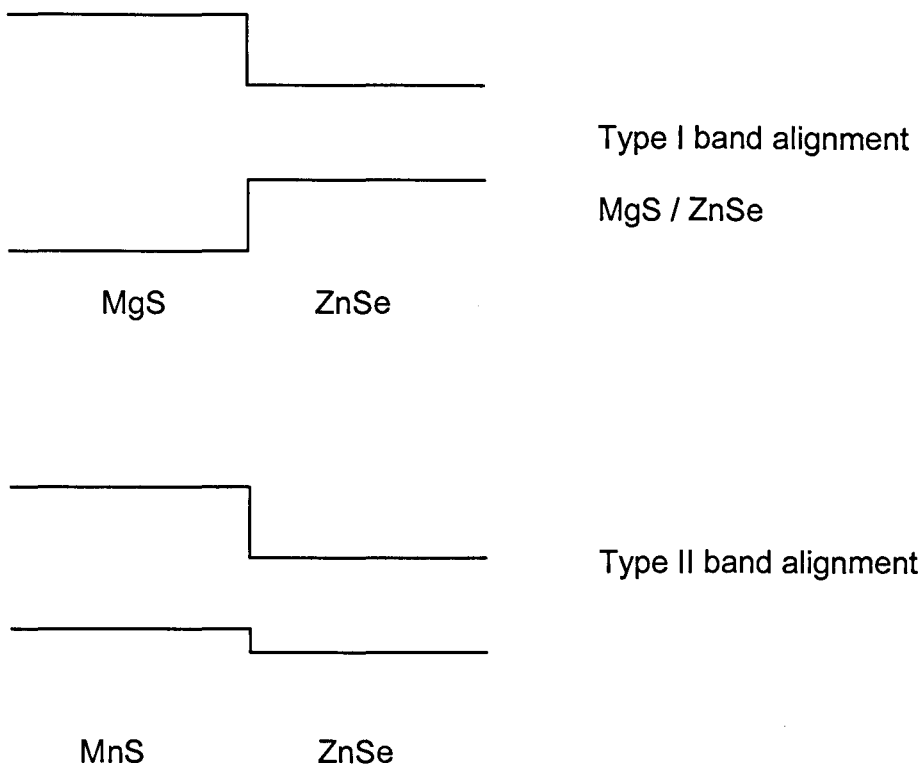

Figure 5.12: Schematic of type I and II band alignments.

2, 4 and 10 nm. Details of how the PL measurements presented here were taken, as well as discussion of the technique in general, can be found in section 3.6.

The XPS results show that ZnSe/MnS heterojunctions have a type II band alignment, however type II transitions [10] are not visible in the PL spectra obtained from these heterostructures. It is possible that the tetrahedral Mn transition at 2.13 eV overlaps the emission from the type II transitions (not shown in figure). A PL spectrum from the 4 nm well is shown in Figure 5.13 with emission at 2.88 eV. The inset in Figure 5.13 shows that as the well width is increased the emission energy also increases. PL spectra from the 2 and 10 nm wells are not shown as the signal to noise ratio is poor.

Since the lattice parameters of GaAs, ZnSe, MgS, and MnS are all similar, it is possible that completely metastable structures of MnS QW in MgS barriers can be grown. Sample HWA1510, a ~8 nm QW of MnS with 20 nm MgS barriers, was grown by Dr. Christine Bradford using the method outlined in Chapter 4. The structure is capped with ZnMgSSe in order to prevent the MgS layer oxidising in air.

The sample was grown with no degradation in morphology evidenced in the RHEED. The PL scan from this sample is shown in Figure 5.14. The emission peak marked (a) has been assigned as emission from the QW (MnS E_g = 3.7 eV). Since the barriers of MgS were grown to a thickness of 20 nm, ridges approximately 2 nm high will have formed on the surface of the MgS, which means that there will be a

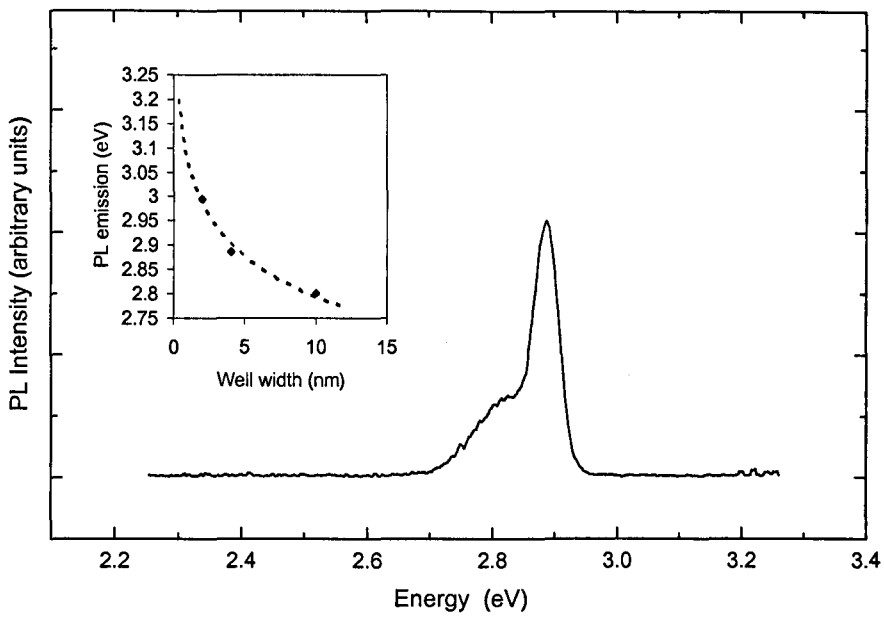

Figure 5.13: PL spectrum from HWA1520 with the structure MnS (13 nm) / ZnSe (4 nm) / MnS (13 nm). The inset shows the measured PL peak positions for equivalent structures with 2, 4 and 10nm thick ZnSe layers, and the best fit curve.

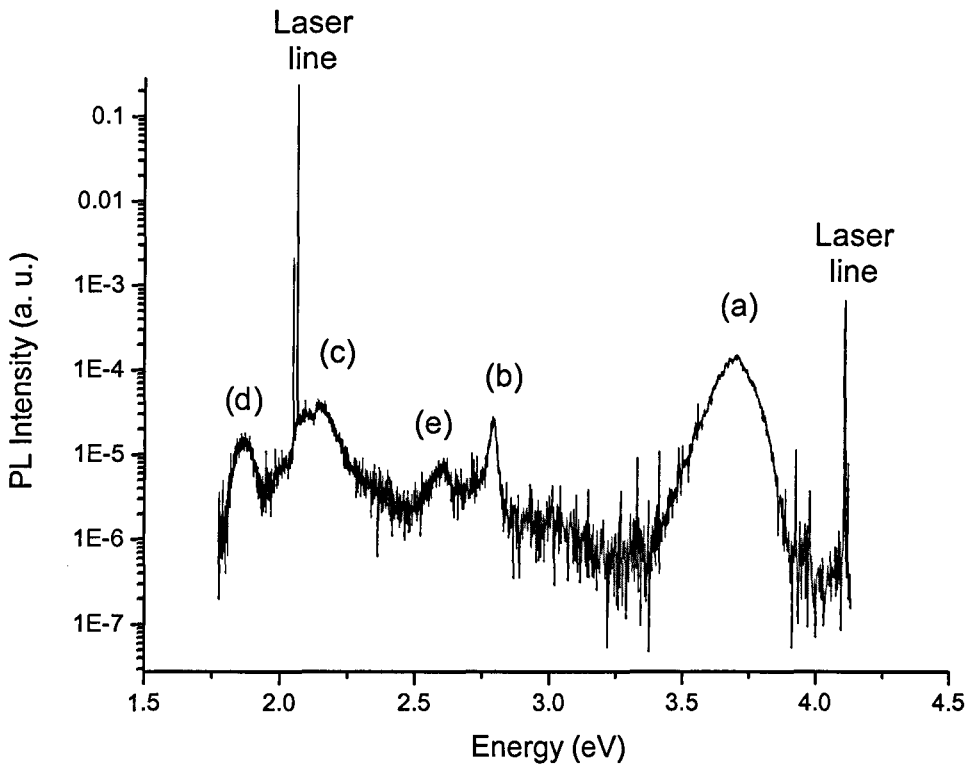

Figure 5.14: PL spectrum from HWA 1510, an 8 nm MnS QW with 20 nm MgS barriers.

range of QW thicknesses over the sample. The broad peak observed in Figure 5.14 is characteristic of emission from wells of different thicknesses [11].

Emission from the ZnSe buffer layer has been labeled as (b). Emission from buffer layers has been observed previously from layers of the same thickness as in this structure (50 nm) [12]. The peak labeled (c) has been assigned to the internal Mn transition [13], which, at an energy of 2.2 eV, indicates that the Mn atoms are in the tetrahedral co-ordination. The emission occurring at 1.8 eV (d) has been assigned as an emission from the GaAs substrate [14].

The final peak in the PL spectrum labeled (e) has not been uniquely identified, and there is a possibility that it is from a type II transition. Although the band alignment between MgS and MnS is not known, it has been previously stated that structures grown at Heriot-Watt involving MgS could not be anything other than type I [15]. However the "common-anion rule" [16] states that the valence band discontinuity at the interface will be very small for semiconductors that contain the same anion. Therefore there is the possibility that type II transitions could occur in this structure. The type II transition from the conduction band of the well to the valence band of the buffer layer would be equal to the energy gap of MnS minus the valence band discontinuity, and the peak labeled (e) is approximately 1 eV lower than the emission from the QW. This is much larger than the "common-anion rule" would suggest, therefore it is unlikely that the emission is from a type II transition.

5.4 Summary

XPS measurements were carried out on a series of MnS layers of varying thickness, which were used to monitor the core level positions and in turn determine the valence band offset between ZnSe and MnS. The XPS results showed that there was a shift in the energy of the Mn core levels as a function of MnS thickness, which indicates that the MnS layer is initiated with a layer of Mn atoms. This result is supported by XRI measurements, which indicate the presence of a 0.6 nm interface layer of MnSSe between MnS and ZnSe layers. The XPS data was then used to determine the valence band discontinuity between ZnSe and MnS. In agreement with a previous study, a type II discontinuity with a value of 48 ± 90 meV was obtained.

PL experiments were carried out on quantum well structures of both MnS / ZnSe and MgS / MnS. The type II valence band offset between MnS and ZnSe means that there is a lack of confinement in these structures, however emission from a 4 nm ZnSe well was measured at an energy of 2.88 eV.

Completely metastable structure of MnS quantum wells with MgS barriers have been produced with no evidence of degradation observed in the RHEED. Photoluminescence from a 8 nm well was presented with a broad emission peak at 3.7 eV, indicating that the ridges formed in MgS has produced wells of varying thicknesses. The presence of the internal Mn transition at 2.2 eV confirms that the MnS is in the zinc blende crystal structure.

References

[1] P. Weightman, Rep. Prog. Phys. **45** (1982) 753

[2] E.A. Kraut, R.W. Grant, J.R. Waldrop and S.P. Kowalczyk, Phys. Rev. B **28** (1983) 1965

[3] L. Wang, S. Sivananthan, R. Sporken and R.Candano, Phys. Rev. B **54** (1996) 2718

[4] D. Shirley, Phys. Rev. B **5** (1972) 4709

[5] Binding Energy Lookup Table, XPS International, www.xpsdata.com (1999)

[6] P.M.A. Sherwood, *Practical Surface Analysis Vol. 1: Auger and X-ray Photoelectron Spectroscopy*, edited by D. Briggs and M.P. Seah (John Wiley, 1990) Appendix 3, p. 555

[7] L. David, C. Bradford, X. Tang, T.C.M. Graham, K.A. Prior and B.C. Cavenett, J. Crystal Growth **251** (2003) 591

[8] J.R. Waldrop, R.W. Grant, S.P. Kowalczyk and E.A. Kraut, J. Vac. Sci. Technol. A **3** (1985) 835

[9] R. Nicolini, L. Vanzetti, G. Mula, G. Bratina, L. Sorba, A. Franciosi, M. Peressi, S. Baroni, R. Resta, A. Baldereschi, J.E. Angelo and W.W. Gerberich, Phys. Rev. Lett. **72** (1994) 294

[10] Y.T. Shih, Y.L. Tsai, C.T. Yuan, C.Y. Chen, C.S. Yang and W.C. Chou, J. Appl. Phys. **96** (2004) 7267

[11] Arran Curran, Private Communication

[12] A. Balocchi, A. Curran, T.C.M. Graham, C. Bradford, K.A. Prior and R.J. Warburton, Appl. Phys. Lett. **86** (2005) 011915

[13] B.J. Skromme, Y. Zhang, D.J. Smith and S. Sivananthan, Appl. Phys. Lett. **67** (1995) 2690

[14] M.D. Sturge, Phys. Rev. **127** (1962) 768

[15] K.A. Prior, C. Bradford, L. David, X. Tang and B.C. Cavenett, Phys. Stat. Sol. (b) **241** (2004) 463

[16] J.O. McCaldin, T.C. McGill and C.A. Mead, Phys. Rev. Lett. **36** (1976) 56

Chapter 6: Growth of CrS

6.1 Introduction

The successful growth of MnS has proven that the method developed for the growth of ZB MgS can be applied to any metal sulphide where the metal is less volatile than Zn. As a continuation of this work the growth of ZB CrS was started.

CrS was chosen as the next transition metal sulphide to be produced because of its interest in the field of spintronics. Dietl has predicted that antiferromagnetism, present in II-VI binary compounds such as MnS, is absent with other divalent transition metal ions. In particular, he has suggested that CrS should be ferromagnetic, with a high Curie temperature, even when undoped [1] based on previous work by Blinowski [2].

There are two important preliminary considerations that must be addressed before the successful growth of ZB CrS can occur. The first is the purity of the source material. For all the other sources in the MBE system the purity is 5N8 pure or higher. However, until 2002, commercial manufacturers could only provide Cr metal 4N pure. The source used in this work was purchased from Newmet Koch at a purity of 5N. With this improvement, temperature cycling during the cell outgas process could be used to increase the purity of the Cr still further. Details of the temperature cycling can be found in Chapter 2 of this thesis.

The second point to address is the choice of a suitable substrate material. The choice of substrate is dictated by the lattice parameter of the epitaxial layer to be grown. In order to lattice match an epitaxial layer to a substrate, the lattice constant for the ZB phase must be within approximately 1% of that substrate [3].

Before the start of this work, calculations were carried out at Heriot-Watt by Dr. Kevin Prior to determine the lattice parameter of ZB CrS. The lattice parameters of all the transition metal sulphides were calculated using atomic radii taken from the CaRIne Crystallography Version 3.1 software. The basic calculation is outlined and discussed in section 6.6.1. Figure 6.1a shows the initial graph of lattice parameter, *a*, for the series of first row transition metal sulphides. From the graph, it can be seen that the calculated lattice parameter of MnS is too large by 0.54 Å. An empirical scaling factor of 0.921 was then applied to correct the value of a_{MnS} and then applied to all the first row transition metal sulphides. It can be seen from Figure 6.1b, the final graph of lattice parameter with applied scaling factor, that the estimated lattice parameter of ZB CrS is 5.806 Å.

Using these initial calculations, work was started on the growth of CrS on InP substrates, with a lattice matched buffer layer of ZnCdSe. Details of how the InP substrates were prepared prior to growth are outlined in this chapter. Optimisation of the ZnCdSe buffer layer is also discussed as well as growth of the initial CrS layers, including why the work on this substrate was halted.

Subsequent literature research into the lattice parameter of CrS uncovered conflicting values, with different *ab initio* calculations determining the lattice

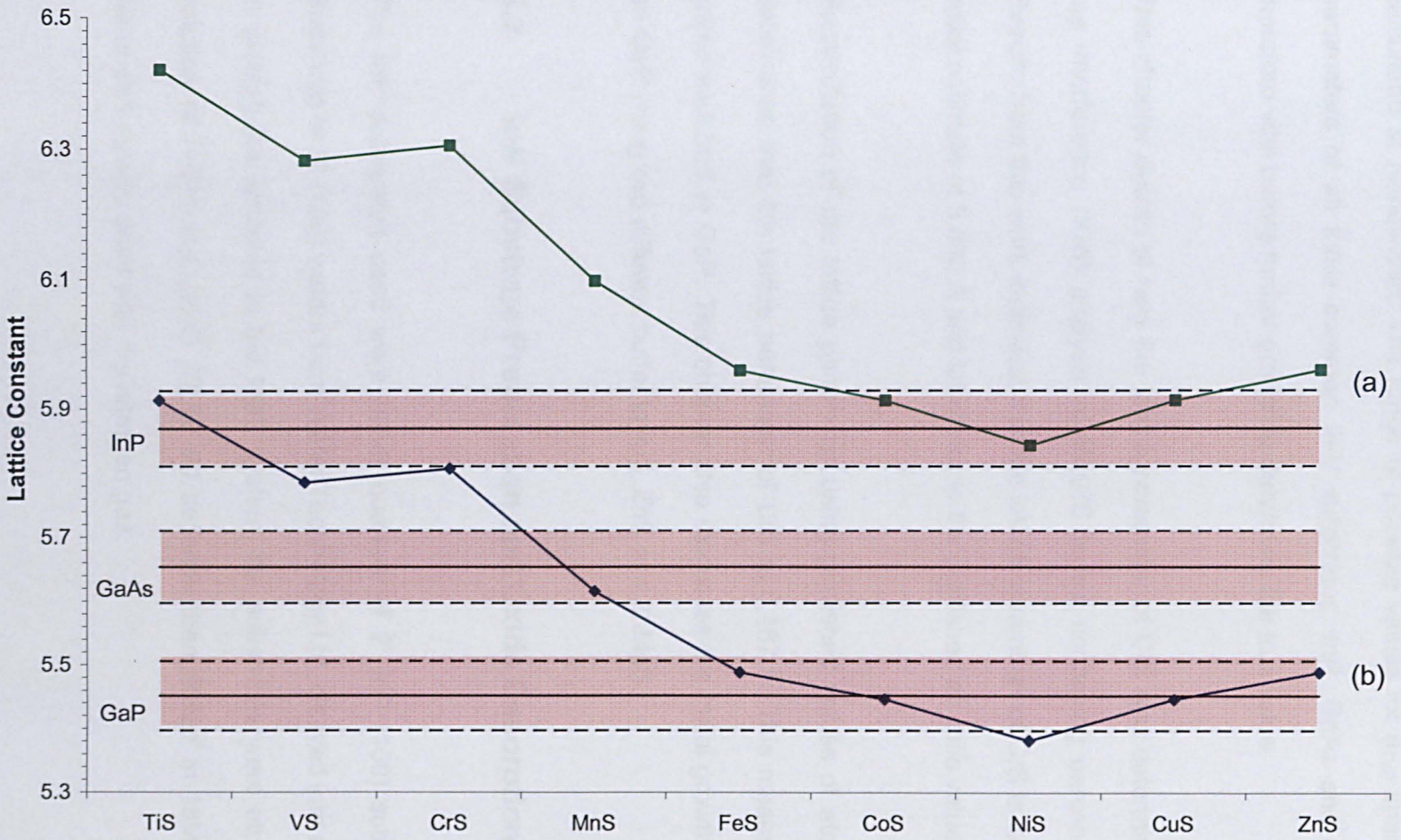

Figure 6.1: Graph of transition metal sulphide ZB lattice parameters. (a) shows initial values calculated with atomic radii from CaRIne software. (b) gives the values after the correction factor has been applied. The shaded areas indicate the lattice matching to the particular substrate.

parameter to be 5.04 Å [4] and 5.309 Å [5]. Both values are much lower than that calculated at Heriot-Watt. The range of possible values for a_{CrS} spans the lattice parameters of all three common III-V substrates; InP, GaAs and GaP. It was therefore vital before further growth to determine the true value.

This chapter details of how the lattice parameter of CrS was determined using X-ray Interference (XRI) analysis of MnCrS layers containing percentages of Cr. Results from this work indicated that the lattice parameter of CrS is lower than the initial estimate of 5.806 Å and far closer to the published *ab initio* values.

Recalculation of the lattice parameter using published values of atomic radii [6] determined that the lattice parameter of CrS is 5.487 Å. This means that CrS is lattice matched to GaP. This chapter also discusses the initial growths of ZB CrS on GaP using two different buffer layers, ZnS and ZnMgS.

6.2 InP Substrate Preparation and Oxide Desorption

The InP substrates used were either quarters of 2" InP (100) substrates from Suminoto or 3" (100) wafers from Wafer Technology Ltd, cleaved into eighths. Prior to placing the samples in the MBE system, the substrates were etched in 5:1:1 solution of H_2SO_4:H_2O_2:H_2O [7] for 90 seconds then rinsed in 18MΩ deionised water and quickly dried with dry nitrogen gas.

As with growth on GaAs substrates, molten indium was used to bond the wafer to the molybdenum substrate holder. Massies *et al.* [8] showed that the bonding process produces an oxide surface 2-3 nm thick dependant on the temperature used and time taken to bond the wafer.

Once mounted the sample was placed in the entry lock of the preparation chamber. In the preparation chamber the molybdenum substrate holder was flash heated to 200°C for 2 minutes 30 seconds to remove water from the sample and substrate holder before transfer to the growth chamber.

Removal of the oxide layer from InP is not straightforward because during the heating of the substrate, phosphorus is removed and the excess indium forms droplets on the surface. This formation is not visible in RHEED as the separation of the droplets is orders of magnitude larger than the RHEED coherence length. In III-V systems there is an overpressure of As or P during the heat clean which prevents the In buildup [9], which is not possible in a II-VI chamber.

Two different clean up techniques were compared to find which could best remove the surface oxide while minimising the density of the indium droplets. The first technique involved raising the substrate temperature slowly to a peak temperature in 50°C steps every 2 minutes. Increasing the temperature at this rate limited the possibility of overheating the sample. Once the temperature reached that peak, the power to the substrate heater was cut and the sample cooled to the growth temperature. During the cooldown the surface was monitored by RHEED, with the 4x reconstruction observed, indicating a smooth flat surface. The sample was then

removed from the MBE system and the surface was observed using an optical microscope.

Initially, the InP sample was heated to the point where the 4x reconstruction first becomes visible, 510°C (on the substrate thermocouple). Optical microscopy of the surface (Figure 6.2a) clearly shows the In droplets on the surface. The In droplet density can be calculated from the optical microscopy image. The scale of the image is 1cm : 19.8 μm and the image size is 77.4 cm^2. There are 151 droplets visible on the surface (shown in Figure 6.2a) which indicates that the In droplet density is ~ $5x10^5$ cm^{-2}.

Figure 6.2b shows the surface of an InP substrate that was heated to a substrate thermocouple temperature of 490°C. The density of the In droplets has reduced to ~ $2x10^5$ cm^{-2}, therefore by lowering the peak cut-off temperature, the density of the In droplets is reduced. Subsequent samples cleaned using this method were heated to 490°C.

The second method used to remove the oxide from the InP surface involved quickly raising the substrate temperature to 395°C and holding it constant for approximately 40 minutes. The principle of this method is based on the congruent sublimation of InP. While working on the growth of InP, Farrow [10] reported the relationship between the P_2 and In evaporation flux signals and substrate temperature. Figure 6.3 shows the results with the congruent evaporation point (638 ± 10K) indicated. Farrow also reported that the maximum congruent

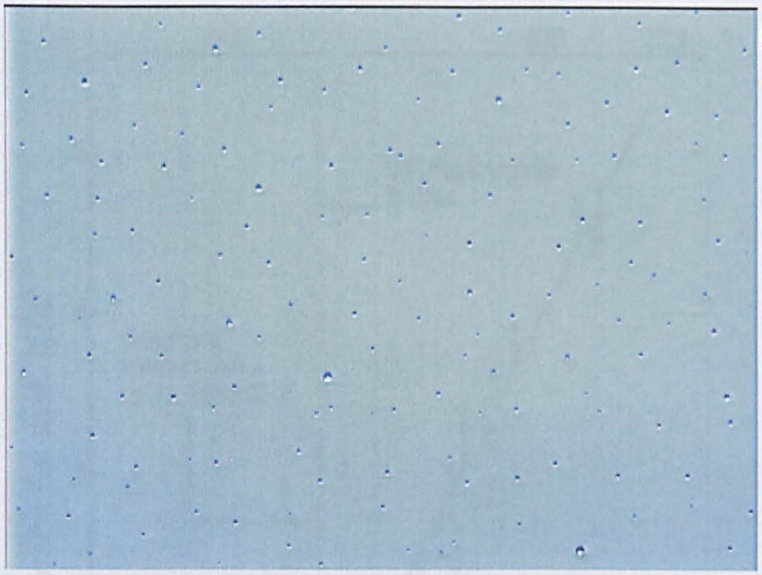

(a)

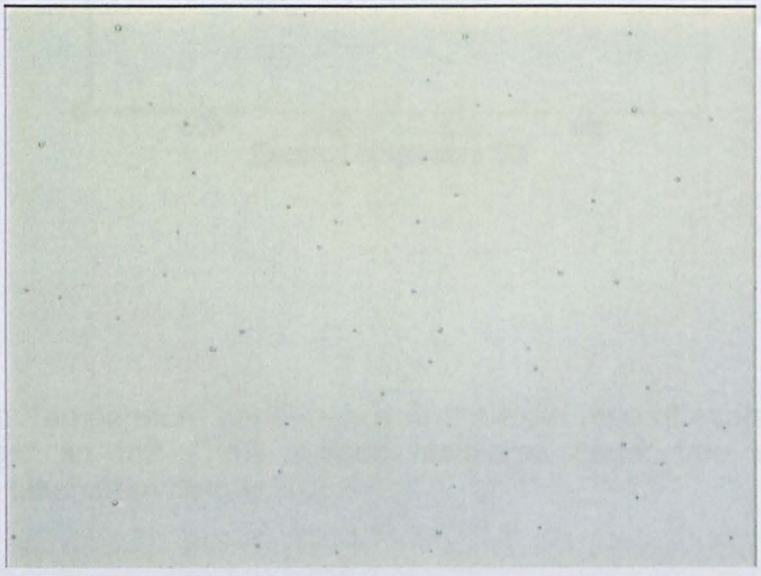

(b)

Figure 6.2: Images of InP surface, taken with an optical microscope, after oxide removal by heating substrate to (a) 510°C and (b) 490°C

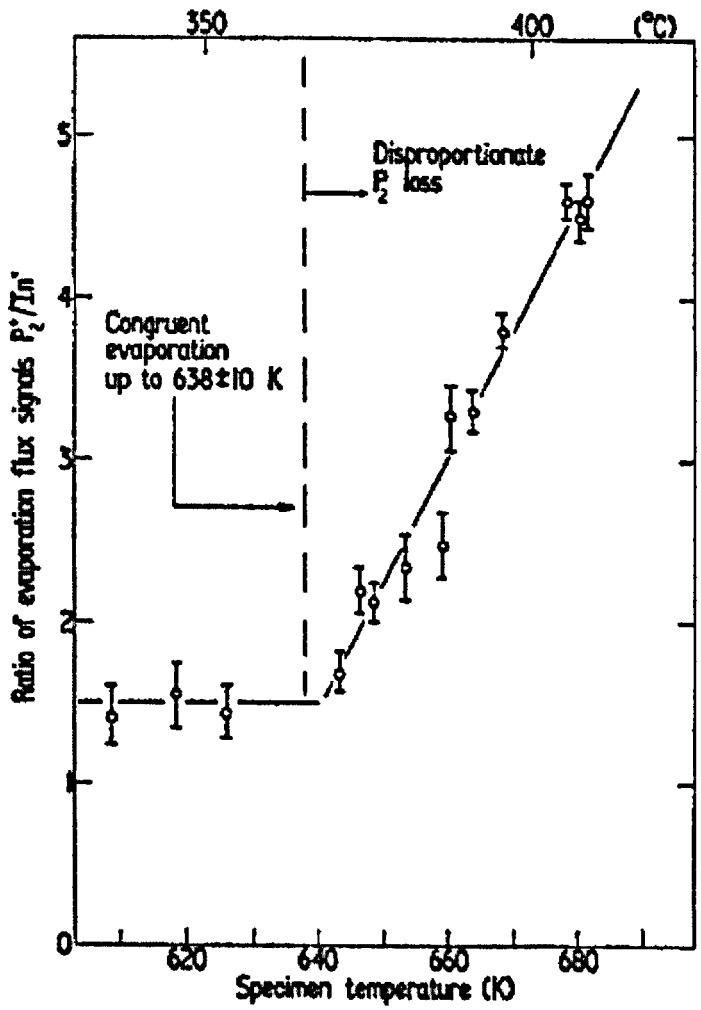

Figure 6.3: Temperature dependence of the P_2/In ratio of evaporation flux signals from an InP (100) surface measured under free evaporation conditions, taken from Farrow [10].

evaporation rate was 10^{-5} monolayers per second, suggesting that cleaning the InP by simply heating it to the congruent evaporation temperature would be inefficient.

It has since been demonstrated by Bando *et al.* [11] that InP substrate cleaning can be successfully carried out by maintaining a temperature of 380 ± 50°C for 15 minutes. The cleaning was carried out without any flux incident on the surface. The oxide removal was confirmed by X-ray Photoelectron Spectroscopy carried out in a UHV chamber connected to the MBE chamber. The temperature range used corresponds to the congruent evaporation temperature found by Farrow and therefore the oxide layer present on the surface of the InP is removed while still maintaining the congruent evaporation of the InP.

In the current work, the InP substrate was heated to 395°C while the surface was monitored by RHEED. After approximately 35 minutes the 4x reconstruction became visible. The power to the substrate heater was cut after 40 minutes and the substrate was cooled to the growth temperature with no flux incident on the surface.

Figure 6.4 is the image of the surface of InP observed with the optical microscope. The image was captured at the same magnification used for imaging the sample surface when cleaned by the first method. The edge of the sample was included only to show that the image was in focus; there are no visible In droplets present anywhere on the surface.

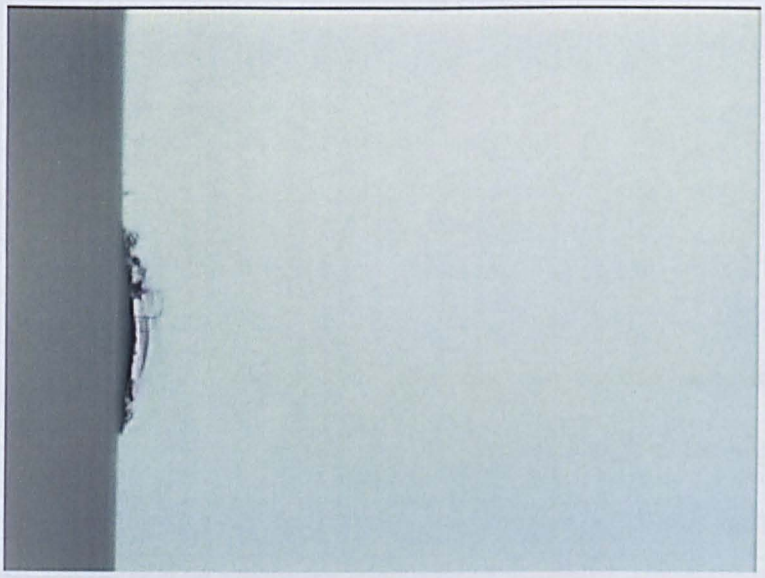

Figure 6.4: Optical microscope image of InP surface after oxide removal by heating substrate to 395°C for 40 minutes. Since no In droplets are visible the edge of the wafer has been imaged to confirm the surface is in focus.

Initial work on optimizing the growth of ZnCdSe on InP substrates was carried out with the InP cleaned by the first method described. Subsequent growths used the congruent sublimation method.

6.3 Growth of ZnCdSe buffer layer

Once the oxidised surface of the InP substrate was successfully removed, growth of the ZnCdSe buffer layer was started. The ZnCdSe layers were grown using 6N Zn, Cd and Se elemental sources. The fluxes from the Zn and Cd cells were varied until the ZnCdSe layer produced was lattice matched to the InP substrate. Figure 6.5 shows the 004 XRD scan of HWA1732, which comprises of a single layer of ZnCdSe. The cell temperatures used for the growth of this sample were T_{Zn}= 273°C, T_{Cd}= 183°C and T_{Se}= 172°C. The sample was grown using the first oxide removal technique and was cooled to growth temperature under a Zn flux. The XRD simulation indicates that the layer is a 10 nm layer of composition $Zn_{0.54}Cd_{0.46}Se$ at the substrate and a thicker layer of 340 nm with the composition $Zn_{0.47}Cd_{0.53}Se$. There is a thin layer of ZnCdSe with high Zn concentration because there was a build-up of Zn at the surface during the cooldown to the growth temperature.

The oxide removal of subsequent growths by this method were carried out with the Zn flux removed once the pyrometer temperature of the substrate cooled to 300°C, to prevent this build-up. It can be seen that the peak from the ZnCdSe layers is

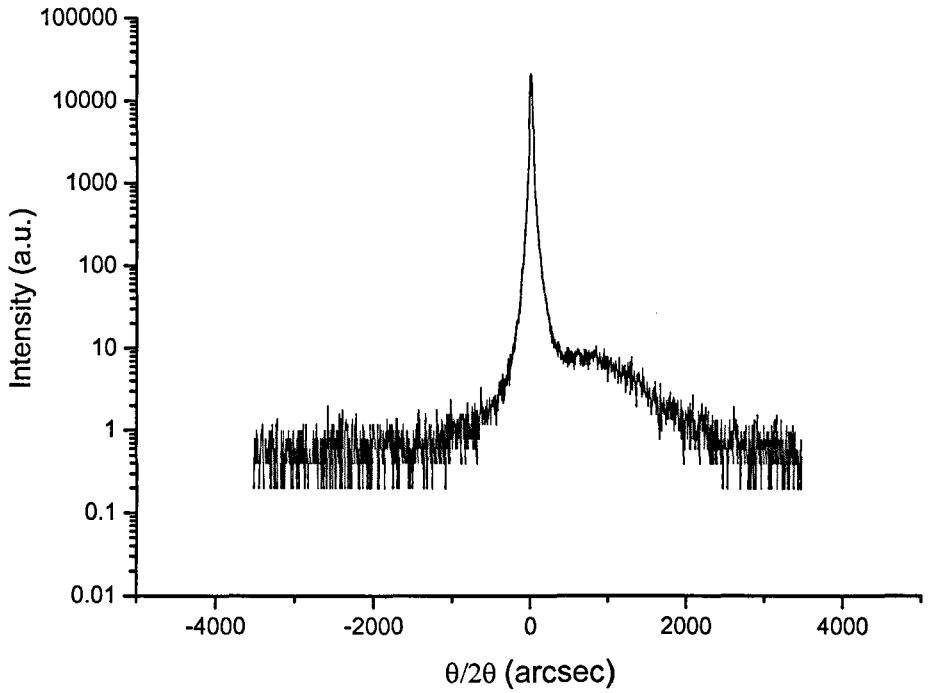

Figure 6.5: 004 XRD scan of HWA1732, a ZnCdSe layer grown for 90 minutes. The simulation software indicates that the sample is composed of two ZnCdSe layers, a thin layer nearest the substrate with a high Zn content and a second thicker layer of lattice matched composition.

within 1000 arcseconds of the substrate peak, indicating that the structure is sufficiently lattice matched to the substrate for growth of further structures.

6.4 CrS Growth on InP

The CrS layers were grown using a 6N compound ZnS source and a 5N elemental Cr source, which was further purified by the method described in Chapter 2. As there have been contamination problems with the other high temperature cells in the Heriot-Watt MBE system, which have been minimized through the installation of a LN_2 shutter, one was also fitted to the Cr cell. The use of LN_2 shutters on the ZnS and Mn cells has been discussed previously [Chapters 2 and 4 respectively]. Since the growths presented here are of initial layers and no definitive growth rate has been determined, the thicknesses of CrS layers will be described in reference to the growth times.

Sample for XRI were grown with the structure ZnCdSe / CrS / ZnCdSe, where the ZnCdSe layer were of equal thickness. Initially the Cr cell temperature was set at 1085°C, which was chosen because it gave an ion gauge current reading similar to that for the Mn cell for growth of MnS. A substrate thermocouple temperature of 285°C was used because that temperature gave a pyrometer reading of ~250°C, again similar to the successful growth of MnS. Figure 6.6a shows the 004 XRI scan of sample HWA1745, which was grown with these conditions and with a structure of ZnCdSe (78 nm) / CrS / ZnCdSe (78 nm). It can be seen from the figure that there are no interference fringes present in the scan.

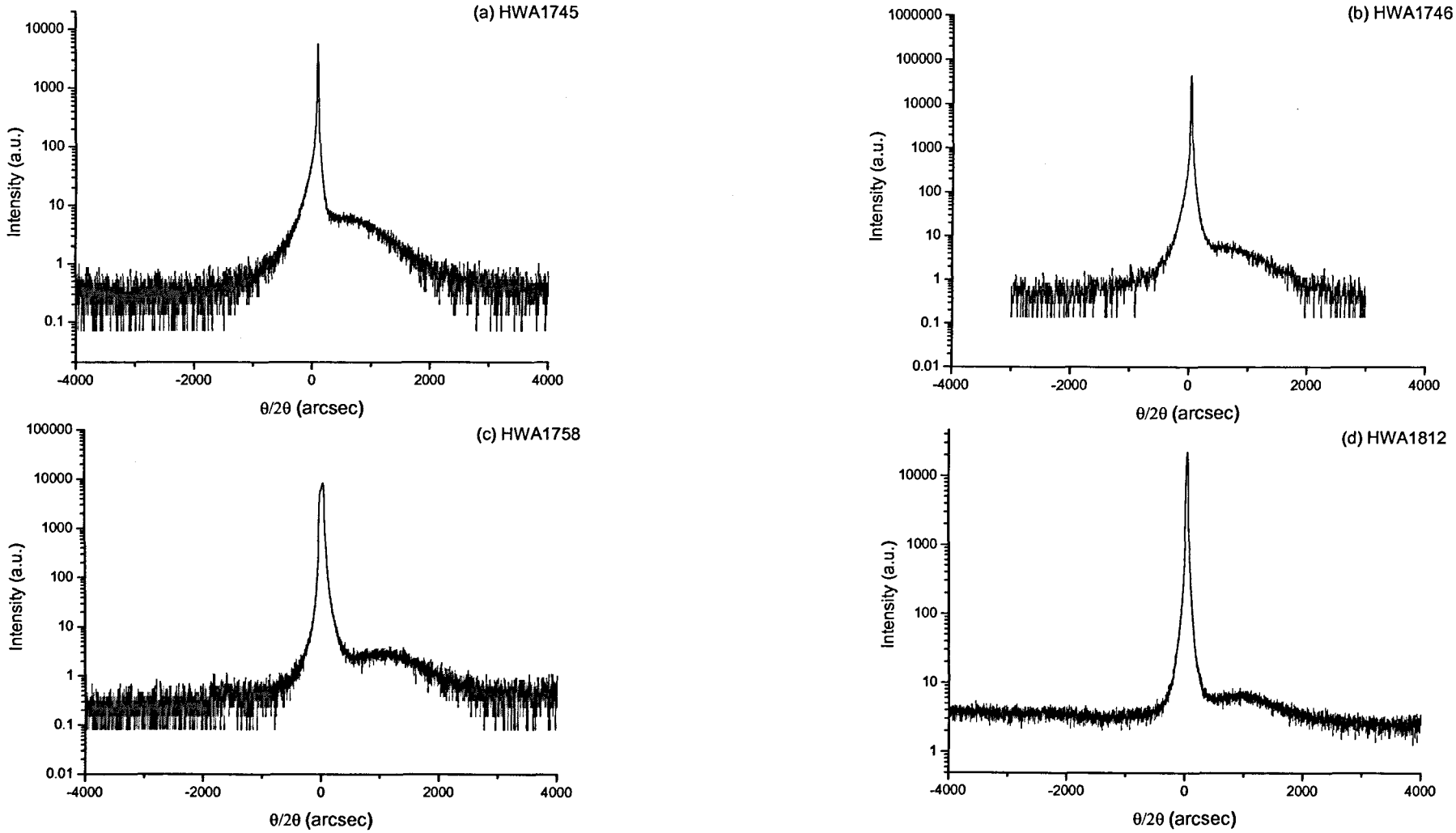

Figure 6.6: 004 XRI scans from ZnCdSe / CrS / ZnCdSe structures grown on InP substrates.

During subsequent growths, it was discovered that flux readings taken from the source cells while the Cr cell was above 1000°C showed poor run to run reproducibility. The flux readings were therefore not routinely taken. From examination of vapour pressure curves for Cr [12] it was decided that the temperature of the Cr cell was too low to produce a flux high enough to generate a significant thickness of CrS. Figure 6.6b shows the XRI scan from HWA1746, this sample is a repeat of HWA1745 except that the Cr cell temperature is 1100°C. The interference fringes are absent in this scan as well.

It was noted that when the Cr shutter was open, the pyrometer temperature reading from the substrate increased by ~30°C. Since the growth temperature window for MgS and MnS is 240 - 270°C [13], this increase puts the pyrometer temperature of the substrate during the CrS growth outside of this window at 290-295°C. This increase could be a real increase or reflected heat from the Cr source cell.

A similar temperature increase has been reported by Kobayashi *et al.* [14] while growing ZnMgCdS layers using a CdS compound source. A pyrometer temperature rise of more than 20K was observed when opening the shutter of the CdS cell, which was at a temperature of ~700°C with all the other cells and substrate kept at ~ 200 - 300°C. The temperature rise was compensated by using the irradiation from a heated filament. An empty K-cell was heated to produce the same heat flux as was being emitted by the CdS source. During the growth the shutter for the empty cell was opened whenever the CdS cell shutter was closed.

This process meant that the heat flux incident on the substrate and the substrate temperature was kept constant during the growth.

Since the temperature rise during the growth of CrS was larger than that reported by Kobayashi *et al.*, the use of a stabilizing heating source in the Heriot-Watt MBE system was considered. However there was no available port on the growth flange to house the empty K-cell.

For subsequent growths the substrate temperature was lowered to 235°C which reduced the pyrometer temperature during CrS growth to ~265°C. In an attempt to reduce the temperature during the CrS growth further, the buffer and cap layers were grown at a substrate thermocouple temperature of 235°C and then the temperature was lowered to 190°C for the CrS growth. This brought the pyrometer reading during the CrS growth to ~256°C.

Figure 6.6c shows the 004 XRI scan from sample HWA1758, which has the same structure as HWA1745 with the Cr source at 1130°C and the substrate temperature reduction discussed above. Since lowering the temperature during growth did not result in a significant drop in the pyrometer reading, subsequent growths were carried out at a constant substrate temperature of 235°C.

All previous growths of CrS on ZnCdSe were carried out on wafers that had the oxide layer removed by the first method discussed in section 6.2. Figure 6.6d shows the XRI scan of HWA1812. This sample was grown after the wafer was heat cleaned using the congruent sublimation of InP, the second method discussed in

section 6.2. This Cr cell temperature used was 1160°C and the substrate temperature was kept constant at 235°C. The structure of the sample is the same as HWA1745, with the same cell temperatures used except for the Cr cell. From the figure, it can be seen that there is only a small peak from the ZnCdSe layers visible on the scan.

The lack of well defined Pendellösung fringes indicated that a strained structure was not produced. At this point, it was decided to re-examine the lattice parameter to see if ZB CrS was indeed lattice matched for growth on InP. The following section details how the lattice parameter of CrS was determined from layers of MnCrS and recalculation using published atomic radii.

6.5 Growth and X-ray Characterisation of MnCrS

As discussed previously, at the start of this work there was ambiguity in the value of the lattice parameter of CrS, with values ranging from 5.04 [4] to 5.806 Å. Growth of ZB CrS was initially attempted on InP substrates, which are lattice matched for the estimate of 5.806 Å of the lattice parameter of CrS. However if the theoretical value of 5.309 Å [5] or any smaller value is more accurate then CrS cannot be grown on InP and another substrate must be found. In order to determine a more suitable substrate, the lattice parameter of ZB CrS must be accurately calculated.

A series of MnCrS layers were grown for XRI analysis. The XRI technique has been described previously in Chapter 3 and results from MnS layers are discussed in Chapter 4. All the samples were grown with the structure GaAs (sub) / ZnSe (~48 nm) / MnCrS / ZnSe (~48 nm).

Initially the Cr cell temperature was set at 1100°C (HWA1815), however the XRI scan of this sample (Figure 6.7) did not show any resolvable Pendellösung fringes. The temperature of the Cr cell was then lowered until fringes were observed in the XRI scan. A series of samples were produced with the Cr cell temperature at 1020, 1010 and 1000°C for XRI analysis.

Figure 6.8a shows the 004 scan from sample HWA1850, grown with a Cr temperature of 1010°C. As previously stated, the RADS Mercury X-ray simulation software requires a value for the lattice parameter of CrS to be entered into the program in order to calculate the Cr mole fraction in the layer. Initially the simulation was calculated using the value a_{CrS} = 5.806 Å, however a suitable fit to the data was not achieved. The lattice parameter was then changed to a value of 5.487 Å, after the calculation using atomic radii was carried out (see section 6.6). Figure 6.8b shows the 004 XRI scan and simulation using a_{CrS} = 5.487 Å of sample HWA1850. By manually altering a_{CrS} in 0.05 Å steps and re-iterating the simulation a better fit to the data was achieved. For a_{CrS} = 5.387 ± 0.025 Å, it can be seen in Figure 6.8c that the simulation and data fit well.

Figures 6.9a and b show the 004 scans and simulations of HWA1843 and HWA1854 respectively. The results from these simulations are detailed in Table

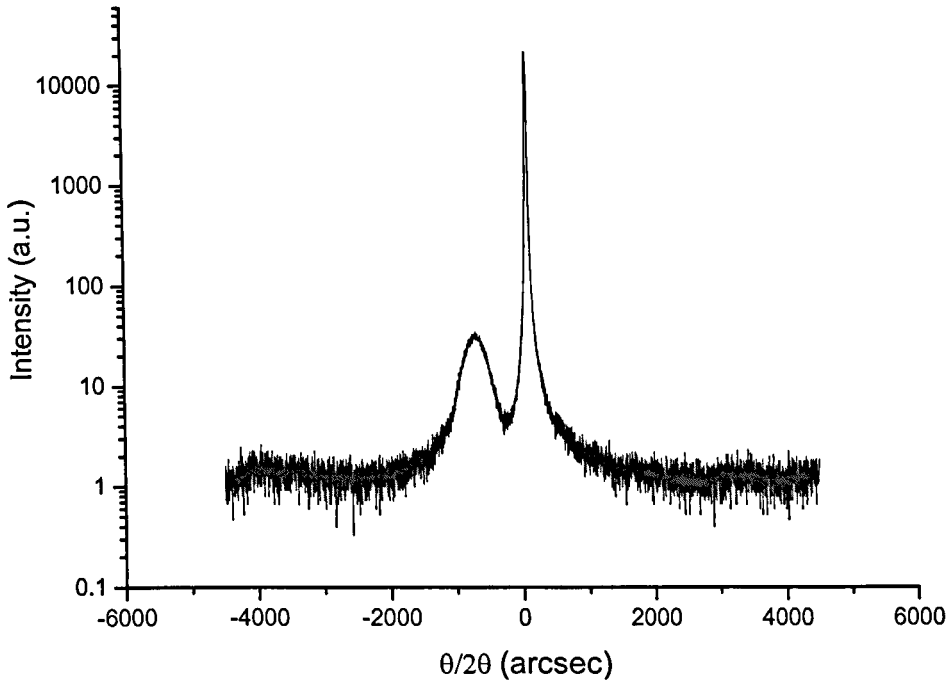

Figure 6.7: XRI scan of sample HWA1815, with structure GaAs (sub) / ZnSe (48 nm) / MnCrS / ZnSe (48 nm). The MnCrS layer was grown with T_{Cr} = 1100°C.

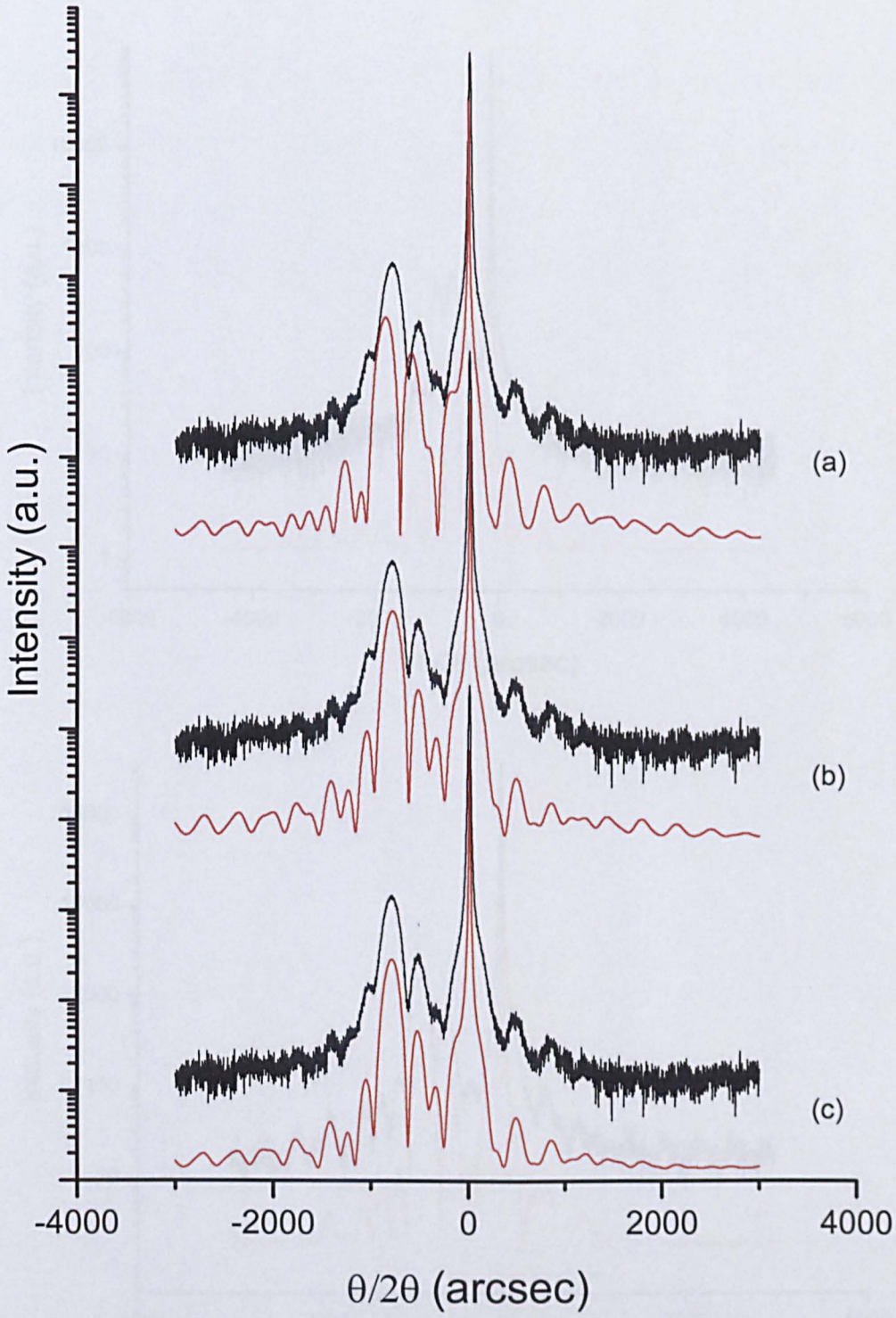

Figure 6.8: XRI scan and simulation data (in red) from sample HWA1850 with the structure GaAs (sub) / ZnSe (48 nm) / MnCrS / ZnSe (48 nm). The MnCrS layer was grown with T_{Cr} = 1010°C. Simulation labelled (a) was calculated using a_{CrS} = 5.806 Å, (b) using 5.487 Å and (c) using 5.387 Å.

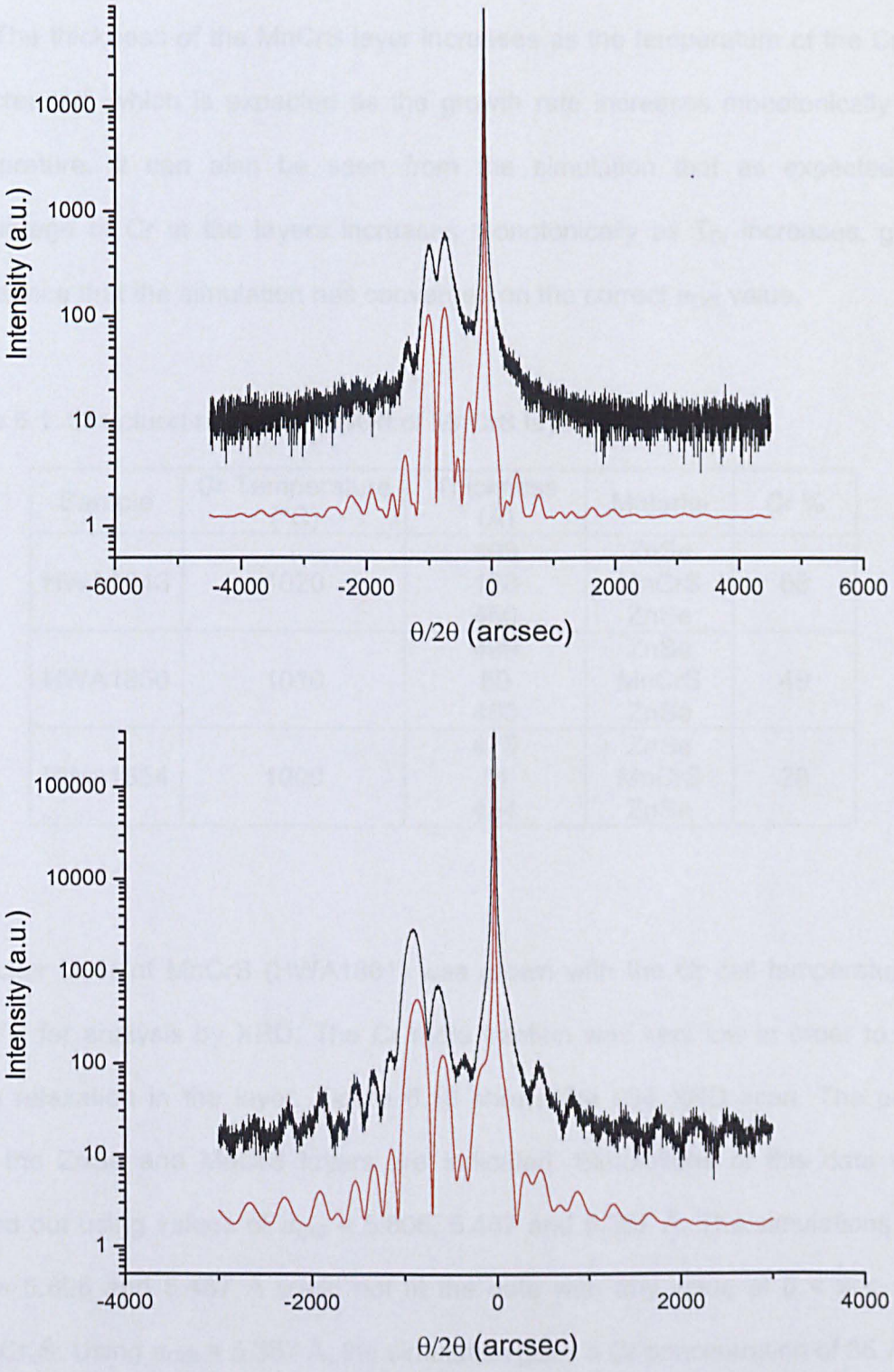

Figure 6.9: XRI scan and simulation data (in red) from sample HWA1843 (top) and HWA1854 (bottom) both with the structure GaAs (sub) / ZnSe (48 nm) / MnCrS / ZnSe (48 nm). The MnCrS layers were grown with T_{Cr} = 1020°C and 1000°C. The simulation curves were calculated using a_{CrS} = 5.387 Å.

6.1. The thickness of the MnCrS layer increases as the temperature of the Cr cell is increased, which is expected as the growth rate increases monotonically with temperature. It can also be seen from the simulation that as expected the percentage of Cr in the layers increases monotonically as T_{Cr} increases, giving confidence that the simulation has converged on the correct a_{CrS} value.

Table 6.1: Structural results from XRI of MnCrS layers.

Sample	Cr Temperature (°C)	Thickness (Å)	Material	Cr %
HWA1843	1020	499 138 450	ZnSe MnCrS ZnSe	68
HWA1850	1010	499 59 450	ZnSe MnCrS ZnSe	49
HWA1854	1000	475 51 454	ZnSe MnCrS ZnSe	28

A thicker layer of MnCrS (HWA1861) was grown with the Cr cell temperature at 1000°C for analysis by XRD. The Cr mole fraction was kept low in order to stop strain relaxation in the layer. Figure 6.10 shows the 004 XRD scan. The peaks from the ZnSe and MnCrS layers are indicated. Simulations of this data were carried out using values of a_{CrS} = 5.806, 5.487 and 5.387 Å. The simulations with a_{CrS} = 5.806 and 5.487 Å could not fit the data with any value of $0 < x < 1$ for $Mn_{1-x}Cr_xS$. Using a_{CrS} = 5.387 Å, the simulation gave a Cr concentration of 35.7 %.

From these growths and the analysis, it can be seen that the lattice parameter of ZB CrS is not 5.806 Å and therefore not lattice matched for growth on InP as a

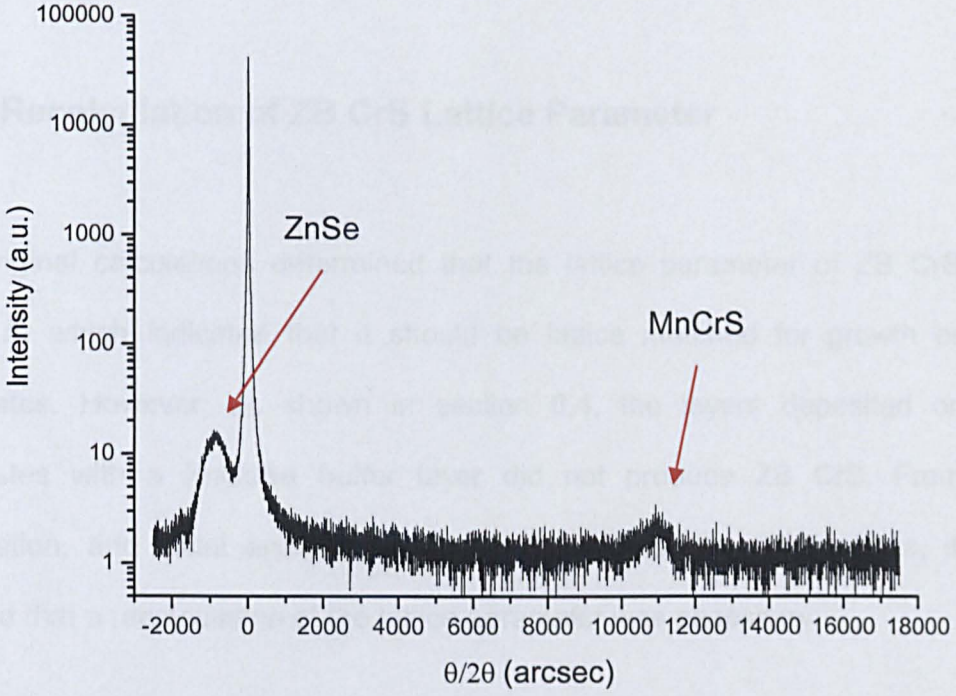

Figure 6.10: 004 XRD scan of HWA1861, a 61 nm thick layer of MnCrS grown with T_{Cr} = 1000°C.

substrate. The lattice parameter for ZB CrS is, from the XRI and XRD scans, 5.387 ± 0.025 Å. This value means that layers of CrS should be lattice matched to GaP. The next section outlines the atomic radii calculation used in the XRI simulations here and the growth of CrS on GaP substrates.

6.6 Recalculation of ZB CrS Lattice Parameter

The original calculations determined that the lattice parameter of ZB CrS was 5.806 Å, which indicated that it should be lattice matched for growth on InP substrates. However, as shown in section 6.4, the layers deposited on InP substrates with a ZnCdSe buffer layer did not produce ZB CrS. From this information, and initial analysis of the MnCrS layers discussed above, it was decided that a recalculation of the lattice parameter was necessary.

The lattice parameter of a ZB compound can be calculated from the radii of the atoms involved and their positions in the unit cell. In the zinc blende unit cell there is a metal atom at co-ordinates (0, 0, 0) and a non-metal atom at (¼, ¼, ¼). Since the ZB structure is cubic, the position of the non-metal atom can be written as $\left(\frac{a}{4},\frac{a}{4},\frac{a}{4}\right)$, where a is the lattice parameter of ZB compound. From Figure 6.11, y equals the sum of the radii of the two atoms in the unit cell, $r_m + r_n$. Using Pythagoras theorem, y can also be calculated as follows:

$$y = \sqrt{x^2 + \left(\frac{a}{4}\right)^2} \qquad x^2 = \left(\frac{a}{4}\right)^2 + \left(\frac{a}{4}\right)^2 \qquad \text{Equation 6.1}$$

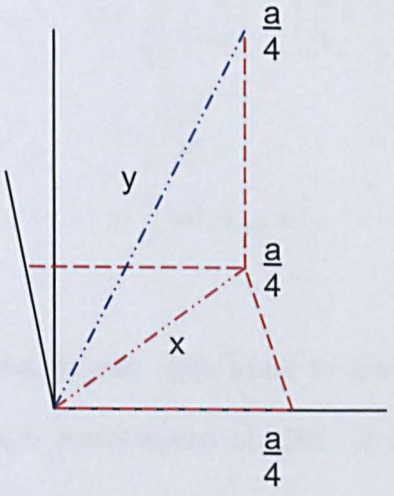

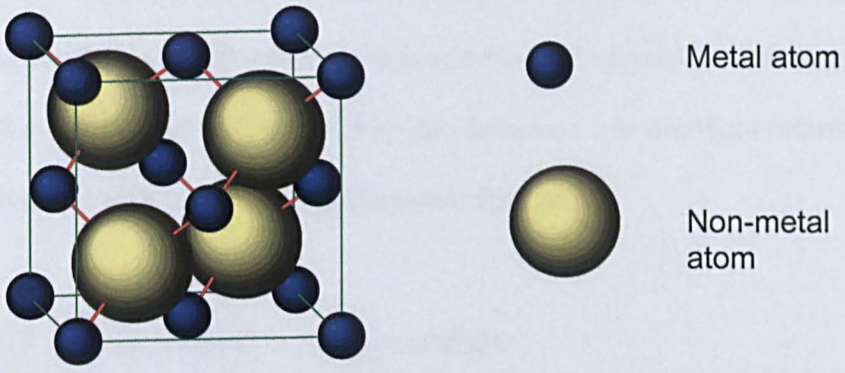

Figure 6.11: Schematic of zinc blende unit cell depicting the origins of the equation $\frac{a}{4}\sqrt{3} = r_m + r_n$ used to calculate the lattice parameter of the compound.

Therefore

$$y = \sqrt{\left[\sqrt{\left(\frac{a}{4}\right)^2 + \left(\frac{a}{4}\right)^2}\right]^2 + \left(\frac{a}{4}\right)^2} \qquad \text{Equation 6.2}$$

$$= \sqrt{\frac{3a^2}{16}}$$

$$= \frac{a}{4}\sqrt{3} = r_m + r_n \qquad \text{Equation 6.3}$$

Table 6.2 shows the atomic radii used in the above calculation as well as the results for the lattice parameters of CrS, MnS and ZnS, for comparison. The different radii are defined as follows: the Empirical Radii have been derived by careful comparison of the bond lengths in over 1200 bond types [15]; the methods outlined in Clementi *et al* [16] have been used to calculate the Calculated Radii; the Atom-Atom Bond Length refers to the internuclear separation between the atoms in the element; one half of the bond length between two identical atoms bonded by a single bond is referred to as the Covalent Radius.

Table 6.2: Atomic Radii of S, Cr, Mn and Zn.

Atomic Radii (taken from ref [6])	r_S (Å)	r_{Cr} (Å)	r_{Mn} (Å)	r_{Zn} (Å)
Empirical Radius	1.0	1.4	1.4	1.35
Calculated Radius	0.88	1.66	1.61	1.42
Atom-Atom Bond Length	1.025	1.249	1.366	1.3325
Covalent Radius	1.02	1.27	1.39	1.31

Table 6.3: Calculated Lattice Parameters of CrS, MnS and ZnS.

Lattice Parameter calculated from	a_{CrS} (Å)	a_{MnS} (Å)	a_{ZnS} (Å)
Empirical Radius	5.542	5.542	5.427
Calculated Radius	5.866	5.7504	5.312
Atom-Atom Bond Length	5.2516	5.5206	5.444
Covalent Radius	5.2885	5.5657	5.3809
Mean value of Lattice Parameter	5.487	5.595	5.390

In Table 6.3, the lattice parameters of MnS and ZnS have also been calculated. The accepted values for these compounds are a_{MnS} = 5.559 Å [13] and a_{ZnS} = 5.41 Å [17], and they agree with those calculated above to within approximately 1%. Therefore the result determined for a_{CrS} can be considered to be accurate to within the same margin. This calculation as well as the XRI analysis carried out on MnCrS layers indicates that ZB CrS is lattice matched to GaP substrates.

There are a number of reasons why the value initially determined by K. Prior for a_{CrS} is incorrect. Firstly, the values he used for the atomic radii of the transition metals were taken from the crystallographic software, CaRIne, which contains a non-standard data set that can be edited easily by the user. Second, the empirical scaling factor used to correct the lattice parameters was determined by comparing the calculated lattice parameter of MnS with that determined by XRD at Heriot-Watt, however the experimental value used was 5.615 Å not the value determined in the present work of 5.559 Å. Re-calculating the lattice parameters with the correct scaling factor does not rectify the problem, which implies that the radii taken from CaRIne were incorrect. One final thing to note about the initial lattice parameter calculation is that the lattice parameter of ZnS was incorrect both before

and after the scaling factor had been applied, and scaling the results with respect to the ZnS lattice parameter gives the incorrect result of 5.536 Å of the lattice parameter of MnS. This implies that the use of an empirical scaling factor may not have been the most effective solution in this case.

6.8 Growth of CrS on GaP

The CrS layers presented in this section were grown on (100) GaP wafers from University Wafer. The 2 inch substrates were cleaved into eighths prior to growth and etched in a 15:5:5 solution of $HCl:HNO_3:H_2O$ [18] for 120 seconds at room temperature. The sample was then rinsed in 18MΩ deionised water and dried quickly with dry nitrogen. Once mounted on the molybdenum substrate holder with indium, the sample was transferred into the MBE system. Rapid heating to 200°C for 5 minutes in the preparation chamber, removed any adsorbed water before the sample is transported into the growth chamber.

The oxide removal process for GaP involves heating the substrate to between 580 and 630°C while the sample is exposed to a zinc flux. During this process the 4x RHEED reconstruction is observed, indicating the removal of the oxide layer. The sample is then cooled to ~170°C for growth of the ZnS buffer layer. The Zn flux was removed when the temperature of the substrate reached ~200°C to prevent Zn condensing on the surface.

Previously at Heriot-Watt a comparison of three different growth methods using different source materials was made [18,19]. The first method used elemental zinc and sulphur from a cracker cell, while the second used a compound ZnS source and sulphur from a cracker cell and the final method used only the ZnS source. PL carried out on these samples show that when using only the ZnS source good quality ZnS layers were produced. Since the active MBE chamber at Heriot-Watt does not have a cracker cell and high quality material has been produced using only a ZnS source, this method of ZnS growth was used.

The ZnS layers produced in this study were structurally characterised by XRD. Figure 6.12 shows the 004 XRD scan of HWA1890, a layer of ZnS grown for 30 minutes, which was measured, by optical interference, to be 650 nm thick.

Figure 6.13 shows the XRI scan from sample HWA1900, a 31 second CrS layer sandwiched in between two layers of ZnS both ~ 150 nm thick. The temperatures used for the growth of the CrS layer were 1020°C for the Cr cell and the substrate thermocouple temperature was raised to 330°C for the growth of the thin layer. This was the temperature at which the MnCrS samples were successfully grown. The different substrate temperatures used for the layers meant that the growth had to be halted between layers while the temperature was altered to the desired point. The time to heat to the CrS growth temperature for these structures was 25 minutes and the cooling time back to the ZnS growth temperature was 50 minutes.

It can be seen that there is only one peak present in Figure 6.13 other than the substrate peak. It was initially believed that this was because there was not enough

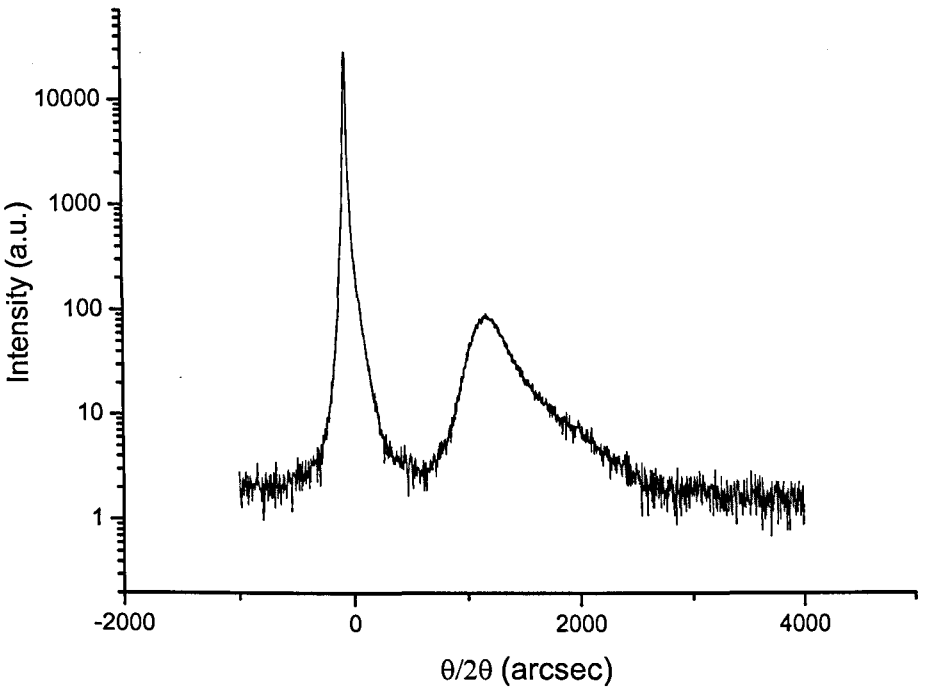

Figure 6.12: 004 XRD scan of HWA1890, a 650 nm thick layer of ZnS.

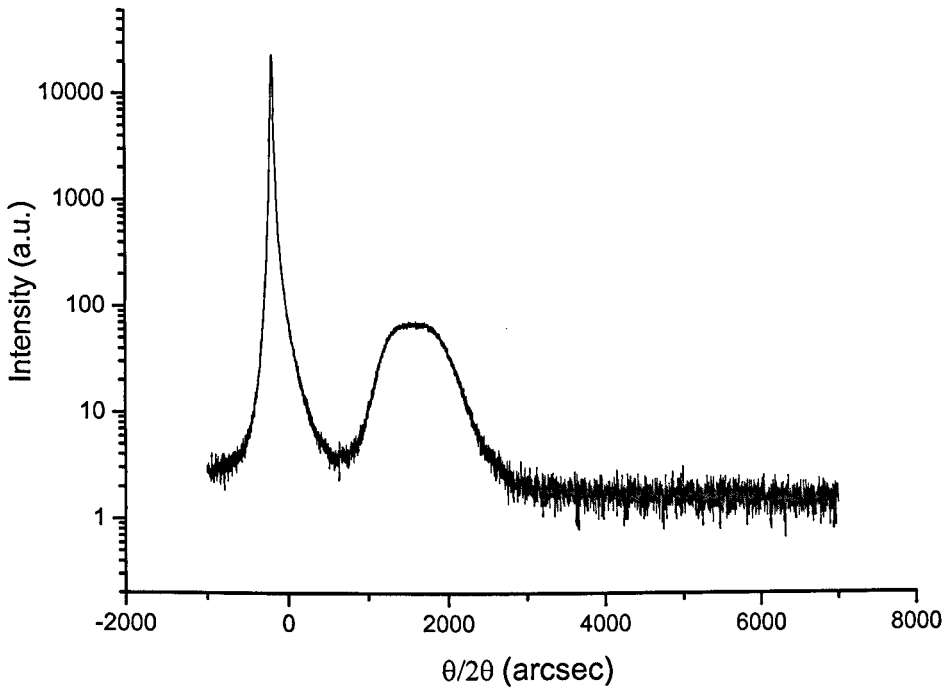

Figure 6.13: 004 XRI scan of HWA1900, with a structure ZnS (~150 nm) / CrS / ZnS (~150 nm). The Cr cell temperature for this growth was 1020°C.

Cr incident on the sample to produce a continuous layer of CrS and therefore only ZnS layers were grown. Subsequent growths were carried out with the Cr temperature increased. There was no change in the XRI scans even up to Cr cell temperatures as high as 1230°C, as shown in Figure 6.14, the XRI scan from sample HWA1913. This sample has the structure GaP (sub) / ZnS (~100 nm) / CrS (60 s) / ZnS (~100 nm).

Further examination of the XRI scan from HWA1900 (Figure 6.13) indicated that the structure peak consists of two superimposed peaks. Since there was no significant change in the data from structures when the Cr temperature was increased, it is possible that a_{CrS} could be similar to a_{ZnS}. From Prior *et al.* [20], the phase change in the XRI experiment for each plane is

$$\delta\varphi = 2\pi m^* \qquad \text{Equation 6.4}$$

where $\delta\varphi$ is the phase change and m^* is the lattice parameter mismatch between the spacer and cladding layers. So for N planes:

$$\delta\varphi = 2\pi N m^* \qquad \text{Equation 6.5}$$

The thickness of the spacer layer, t can be expressed as the product of the number of planes and the repeat thickness of the diffraction pattern which equals a quarter of the lattice parameter of the cladding layers, d_{hkl} :

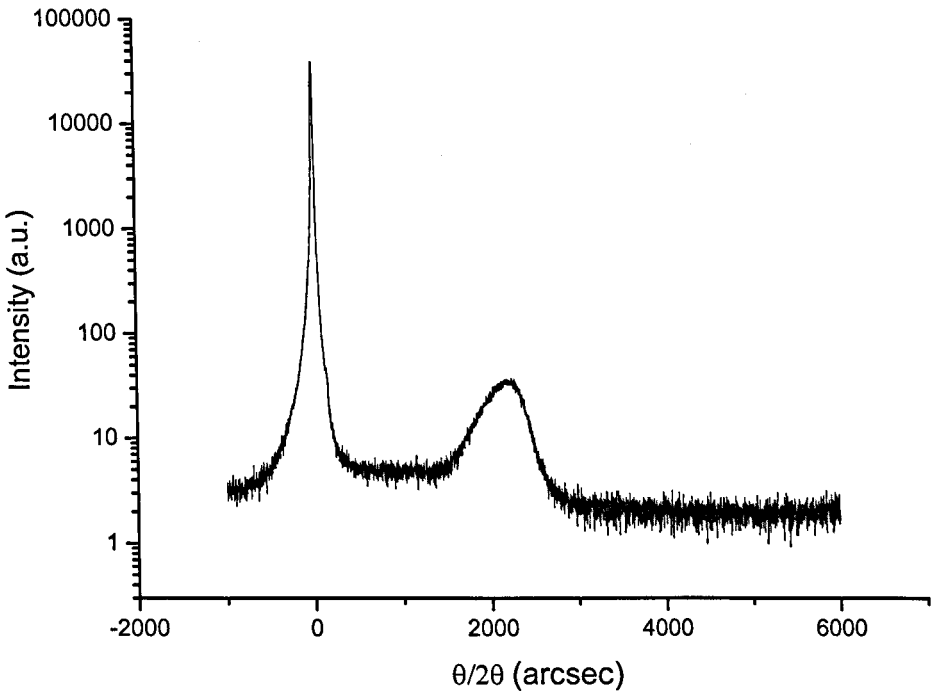

Figure 6.14: 004 XRI scan of HWA1913, with a structure ZnS (~100 nm) / CrS / ZnS (~100 nm). The Cr cell temperature for this growth was 1230°C.

$$t = d_{hkl}N = \frac{a}{4}N \qquad \text{Equation 6.6}$$

Combining Equations 6.5 and 6.6 gives:

$$\delta\varphi = 8\pi\frac{t}{a}m^* \qquad \text{Equation 6.7}$$

The criteria detailed by Holloway [21], suggests that the smallest difference in layer thickness between similar XRI scans that can be resolved corresponds to a phase change of $\pi/16$. Therefore Equation 6.7 becomes:

$$m^* \geq \frac{1}{128}\frac{a}{t} \qquad \text{Equation 6.8}$$

The lattice mismatch between ZnS and CrS is 4.25 x10^{-3}, assuming a_{CrS} = 5.387 Å. Therefore, from Equation 6.8, if the thickness of the spacer layer is less than 1 nm then no Pendellösung fringes will be visible in the XRI scan. As can be seen in the following pages, the thickness of the CrS layers in this series of samples can be extrapolated as being less then 10 nm, so therefore may have the effect described above.

In order to solve this problem, the lattice constant of the cladding layers can be changed. Therefore, the CrS layers were subsequently grown on layers of ZnMgS, lattice matched to GaP. These growths were carried out before a full analysis of the MnCrS XRI data could be completed, therefore the lattice parameter of CrS had still not been accurately determined.

Figure 6.15 shows the 004 XRI scans of samples HWA1915, HWA1916 and HWA1917, which were all growth with the same structure, ZnMgS (~95 nm) / CrS / ZnMgS (~95 nm). The Cr cell was kept constant during these growths and the temperature used for the Mg cell was initially determined from previous work on the growth of ZnMgS [19], then altered to produce a ZnMgS layer more closely lattice matched to GaP, which resulted in temperatures of 337, 350 and 353°C for HWA1915, HWA1916 and HWA1917 respectively.

It can be seen from Figure 6.15 that as the Mg cell temperature is increased the separation between the substrate peak and the cladding layer peak decreases, this indicates that the ZnMgS layer is more closely lattice matched to the substrate in sample HWA1917.

Further growths of samples with the same structure were carried out while varying the Cr cell temperature. It was noted that at a Cr cell temperature of 1010°C, the RHEED pattern remained streaky throughout the 30 second CrS growth, at other temperatures the pattern became spotty after 15-25 seconds. During the growth of MgS and MnS, the streaky RHEED pattern was used as an indication of the quality of the growth [22]. A series of samples were then grown for XRI analysis with T_{Cr} = 1010°C and T_{Mg} = 353°C, with the structure ZnMgS (~95 nm) / CrS (X seconds) / ZnMgS (~95 nm) where X = 30, 20 and 10 seconds for HWA1918, HWA1922 and HWA1923 respectively.

Figure 6.16 shows the 004 scans from the series. The scan from HWA1918 shows that the structure peak is ~ 200 arcsec further away from the substrate peak than

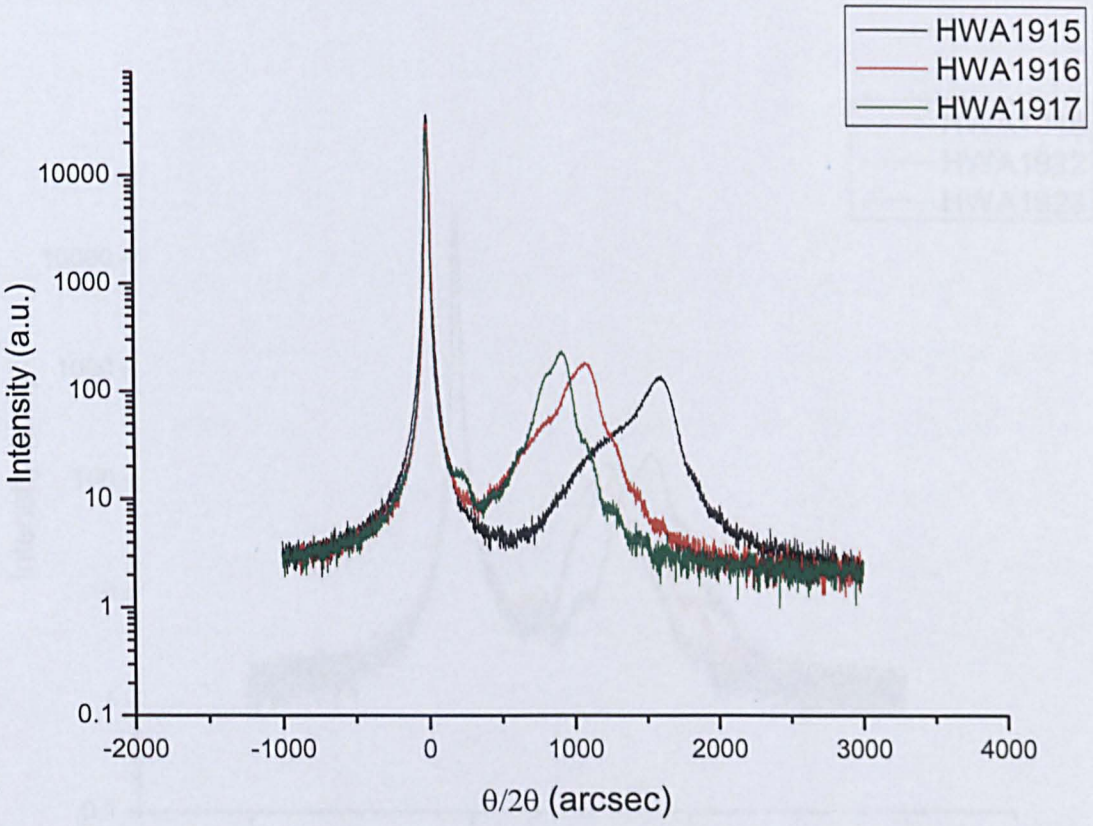

Figure 6.15: 004 XRI scans of samples HWA1915, 1916 and 1917. The samples all have a similar structure, ZnMgS / CrS / ZnMgS. The Cr cell temperature for these growths was kept constant at 1020°C. The Mg cell temperature varied for the three samples with HWA1915 at 337°C, HWA1916 at 350°C and HWA1917 at 353°C.

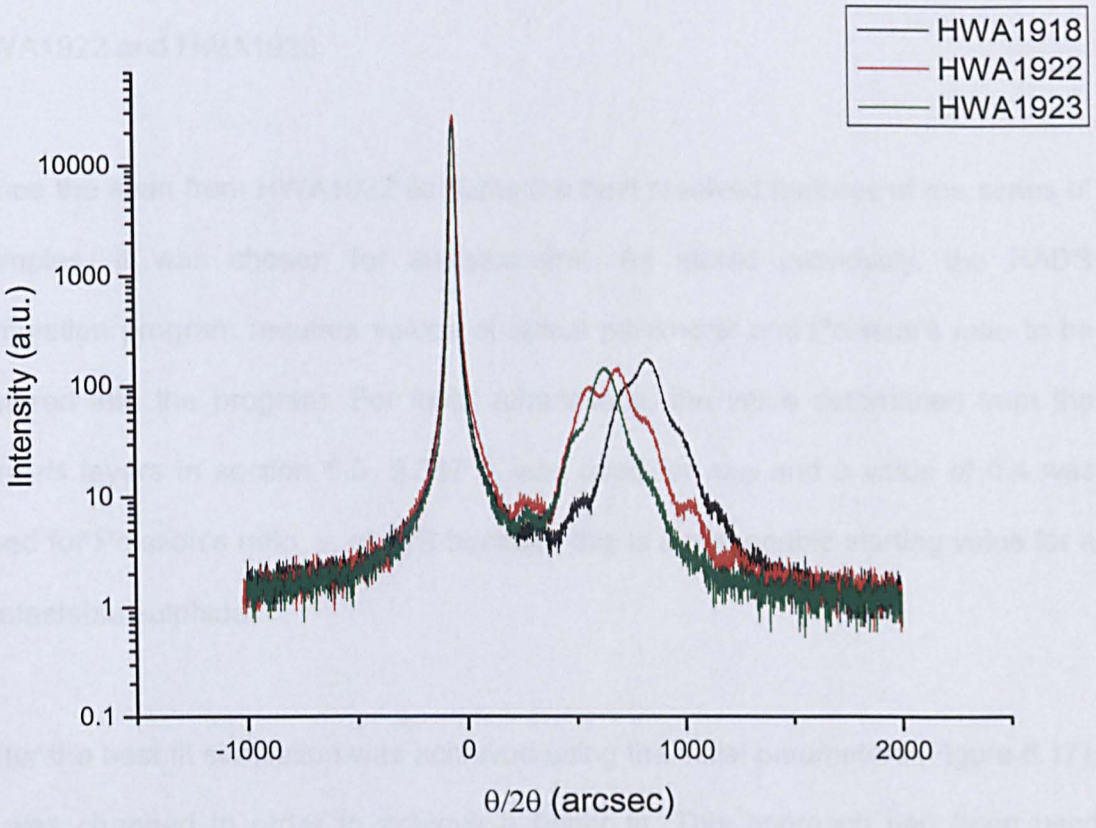

Figure 6.16: 004 XRI scans of samples HWA1918, 1922 and 1923. The samples all have a similar structure, ZnMgS / CrS / ZnMgS, with varying thickness of CrS. The Cr and Mg cell temperatures for these growths were kept constant at 1010°C and 353°C respectively.

in the other two scans in the series. This is due to an increased amount of Zn in the lower cladding layer. During cooldown after the oxide desorption of the substrate, the Zn flux was incident on the surface for a longer period of time than for the other samples in the series. For this reason the main analysis was carried out on HWA1922 and HWA1923.

Since the scan from HWA1922 contains the best resolved features of the series of samples, it was chosen for analysis first. As stated previously, the RADS simulation program requires values of lattice parameter and Poisson's ratio to be entered into the program. For initial simulations, the value determined from the MnCrS layers in section 6.5, 5.387 Å was used for a_{CrS} and a value of 0.4 was used for Poisson's ratio, v, of CrS because this is a reasonable starting value for a metastable sulphide.

After the best fit simulation was achieved using the initial parameters (Figure 6.17), v was changed in order to achieve a better fit. This approach had been used previously during the fitting of MgS and MnS XRI layers [23,24]. Therefore, v was varied in steps of 0.025 and as the value of v was increased the simulation fit to the data improved. The best fit was achieved using v = 0.485, which is consistent with the values for the other metastable sulphides. The lattice parameter of CrS was then altered to determine if the fit could be further improved. It was found that the best fit to the data was achieved when a_{CrS} = 5.3525 ± 0.0025 Å. Another cycle of varying v gave another slight improvement with a final value of 0.48 ± 0.02.

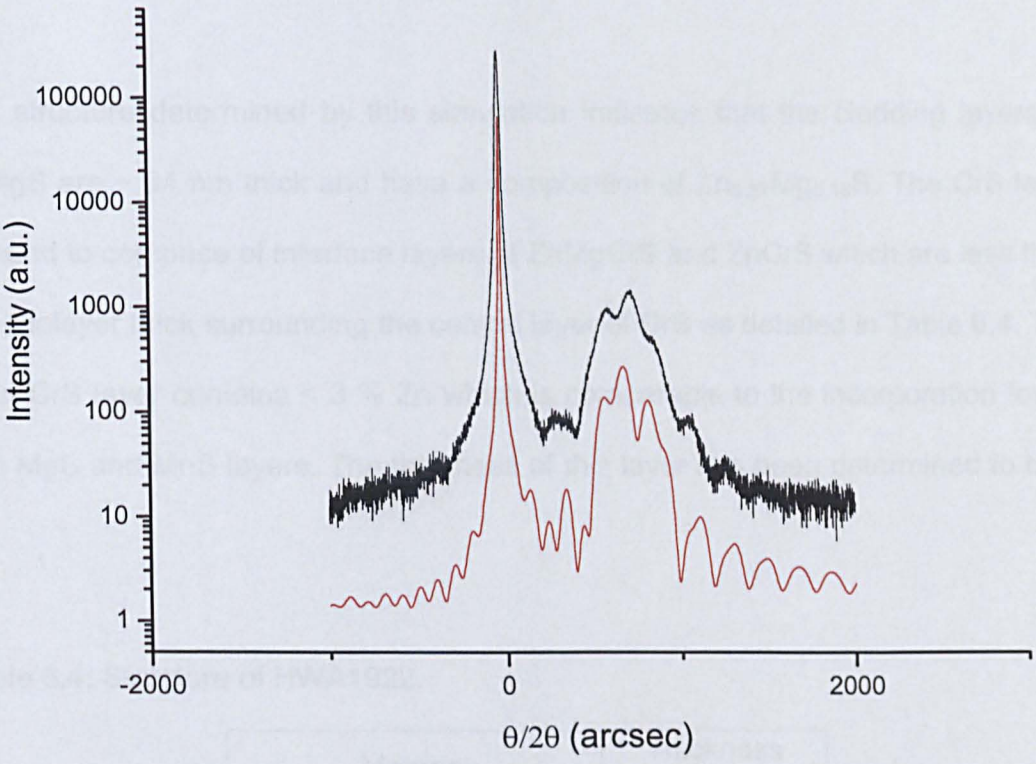

Figure 6.17: 004 XRI scan of HWA1922 and the corresponding simulation using $v = 0.4$ and $a_{CrS} = 5.387$ Å.

Figure 6.18a shows the best fit simulation for the 004 XRI scan of HWA1922 and corresponding simulation. The simulation was calculated using the best fit values and when compared to Figure 6.17, it can be seen that the simulation fit is excellent.

The structure determined by this simulation indicates that the cladding layers of ZnMgS are ~ 94 nm thick and have a composition of $Zn_{0.87}Mg_{0.13}S$. The CrS layer is found to comprise of interface layers of ZnMgCrS and ZnCrS which are less than a monolayer thick surrounding the central layer of CrS as detailed in Table 6.4. The main CrS layer contains < 3 % Zn which is comparable to the incorporation found with MgS and MnS layers. The thickness of this layer has been determined to be 3 nm.

Table 6.4: Structure of HWA1922.

Material	Thickness (nm)
$Zn_{0.87}Mg_{0.13}S$	96
$Zn_{0.86}Mg_{0.08}Cr_{0.06}S$	0.18
$Zn_{0.82}Cr_{0.18}S$	0.1
$Zn_{0.03}Cr_{0.97}S$	3
$Zn_{0.78}Cr_{0.22}S$	0.06
$Zn_{0.87}Mg_{0.04}Cr_{0.09}S$	0.01
$Zn_{0.86}Mg_{0.14}S$	93
GaP	Sub

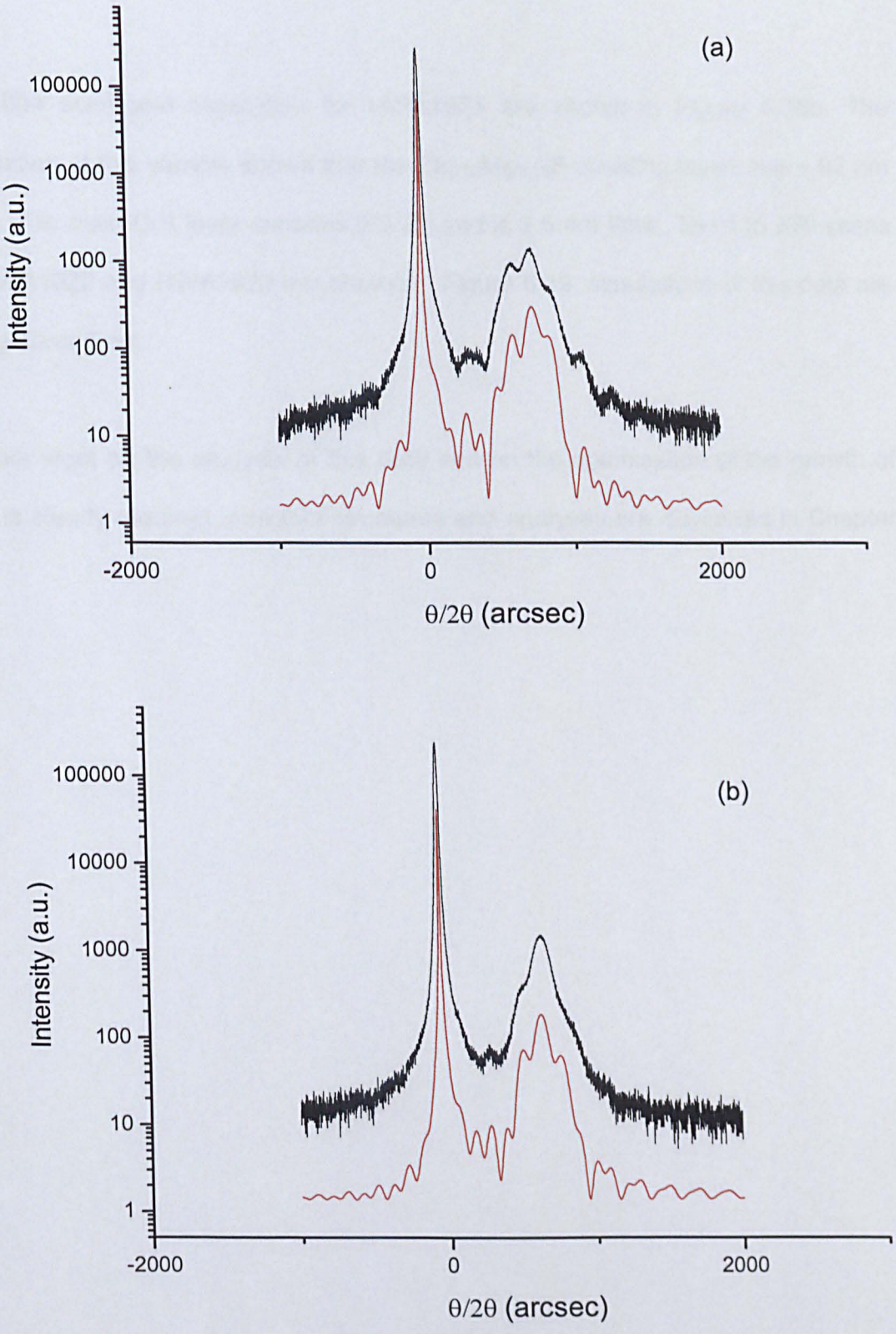

Figure 6.18: 004 XRI scans and corresponding simulations using v = 0.46 and a_{CrS} = 5.3525 Å of (a) HWA1922 and (b) HWA1923.

The 004 scan and simulation for HWA1923 are shown in Figure 6.18b. The simulation of this sample shows that the $Zn_{0.87}Mg_{0.13}S$ cladding layers are ~ 92 nm thick. The main CrS layer contains 2% Zn and is 2.5 nm thick. The 115 XRI scans of HWA1922 and HWA1923 are shown in Figure 6.19, simulations of this data are being carried out.

Further work on the analysis of this data and on the optimisation of the growth of CrS is clearly required, possible structures and analyses are discussed in Chapter 7.

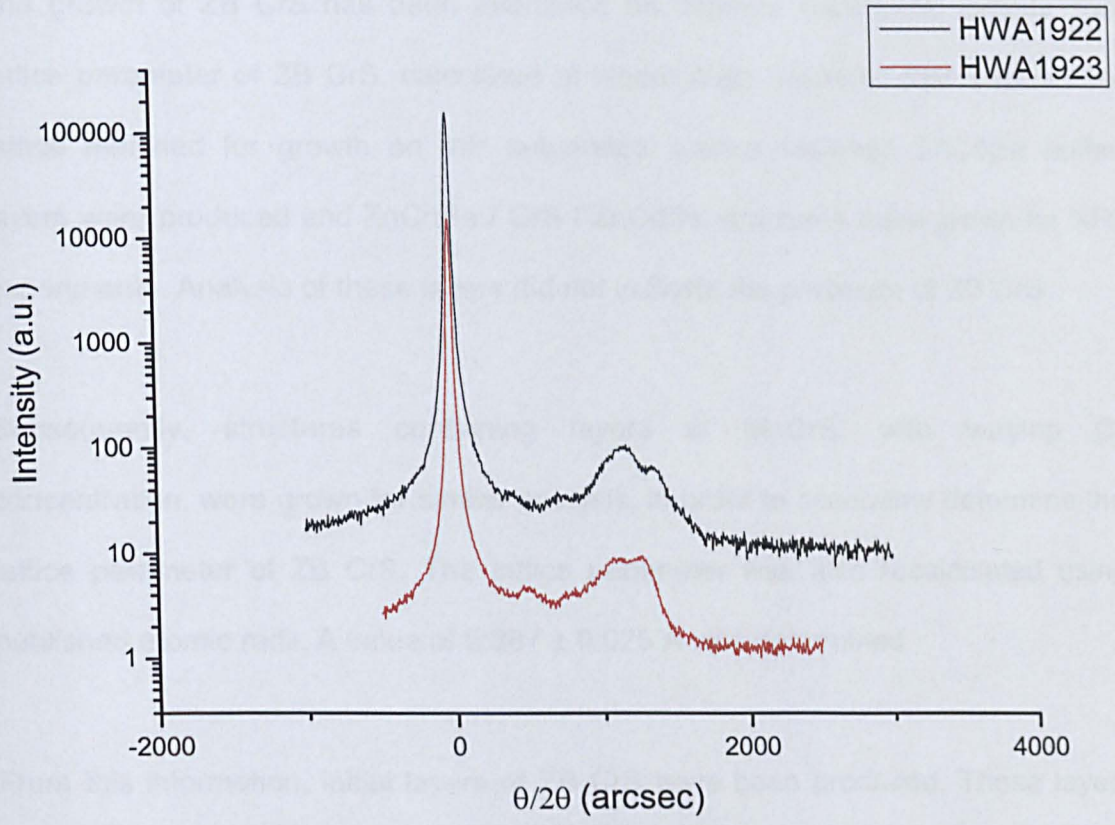

Figure 6.19: 115 XRI scans of HWA1922 and HWA1923 as indicated.

6.8 Summary

The growth of ZB CrS has been attempted on different substrates. Initially, the lattice parameter of ZB CrS, calculated at Heriot-Watt, indicated that it would be lattice matched for growth on InP substrates. Lattice matched ZnCdSe buffer layers were produced and ZnCdSe / CrS / ZnCdSe structures were grown for XRI experiments. Analysis of these layers did not indicate the presence of ZB CrS.

Subsequently, structures containing layers of MnCrS, with varying Cr concentration, were grown for similar analysis, in order to accurately determine the lattice parameter of ZB CrS. The lattice parameter was also recalculated using published atomic radii. A value of 5.387 ± 0.025 Å was determined.

From this information, initial layers of ZB CrS have been produced. These layers were grown with lattice matched ZnMgS buffer layers on (001) GaP substrates. Layers grown for initial XRI analysis indicate that the value of a_{CrS} is 5.3525 ± 0.0025 Å and Poisson's ratio for CrS is 0.48 ± 0.02. The Zn incorporation of the CrS layers is < 3%. Further analysis and optimisation is still required for CrS.

References

[1] T. Dietl and H. Ohno, Physica E **9** (2001) 185

[2] J Blinowski, P. Kacman and J.A. Majewski, Phys. Rev. B **53** (1996) 9524

[3] K.A. Prior, C. Bradford, L. David, X. Tang and B.C. Cavenett, Phys. Stat. Sol. (b) **241** (2004) 463

[4] I. Galanakis and P. Mavropoulos, Phys. Rev. B **67** (2003) 104417

[5] H. Shoren, F. Ikemoto, K. Yoshida, N. Tanaka and K. Motizuki, Physica E **10** (2001) 242

[6] www.webelements.com

[7] X.B. Zhang and S.K. Hark, J. Crystal Growth **223** (2001) 512

[8] J. Massies and J.P. Contour, J. Appl. Phys. **58** (1985) 806

[9] G.J. Davies, R. Heckingbottom, H. Ohno, C.E.C. Wood and A.R. Calawa, Appl. Phys. Lett. **37** (1980) 290

[10] R.F.C. Farrow, J. Phys. D: Appl. Phys. **7** (1974) L121

[11] H. Bando, H. Yoshino, H. Okamoto and K. Iizuka, J. Crystal Growth **278** (2005) 464

[12] Veeco, MBE Components, 2005 Product guide pp 121

[13] L. David, C. Bradford, X. Tang, T.C.M. Graham, K.A. Prior and B.C. Cavenett, J. Crystal Growth **251** (2003) 591

[14] M. Kobayashi, J. Ueno, M. Enami, S. Katsuta, A. Ichiba, K. Ogura, K. Onomitsu and Y. Horikoshi, J. Crystal Growth **278** (2005) 273

[15] J.C. Slater, J. Chem. Phys. **41** (1964) 3199

[16] E. Clementi and D.L. Raimondi, J. Chem. Phys. **38** (1963) 2686

[17] D.W. Palmer, www.semiconductors.co.uk, 2002

[18] S.A. Telfer, C. Morhain, B. Urbaszek, C. O'Donnell, P. Tomasini, A. Balocchi, K.A. Prior and B.C. Cavenett, J. Crystal Growth **214** (2000) 197

[19] K.A. Prior, S.A. Telfer, X. Tang, C. Morhain, B. Urbaszek, C. O'Donnell, P. Tomasini, A. Balocchi and B.C. Cavenett, J. Crystal Growth **227** (2001) 655

[20] K.A. Prior, X. Tang, C. O'Donnell, C. Bradford, L. David and B.C. Cavenett, J. Crystal Growth **251** (2003) 565

[21] H. Holloway, J. Appl. Phys. **67** (1990) 6229

[22] K.A. Prior, C. Bradford, L. David, X. Tang and B.C. Cavenett, J. Crystal Growth **275** (2005) 141

[23] C. Bradford, C.B. O'Donnell, B. Urbaszek, A. Balocchi, C. Morhain, K.A. Prior and B.C. Cavenett, J. Crystal Growth **227** (2001) 634

[24] L. David, X. Tang, G. Beamson, D. Wolverson, K.A. Prior and B.C. Cavenett, Phys. Stat. Sol. (b) **241** (2004) 471

Chapter 7: Conclusions and Future work

7.1 Introduction

Details of the growth of metastable ZB transition metal sulphides have been presented in this thesis. In this chapter, the results will be summarised and prospects for future work in this area will be discussed.

7.2 Growth and characterisation of MnS

7.2.1 Summary

MnS is a II-VI semiconductor material with a bandgap of 3.7 eV. The stable crystal structure of MnS is rocksalt, and previous attempts to grow MnS in the metastable ZB phase yielded layers less than 50 nm thick. Using compound ZnS as the only source of sulphur, a technique developed for MgS, MnS layers up to 132 nm thick have been produced in the ZB crystal structure.

Initially, thin layers were produced for X-ray Interference (XRI) measurements which were used to determine the growth rate of ZB MnS to be 0.15 μmh^{-1}, and subsequently, Poisson's ratio was found to be 0.475. The lattice parameter of MnS, 5.559 Å, was determined from X-ray Diffraction (XRD) of thicker layers, in conjunction with Secondary Ion Mass Spectroscopy, which showed residual Zn content of 3%.

Atomic Force Microscopy (AFM) studies of the MnS surface showed the development of ridges in the [110] direction after the deposition of ~20 nm, similar to results which were found during the growth of ZB MgS [1].

Thin layers of MnS, grown on a buffer of ZnSe, were analysed by XPS to monitor the core level positions with respect to MnS thickness. From these results, a type II valence band (VB) offset between ZnSe and MnS of 49 ± 90 meV was determined. The VB offset had been investigated previously with layers of MnS grown by conventional MBE, and those results determined the VB offset to be ~150 ± 100 meV. Differences between the two growth techniques were highlighted in the XPS results as the previous results indicate that the growth of MnS is initiated by a layer of S atoms, and in the present study, it was determined that a layer of Mn atoms formed the interface. This was confirmed by XRI.

Photoluminescence (PL) has been carried out on MnS / ZnSe quantum wells (QW) however since there is a type II VB offset between these materials, MnS does not form a good barrier material for ZnSe. The PL from a fully metastable structure of MnS QW with MgS barriers was also discussed.

7.2.2 Future Work

With regards to the work on MnS, we have completed our objective which was to show that the growth method developed for MgS could be adapted for the growth of MnS. However, we continue to supply samples to other groups on request, who

have characterisation facilities that are not available at Heriot-Watt. Some results from samples already supplied are given here.

Raman spectroscopy has been carried out on layers of MnS supplied recently to the University of Bath, UK. The spectra were obtained using 244 nm excitation from a CW frequency-doubled argon ion laser. Figure 7.1 shows the preliminary Raman data obtained from HWA1432, a 67 nm layer of MnS. The third overtone of the MnS LO phonon was found at 1122 cm^{-1}, which gives the LO phonon frequency to be 380 cm^{-1}. The LO phonon frequencies of many II-VI compounds scale linearly with reduced mass. MnS has a similar reduced mass to ZnS and the LO phonon frequency of this material is also similar, 351 cm^{-1} [2]. In this respect it is unlike MgS, where the LO phonon frequency of 421 cm^{-1} is far lower than the value predicted by this model of approximately 500 cm^{-1} [3]. Further characterisation of ZB MnS by Raman spectroscopy will be carried out.

From the initial analysis of the PL from the fully metastable MgS / MnS QW, it is clear that further characterisation of this structure is required. XPS measurements of MgS / MnS, in order to determine the VB offset, would also shed some light on the interface between MgS and MnS. However, *in situ* XPS is required as MgS is hygroscopic and requires a cap to prevent surface oxidization in air. At present, no such system exists at Heriot-Watt, therefore no conclusive XPS measurements can be taken.

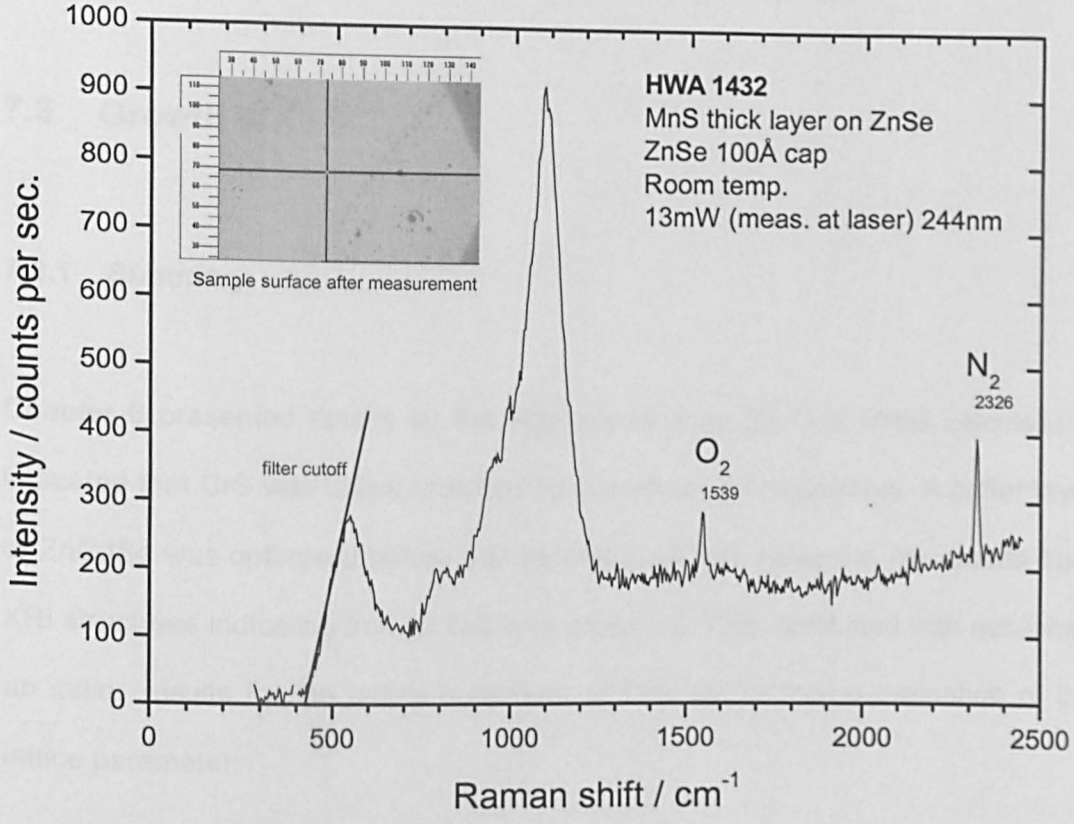

Figure 7.1: Preliminary Raman data from HWA1432, a 67 nm layer of MnS. The inset shows that the sample surface was not degraded after the data was taken.

Initial discussions between our group and those at the Polish Academy of Sciences, indicate that they are keen to study the magnetic properties of MnS layers. At present, there have been no specific sample requests.

7.3 Growth of CrS

7.3.1 Summary

Chapter 6 presented details on the attempts to grow ZB CrS. Initial calculations indicated that CrS was lattice matched for growth on InP substrates. A buffer layer of ZnCdSe was optimised before the deposition of CrS. However, the results from XRI structures indicating that no CrS was produced. This, combined with published *ab initio* results for the lattice parameter of CrS, led to the re-evaluation of the lattice parameter.

MnCrS layers were grown on GaAs substrates for XRI analysis to determine lattice parameter of CrS. During this analysis, the lattice parameter of CrS was also re-calculated from published atomic radii. The combined result of this gave a value for the lattice parameter of CrS as 5.387 Å, which is lattice matched to GaP.

Subsequently, thin CrS layers were grown with cladding layers of ZnS for XRI measurements. However, the XRI scans showed no Pendellösung fringes, which indicated that the incident x-ray beam considered the structure as a single layer. This problem was overcome by using ZnMgS, lattice matched to GaP, as the

cladding layer. Results from the XRI of thin CrS layers were presented, indicating that the Zn incorporation of the layer was ~ 2% and the layer thickness was 3 nm.

7.3.2 Future work

Based on the initial growth of ZB CrS, it is clear that further optimisation is required as well as characterisation of CrS layers. Thicker layers must be produced for SIMS to confirm the residual Zn content of the layers, as well as XRD measurements to verify the determinations of lattice parameter and Poisson's ratio presented in this thesis.

Once the growth has been optimized, layers will be supplied to Prof. Tomasz Dietl at the Polish Academy of Sciences, in order to study the magnetic susceptibility of CrS and accurately determine the Curie point. These samples will be multilayer structures of CrS and ZnMgS to ensure that the CrS layers are thick enough for magnetic susceptibility measurements while still maintaining the ZB crystal structure.

MnCrS layers of varying Cr concentration as well as MnS layers have recently been sent to Dr. Peter Klar from Philipps-University of Marburg, who are currently interested in the energy transfer processes between Mn ions in nanostructures of (II,Mn)VI semiconductors. The concentration and geometry dependence of the time-resolved luminescence of the yellow Mn PL emission is also of interest. Dr. Klar is particularly interested in investigating whether any emission from the Cr in the MnCrS layers quenches the emission from the internal Mn transition.

Since the technique developed for the growth of ZB MgS has proven successful for the growth of both MnS and CrS, it can be applied to other transition metal sulphides. FeS is expected to be antiferromagnetic but Dietl has suggested that more complex layered binary compounds could benefit from strong antiferromagnetic coupling. For example, in a structure consisting of alternating monolayers of MnS and FeS, the antiferromagnetic coupling between the Mn and Fe ions would produce a net ferrimagnetic effect [4].

The lattice parameter of FeS has been calculated by the same method as in section 6.6, with a result of 5.413 Å. Therefore, initial layers of FeS can be grown on GaP substrates for characterisation with structures of GaP (sub) / ZnMgS / FeS / ZnMgS grown for XRI analysis. Subsequent multilayer structures of MnS / FeS can be grown on GaAs substrates with strain relieving ZnSe spacer layers between each multilayer. The strains of each material to GaAs are shown in Table 7.1.

Table 7.1: Epilayer strain to GaAs substrate.

Material	Lattice Parameter (Å)	Strain to GaAs (ϵ)
GaAs	5.6532	0
ZnSe	5.6676	0.00254
MnS	5.559	-0.0169
FeS	5.413	-0.0444

If the MnS and FeS layers are 1 monolayer thick each and assuming the lattice parameter calculated for FeS is correct, then the strain relieved structure would require ZnSe spacer layers of 6.5 nm between each MnS / FeS multilayer.

References

[1] C. Bradford, K.A. Prior and B.C. Cavenett, Phys. Stat. Sol. (c) **1** (2004) 645

[2] S.S. Mitra, O. Brafman, W.B. Daniels and R.K. Crawford, Phys. Rev. **186** (1969) 942

[3] D. Wolverson, D.M. Bird, C. Bradford, K.A. Prior and B.C. Cavenett, Phys. Rev. B **64** (2001) 113203

[4] T. Dietl and H. Ohno, Physica E **9** (2001) 185